Biological Cybernetics

Volume 25 Number 4 1977

Indexed in Current Contents

Springer-Verlag Berlin Heidelberg New York

Biol. Cybernetics ISSN 0340-1200 BICYAF 25 (4) 181-240 (1977)

28. 2. 1977

Lecture Notes in Biomathematics

This series aims to report new developments in biomathematics research and teaching—quickly, informally and at a high level. The type of material considered for publication includes:

1. Preliminary drafts of original papers and monographs
2. Lectures on a new field, or presenting a new angle on a classical field
3. Seminar work-outs
4. Reports of meetings, provided they are
   a) of exceptional interest and
   b) devoted to a single topic

Volume 1: P. WALTMAN
Deterministic Threshold Models in the Theory of Epidemics
15 figures. V, 101 pages. 1974
DM 16,—; US $7.10
ISBN 3-540-06652-7

Volume 2:
Mathematical Problems in Biology
Victoria Conference
Editor: P. van den Driessche
VI, 280 pages. 1974
DM 28,—; US $12.40
ISBN 3-540-06847-3

Volume 3: D. LUDWIG
Stochastic Population Theories
Notes by M. Levandowsky
VI, 108 pages. 1974
DM 18,—; US $8,—
ISBN 3-540-07010-9

Volume 4:
Physics and Mathematics of the Nervous System
Proceedings of a Summer School organized by the International Centre for Theoretical Physics, Trieste, and the Institute for Information Sciences, University of Tübingen, held at Trieste, August 21—31, 1973
Editors: M. Conrad, W. Güttinger, M. Dal Cin
159 figures. XI, 584 pages. 1974
DM 45,—; US $19.80
ISBN 3-540-07014-1

Volume 5:
Mathematical Analysis of Decision Problems in Ecology
Proceedings of the NATO Conference held in Istanbul, Turkey, July 9—13, 1973
Editors: A. Charnes, W. R. Lynn
77 figures, 23 tables
VIII, 421 pages. 1975
DM 35,—; US $15.40
ISBN 3-540-07188-1

Volume 6: H. T. BANKS
Modeling and Control in the Biomedical Sciences
22 figures. V, 114 pages. 1975
DM 18,—; US $8,—
ISBN 3-540-07395-7

Volume 7: M. C. MACKEY
Ion Transport through Biological Membranes
An Integrated Theoretical Approach
46 figures, 13 tables
IX, 240 pages. 1975
DM 25,—; US $11,—
ISBN 3-540-07532-1

Volume 8: C. DELISI
Antigen Antibody Interactions
29 figures, 2 tables
IV, 142 pages. 1976
DM 18,—; US $8,—
ISBN 3-540-07697-2

Volume 9: N. DUBIN
A Stochastic Model for Immunological Feedback in Carcinogenesis: Analysis and Approximations
18 figures, 1 table
XIII, 163 pages. 1976
DM 20,—; US $8.80
ISBN 3-540-07786-3

Volume 10: J. J. TYSON
The Belousov-Zhabotinskii Reaction
29 figures, 1 table
IX, 128 pages. 1976
DM 18,—; US $8,—
ISBN 3-540-07792-8

Volume 11:
Mathematical Models in Medicine
Workshop, Mainz, March 1976
Editors: J. Berger, J. Bühler, R. Repges, P. Tautu
XII, 281 pages. 1976
DM 28,—; US $12.40
ISBN 3-540-07802-9

Springer-Verlag
Berlin
Heidelberg
New York

Prices are subject to change without notice

5010/4/1

Biological Cybernetics

Communication and Control in Organisms and Automata

Nachrichtenübertragung, Nachrichtenverarbeitung, Steuerung und Regelung in Organismen und in Automaten

Editors

H. B. Barlow, Cambridge/Cambs. · J. D. Cowan, Chicago/Ill.
O. Creutzfeldt, Göttingen · B. Hassenstein, Freiburg i. Br.
W. D. Keidel, Erlangen · K. Küpfmüller, Darmstadt
D. M. MacKay, Keele/Staffs. · H. Mittelstaedt, Seewiesen/Obb.
W. Reichardt, Tübingen (Editor-in-Chief) · W. A. Rosenblith, Cambridge/Mass.
J. F. Schouten, Eindhoven · D. Varjú, Tübingen

Springer-Verlag Berlin Heidelberg New York

Biological Cybernetics

Communication and control in organisms and automata.
Continuation of „Kybernetik" (Volume 1—16)

Biological Cybernetics appears about every month.

Subscription Information

Volumes 25—28 (4 issues each) will appear in 1977. The publisher reserves the right to issue additional volumes during the calendar year. Information about obtaining back volumes available upon request.

All Countries (Except North America). Subscription rate: DM 592,— plus postage and handling. Orders can either be placed with your bookdealer or sent directly to: Springer-Verlag, Heidelberger Platz 3, D-1000 Berlin 33.

North America. Subscription rate: $ 254.00 including postage and handling. Subscriptions are entered with prepayment only. Orders should be sent to your bookdealer or subscription agency or directly to: Springer-Verlag New York Inc. 175 Fifth Avenue, New York, N. Y. 10010.

Manuscripts should be addressed to:
Prof. Dr. W. Reichardt
Max-Planck-Institut für biologische Kybernetik
Spemannstraße 38
D-7400 Tübingen, FRG

It is a fundamental condition that submitted manuscripts have not been and will not be, simultaneously submitted elsewhere.

Correspondence concerning advertisements should be sent to the Advertisement Department of the publishing firm in Berlin: Kurfürstendamm 237, D-1000 Berlin 15, Tel. (0 30) 8 82 10 31, Telex 01-85 411.

Springer-Verlag

Heidelberger Platz 3
D-1000 Berlin 33
Tel. (0 30) 82 20 01
Telex 01-83 319

Postfach 105 280
D-6900 Heidelberg 1
Tel. (0 62 21) 4 87-1
Telex 04-61 690

Springer-Verlag New York Inc.
175 Fifth Avenue
New York, N. Y. 10010
Tel. 2 12 (6 73-26 60)
Telex 00-23 22 235

The concepts of transmission of information, processing of information and automatic control engineering originated within technology and physics. Today, however, these concepts have also proved useful in the biological sciences where analogous processes of communication and control are encountered. Despite the differences between nonliving and living systems, many of the logical procedures, the experimental and theoretical approaches and the mathematical techniques applicable to the physical sciences also find natural applications in the realm of the life sciences. In particular, by adopting this approach to sensory and neurophysiological problems new insight has been gained into the principles by means of which organisms handle and utilize information. Conversely, physicists and engineers have shown increasing interest in natural mechanisms of communication and control, including genetic communication and the control of reproduction.

The aim of "Biological Cybernetics" is to promote the exchange of experimental and theoretical information in the following fields: Quantitative analysis of behaviour, in both vertebrates and invertebrates; quantitative micro- and macro-physiological studies of information-processing in receptors, neural systems and effectors; mathematical models of communication and control processes in organisms, including reproductive mechanisms; biologically relevant aspects of information theory, network theory, theory of automata, theory of control systems.

Contents of the next issue

Hinweise für die Autoren*

Die Beiträge sind so kurz wie möglich abzufassen. 3 zweizeilig beschriebene DIN-A-4-Seiten entsprechen etwa einer Druckseite.

Der Umfang eines Manuskripts sollte 25 Schreibmaschinenseiten inclusive Abbildungen und Tabellen nicht überschreiten.

Ein Manuskript muß formal wie inhaltlich so durchgearbeitet sein, daß spätere Änderungen nicht notwendig werden, da der Beitrag sofort nach dem Satz auf Seitenformat umbrochen wird. Nachträgliche, vom Manuskript abweichende Änderungen müssen dem Autor berechnet werden. Der Autor erhält einen endgültigen Umbruch mit provisorischer Paginierung (2fach). Seitenhinweise können daher bei der Korrektur vorgenommen werden. Der Verlag besorgt das Einsetzen der endgültigen Seitenzahlen. In dem Umbruch sind bereits die Abbildungen und Tabellen enthalten. Im Manuskript sind die gewünschten Einschaltstellen der Abbildungen und Tabellen an den für sie vorgesehenen Positionen am Rand anzugeben.

Das Manuskript muß mit Maschine, einseitig und mit breitem Rand geschrieben werden; die Blätter sind einschließlich Literaturverzeichnis und Legenden durchzunumerieren.

Jedem Manuskript sind auf gesondertem Blatt „Anweisungen für den Satz" beizugeben, auf dem die benutzten Kennzeichnungen sowie verwendete besondere Symbole erklärt werden.

Jedem Beitrag soll eine *Zusammenfassung* beigegeben werden. Für deutsche Arbeiten sind Zusammenfassungen in englischer Sprache sowie eine englische Übersetzung des Titels erwünscht.

Kursiv zu setzende Wörter oder Sätze sind durch Unterstreichung zu kennzeichnen.

Soweit Teile des Manuskriptes in einem *kleineren Schriftgrad* (Petit) gesetzt werden können, sind sie durch einen vertikalen Strich am Rand unter Beifügung des Buchstabens „p" zu kennzeichnen. Formeln, Fußnoten und Tabellen werden automatisch in Petit gesetzt. *Tabellen* sind mit Überschriften zu versehen und laufend zu numerieren.

Fußnoten, die nicht zum Beitragskopf gehören, sind durchzunumerieren. Sie sollen am Fuß der einzelnen Manuskript-Blätter (nicht geschlossen am Ende der Arbeit) stehen.

Beim Lesen der *Formeln* darf auch dem Laien über die Stellung und Deutung der Zeichen und Buchstaben kein Zweifel aufkommen. *Alle Formeln sind möglichst mit der Maschine zu schreiben,* wobei genau darauf zu achten ist, daß Indizes und Exponenten trotz des fehlenden Größenunterschiedes genau als solche zu erkennen sind. Andernfalls müssen diese in geringerer Größe mit der Hand eingetragen werden. Besondere Lettern (griechische, gotische, Skript) sind durch farbige Unterstreichung zu kennzeichnen. Zur Vermeidung von Verwechslungen wird gebeten, *griechische Buchstaben rot, gotische blau und Skripttypen grün zu unterstreichen.* Handgeschriebene Buchstaben sind häufig schwer zu identifizieren und werden in verschiedenen Ländern teilweise verschieden geschrieben. Deshalb wird gebeten, auch gotische und Skriptbuchstaben mit der Maschine als lateinische Buchstaben zu schreiben und allein durch die farbige Unterstreichung zu kennzeichnen. Sofern dennoch handgeschriebene Buchstaben vorkommen, unterscheide man das große und kleine Alphabet: *große Buchstaben sollten zweimal, kleine einmal unterstrichen werden.* Das gilt auch für handgeschriebene lateinische Buchstaben, insondere für: *c, C*; *k, K*; *p, P*; *o, O*; *s, S*; *u, U*; *v, V*; *w, W*; *x, X* und *z, Z*. Besonders sorgfältig beachte man die Schreibweise bei handschriftlichen Buchstaben, wenn gleichzeitig *e* und *l*, oder *u* und *n* und *r*, oder *o* und 0 als mathematische Bezeichnungen auftreten. Auch gleichzeitig auftretende v und ν sowie ε und ϵ geben zu Verwechslungen Anlaß. Man vermeide bei mathematischen Typen Unterstreichung mit Tinte oder Schreibmaschine, eine solche müßte beim Satz zwangsweise als zum mathematischen Sinn gehörig mitgesetzt werden.

Besondere Schwierigkeiten entstehen dadurch, daß Schreibmaschinen im allgemeinen keine Unterschiede zwischen 0 (Null) und *O* (Buchstabe), sowie häufig auch zwischen 1 (Eins) und *l* (Buchstabe) kennen. *Hier sind unterscheidende Kennzeichnungen unbedingt erforderlich.* Die arabische Ziffer 1 schreibe man deutlich als 1 und nicht als senkrechten Strich. Letzteres ist besonders verhängnisvoll, wenn die 1 als oberer Index auftritt. In englischsprachigen Manuskripten schließe man, wenn der kleine lateinische Buchstabe *a* als mathematische Bezeichnung vorkommt, die Verwechslung mit dem unbestimmten Artikel durch mehr Abstand auf beiden Seiten aus.

Sämtliche Buchstaben in Formeln und Einzelbuchstaben im Text werden automatisch kursiv gesetzt und sind deshalb nicht besonders zu unterstreichen. Dagegen müssen in Formeln auftretende Abkürzungen wie Ord, Op, Re, Im, grad, div, dim, codim, rang, id, lim, bound, sup, die in Antiqua gesetzt werden sollen, besonders gekennzeichnet werden (gelb unterstreichen, soweit es sich nicht um die allgemein bekannten trigonometrischen Funktionen handelt). Vektoren (Buchstaben mit Pfeil darüber) werden immer halbfett gesetzt (ohne Pfeil).

* Diese Hinweise werden alternierend in deutscher und englischer Sprache abgedruckt.

Schemata bzw. Figuren werden getrennt vom Text auf besonderen Blättern erbeten.

Die Abbildungen sollen die Breite einer Spalte (8,1 cm) oder den Satzspiegel (16,8 x 22 cm) — inklusive Abbildungsunterschrift — nicht überschreiten. Mehrere Abbildungen sollen zu einem Tableau innerhalb einer Seite zusammengefaßt werden. Für *Strichabbildungen* werden gute scharfe Fotoabzüge in der gewünschten Endgröße erbeten. Die Beschriftung soll klar lesbar sein. Optimal ist eine Schrifthöhe von 2 mm. Für *Halbtonabbildungen* sind kontrastreiche gute Fotoabzüge, rechtwinklig beschnitten, in der gewünschten Endgröße einzusenden. Die Beschriftung soll ca. 3 mm hoch sein. Für alle Abbildungen sind Unterschriften auf gesonderten Blättern beizufügen. Bei Übernahme von Abbildungen aus anderen Werken wird um genaue Quellenangabe gebeten.

Literaturzitate sind als geschlossenes Verzeichnis am Ende der Arbeit zu bringen. Bei Zeitschriften-Artikeln sind folgende Angaben unerläßlich: Namen und Initialen sämtlicher Autoren, vollständiger Titel der Arbeit, Zeitschriftentitel, Band-, Seiten- (stets auch End-Seitenzahlen) und Jahreszahl, z. B.

Leibovic, K. N., Balslev, E., Mathieson, T. A.: Binocular vision and pattern recognition. Kybernetik **8**, 14—23 (1970)

Bücher werden mit Autor(en), vollem Titel, Auflage, Ort, Verlag und Jahr zitiert, z. B.

Landgraf, Chr., Schneider, G.: Elemente der Regelungstechnik. Berlin - Heidelberg - New York: Springer 1970

In den Umbruchabzügen sollen *nur Satzfehler verbessert* werden. Neue Ergebnisse können als „Nachtrag bei der Korrektur" angehängt werden.

Sonderdrucke: 50 Sonderdrucke werden von jedem Beitrag kostenlos zur Verfügung gestellt.

Die Adresse des Autors ist genau anzugeben. Wechselt der Autor bis zum Erscheinen seiner Arbeit seine Anschrift, so bitten wir in seinem eigenen Interesse dringend um sofortige Benachrichtigung.

Verwendete Alphabete:

Kursiv* (normale Satzweise von Formelbuchstaben)
A, B, C, D, ..., Z; a, b, c, d, ..., z

Grotesk* (auch in Kursiv vorhanden)
A, B, C, D, ..., Z; a, b, c, d, ..., z

Gotisch* ..... $\mathfrak{A}, \mathfrak{B}, \mathfrak{C}, \mathfrak{D}, \ldots, \mathfrak{Z}$; $\mathfrak{a}, \mathfrak{b}, \mathfrak{c}, \mathfrak{d}, \ldots, \mathfrak{z}$

Schreibschrift (Skript)
$\mathscr{A}, \mathscr{B}, \mathscr{C}, \mathscr{D}, \mathscr{E}, \mathscr{F}, \mathscr{G}, \mathscr{H}, \mathscr{I}, \mathscr{J}, \mathscr{K}, \mathscr{L}, \mathscr{M}, \mathscr{N}, \mathscr{O}, \mathscr{P}, \mathscr{Q}, \mathscr{R}, \mathscr{S}, \mathscr{T}, \mathscr{U}, \mathscr{V}, \mathscr{W}, \mathscr{X}, \mathscr{Y}, \mathscr{Z}$

Griechisch* A, B, $\Gamma, \Delta, \ldots, \Omega$; $\alpha, \beta, \gamma, \delta, \ldots, \omega$

* Das betreffende Alphabet ist auch in halbfett vorhanden.

Biol. Cybernetics 25, 181–194 (1977)

Biological Cybernetics

Spatial Mapping in the Primate Sensory Projection: Analytic Structure and Relevance to Perception*

E. L. Schwartz

Brain Research Laboratories, New York Medical College, New York, USA

Abstract. The retinotopic mapping of the visual field to the surface of the striate cortex is characterized as a logarithmic conformal mapping. This summarizes in a concise way the observed curve of cortical magnification, the linear scaling of receptive field size with eccentricity, and the mapping of global visual field landmarks. It is shown that if this global structure is reiterated at the local level, then the sequence regularity of the simple cells of area 17 may be accounted for as well. Recently published data on the secondary visual area, the medial visual area, and the inferior pulvinar of the owl monkey suggests that the same global logarithmic structure holds for these areas as well. The available data on the structure of the somatotopic mapping (area $S-1$) supports a similar analysis. The possible relevance of the analytical form of the cortical receptotopic maps to perception is examined and a brief discussion of the developmental implications of these findings is presented.

Introduction

The primary sensory projection of the brain is a topographic mapping of the receptor periphery onto the central neural processor. Early workers such as Talbot and Marshall [29] (retinostriate projection), Apter [7] (retinotectal projection), Woolsey [36] (somatotopic projection), and Lorenté de No [20] (auditory projection) established the basic existence and structure of these mappings using relatively crude slow-wave recording techniques. Subsequent work, making use of more refined and sophisticated single-unit mapping methods, has served in recent years to greatly increase the detailed knowledge of the structure of the various sensory mappings, and has extended their domain of definition to include a variety of thalamic and mid-brain structures as well.

The existence of orderly spatial mapping in diverse neural structures would seem to have considerable importance to the functional aspects of sensory neurophysiology: in each modality, a receptor surface (the retina, the cutaneous surface, the basilar membrane) is mapped, through sub-cortical relay nuclei, to an essentially two-dimensional (laminar) representation at the cortical surface. This representation of the sensorium in terms of a receptor sheet mapped onto a cortical surface has led Arbib [8] to characterize the brain as "a layered, somatotopically organized computer".

The view of the primary sensory projection as a planar (although "distorted") map of the sensorium underlies a basic controversy that has existed for the past thirty years. Somjen [26] has provided a concise statement of this question:

"The issue of the cortical movie screen, popular at first, discredited later... and defended once again, is still not resolved. The presence of these topographically organized projection areas can hardly be mere accident, of course. Besides the retina and the body surface, the receptor sheet of the cochlea also finds a representation of sorts in several regions of the brain. What kind of significance can we attach to them?"

The present work is a critical examination of this question, which begins by analyzing the anatomical and physiological data that has accumulated during the past twentyfive years on the detailed structure of the retinotopic mapping of the striate cortex (area 17). It is possible to present a simple analytic description of the retinotopic mapping, using complex variables to represent points in the visual and cortical planes. The retinotopic mapping is thus found to be a complex logarithmic (conformal) mapping of the visual field onto the cortical surface. Furthermore, the available evidence suggests that the receptotopic

* This work was supported by Grant No. 1 F32MH05367-01 from the USPHS, ADAMHA

mappings of the secondary visual cortex, the inferior pulvinar, and the somatosensory cortex, may be described by the same mathematical formalism. In addition, it is pointed out that the local receptive field structure of the striate cortex, as represented by Hubel and Wiesels [17] model of the hypercolumn, may very well be the consequence of a complex logarithmic mapping on a local scale. The possible relevance to visual perception of the complex logarithmic mapping will then be investigated by studying the mapping of a visual stimulus. This demonstration will support, in a graphic way, the conclusion that the preprocessing of the two-dimensional brightness distribution available at the retina, by the complex logarithmic retinotopic mapping, may possibly play a role in the analysis of form invariant information. Finally, a brief discussion of the seemingly ubiquitous presence of complex logarithmic structure in the sensory projection will be presented with respect to the developmental mechanisms that could lead to this structure in a biological system.

Global Retinotopy

The notion of retinotopy may be traced back to the pioneering anatomical investigations of Polyak [23], who suggested, on the basis of the anatomy of the visual cortex, that a mathematical projection of the retina on the cortex must exist. Talbot and Marshall [29] confirmed this hypothesis with physiological methods, and the extensive investigation of Daniel and Whitteridge [11] provided a source of precise, quantitative data; however, a mathematical analysis of the retinotopic mapping has never been presented.

In subsequent work, making use of single cell recording techniques, the locus of accurate topographical representation in the striate cortex has been limited to layer IVc, where the receptive fields are predominantly small and circularly symmetric, and the cortical afferents arriving from the lateral geniculate nucleus (LGN) arrive and terminate [17]. In the subsequent discussion of global topography, it will be understood that it is mainly layer IVc of the striate cortex that is accurately retinotopic. Following this discussion of global topography, the local remapping of cortical afferents to simple cells, which are located mainly in the cortical laminae surrounding layer IVc, will be separately analyzed.

Daniel and Whitteridge measured the cortical magnification factor by recording slow wave and multiple unit responses to spots of light in the visual periphery, and then reconstructing the electrode tracks from histological sections. They defined the cortical magnification factor as the distance moved (in millimeters) across the cortical surface corresponding to one degree of movement of a point stimulus in the visual field [11].

Daniel and Whitteridge found that the cortical magnification factor is the same along all radii, regardless of the angular coordinate, and is the same whether measured radially or along the circumference; thus the magnification factor is radially symmetric.

The cortical magnification data was used to construct a three dimensional model, which accounted closely for the surface area of the cortex, and could be simply folded to duplicate the actual folding pattern of the striate cortex. However, their investigation was largely phenomenological: "no simple equation was found to fit the data".

Daniel and Whitteridge presented their cortical magnification data graphically. For the present analysis, data published in their original work were measured, and fit by computer to a power law. The fit is excellent over the entire range of measured date (from 1° to 50°):

Figure 1A

$$M(r) = 6^{\star}(r)^{-0.9} \quad (\text{C.L.} = 95\%) . \tag{1}$$

$M(r)$ is the magnification factor in millimeters/degree, and the variable r measures the eccentricity in degrees. The choice of r as the variable representing eccentricity is made in order to simplify the geometry by approximating the visual sphere by its tangent plane. The spherical polar coordinates of eccentricity and azimuth may be approximated by the polar coordinates of the tangent plane (r and ϕ). The polar coordinate ϕ is identical to the azimuthal spherical coordinate. The polar coordinate r is approximately proportional to the eccentricity:

$$r = R \sin \Theta \cong R\Theta . \tag{2}$$

Where r is the tangent plane radial polar coordinate, R is the radial distance of the tangent plane from the retina, and Θ is the eccentricity. The approximation of Equation (2) is accurate to 98% for the central 20 degrees of visual field. Furthermore, for a tangent plane that is placed 57.3 cm from the eye, the polar coordinate r in the tangent plane is numerically equal (in cm) to the eccentricity in degrees.

The fit of Equation (1) is the best power fit to the data of Daniel and Whitteridge. For the central foveal representation (less than 1° of eccentricity), no magnification data is available; it is assumed that the inverse dependence on eccentricity tapers off in a gradual way for this central-most part of the visual field. For the central 20 degrees of visual field, a simple straight line fit to the inverse magnification is in excellent agreement with the data. In order to include peripheral parts of the visual field (beyond 20°), Equation (1) may be used, which is very close to an

inverse linear dependence on eccentricity for the entire visual field. Thus, the exponent of r in Equation (1) is sufficiently close to unity to be replaced by it; that is supported by the later work of Hubel and Wiesel [18], who find that the inverse magnification curve is closely approximated by a straight line. In light of the previous discussion, it is possible to simplify the analysis of Daniel and Whitteridge's data, expressed in Equation (1) by the approximation:

$$m = k/r\,. \tag{3}$$

Where k is a constant, r represents eccentricity from the fixation point (foveal representation) and m is the magnification. Cortical magnification is a differential quantity: small changes in cortical position are related to small changes in visual field position. Since we are interested in the analytic form of the retinotopic mapping, and not its derivative, we must find an analytic function whose derivative is radially symmetric and is proportional to $1/r$. The analytic function that has this property is the complex logarithm:

$$w = \ln(z) \tag{4}$$

where w represents a point in the cortical plane and z represents a point in the visual plane, which may be represented as:

$$z = r\exp(i\phi)\,. \tag{5}$$

Equation (4) may be written in real variables as:

$$z = \ln r$$
$$y = \phi \tag{6}$$

with the point (x, y) located in the cortical plane and the point (r, ϕ) located in the visual plane.

Magnification is defined for a complex (conformal) mapping as the amount by which an infinitesimal line segment is "stretched" by the mapping $f(z)$ [1]. This is exactly analagous to the physiological definition of magnification. In general, the magnification of a conformal mapping may be written as: (1)

$$m(z_0) = \lim_{z \to z_0} \left| \frac{f(z) - f(z_0)}{z - z_0} \right| = |f'(z_0)|\,. \tag{7}$$

Substituting the logarithm function for $f(z)$, we have:

$$|f'(z_0)| = \left| \frac{k}{z_0} \right| = \left| k \frac{e^{-i\phi}}{r_0} \right| = \frac{k}{r_0}\,. \tag{8}$$

Thus, the magnification of the complex logarithm has the required logarithmic dependence on eccentricity, and is radially symmetric, satisfying the experimental findings of Daniel and Whitteridge. In order to verify this analysis, it is possible to examine the mapping of global visual field landmarks and compare these to the predicted mappings of the same stimuli under the logarithmic mapping. It should be emphasized that this is a totally independent verification. The (differential) cortical magnification, as a measurement, is independent of the (global) measured representations of the vertical and horizontal meridians, and other visual landmarks.

The mapping of global visual field landmarks, as measured by Talbot and Marshall and Daniel and Whitteridge is shown in Figure 1B.

The vertical meridian is wrapped around the visual projection, and forms the border of area 17; *circles of constant eccentricity are mapped to vertical straight lines.* Alongside the experimental data is presented the predicted mappings of the same visual field landmarks. There is excellent agreement between the measured and predicted geometries.

Thus, the phenomenological aspects of the retinotopic mapping discussed above, and illustrated in Figures 1A and 1B support the hypothesis summarized by Equation (4).

The characteristic features of planar mapping which indicate the underlying presence of logarithmic spatial structure are summarized in Table 1, and are derived in Appendix 1.

These features may be thought of as the "signature" of the complex logarithmic mapping. Wherever these "signatures" are evident in a receptotopic mapping, the presence of a logarithmic spatial structure may be inferred. This situation is analagous to plotting data on semi-logarithmic paper. Exponentually distributed data is difficult to characterize by eye; if one takes the (exponential) data points representing the growth of a bacteria colony and plots them on linear graph paper, they may seem to be derived from an exponential distribution. However, if the same data is plotted on semi-logarithmic paper, the resultant straight line fit is satisfying confirmation that the underlying distribution actually is exponential. In a similar manner, once the underlying signatures of the complex logarithmic mapping are familiar, it becomes very much

Table 1. Geometry of the logarithmic conformal mapping

$\log z$	=	w
1. Concentric circles (exponentially spaced)		Vertical lines (equally spaced)
2. Radial lines (equal angular spacing)		Horizontal lines (equally spaced)
3. Logarithmic spirals ($\varrho = Ae^{k\phi}$)		Inclined straight lines slope $= l/k$; intercept $= -(\log A)/k$

The three geometric patterns on the left are the level lines (1), or streamlines, of the logarithmic conformal mapping. Numbers 1 and 2 may be thought of as limiting cases of the logarithmic spiral; No. 1 for $k = 0$ and No. 2 for $k = \infty$

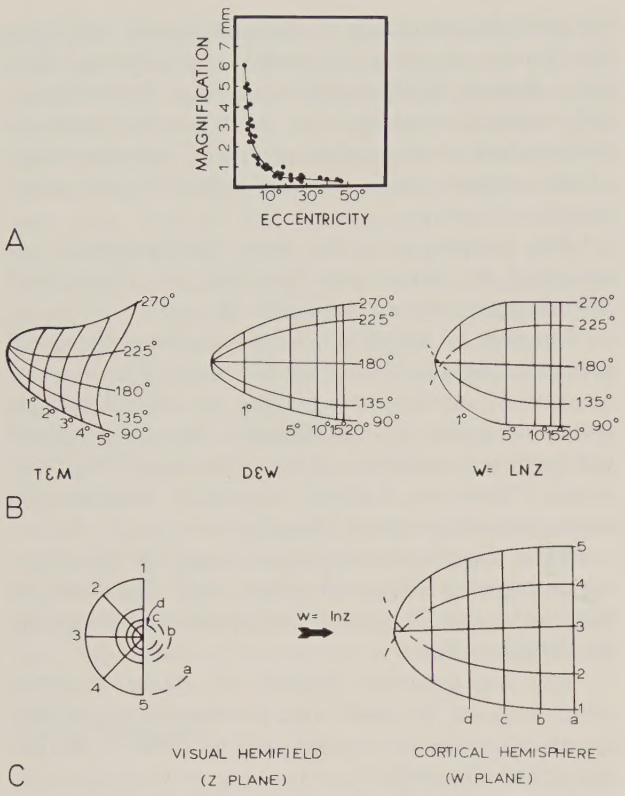

Fig. 1. **A** The cortical magnification data of Daniel and Whitteridge. Through the points is drawn the best fit to the data for a power law, as described in the text. **B** The measured and predicted mapping of visual landmarks in striate cortex. The upper (90°) and the lower (270°) vertical meridians, the horizontal half meridian (180°), the octants (135° and 225°) and the circles of constant eccentricity are drawn as measured by Talbot and Marshall, and Daniel and Whitteridge. The data of Talbot and Marshall, on the left, does not show the correct (logarithmic) spacing between the lines of constant eccentricity; their experiment is the pioneering measurement of this data. The data of Daniel and Whitteridge is much more accurate, and is shown in the center. This is a projection, onto a horizontal plane, of a three dimensional model; the meridians and octants are equally spaced, as they are in the theoretical prediction of these mappings under the logarithmic conformal mapping. The theoretical prediction, on the right, actually represents a vertical meridian that is infinitesimally displaced from the origin; otherwise the curved part of the contour would actually be a right angle. The horizontal meridian is an average of a line infinitesimally above and below the precise horizontal meridian. With these qualitative reservations, there is great similarity between the data and the theoretical prediction of the data under the logarithmic mapping. **C** The global retinotopic mapping under the logarithm function. Concentric circles (exponentially spaced) and radial straight lines are mapped onto the equidistant cartesian grid on the cortex. Note the density (derivative) of the exponentially spaced lines gives a linear dependence on the eccentricity; this is observed as a linear scaling of the receptive field size in the visual plane, with a constant (hypercolumn) size in the cortex

easier to identify the presence of complex logarithmic structure. This analogy is particularly applicable to neuroanatomical data because of the complex folding and bending characteristic of neural structures. Virtually all the "surfaces" alluded to in this paper are actually highly complex, convoluted, doubly curved surfaces, for which the "planar" structure must be inferred by histological reconstruction, and then by projection onto a planar map. Naturally, the maps that result from this procedure are often difficult to interpret merely by their visual appearance. However, the signature of spatial logarithmic structure, as outlined above, is easy to see and provides satusfying confirmation of the underlying mathematical structure of the neural maps.

The previous analysis has demonstrated that the retinotopic mapping of the striate cortex may be mathematically described as a complex logarithmic mapping. The characteristics of logarithmic spatial structure that support this statement are summarized in Table 1. In the case of the striate cortex, excellent measurements are available, and these satisfy all the requirements specified in Table 1 for the existence of logarithmic spatial structure. For other cortical and sub-cortical areas and modalities, the experimental data is much less comprehensive. Nevertheless, the signature of the complex logarithm is so characteristic that it is possible to identify a receptotopic mapping as a logarithmic mapping, even in the absence of the detailed data available for the striate cortex.

In the following discussion, the lateral geniculate nucleus, the secondary visual cortex, the inferior pulvinar, and the somatosensory cortex, will be discussed with respect to specifying the analytic structure of their receptotopic maps.

The Optic Tract and the Lateral Geniculate

The magnification factor for the lateral-geniculate nucleus (LGN) is the same from as that for the striate cortex, up to a scale factor [9] and therefore is of the same form as Equation (3) above. Since cell density in both the LGN and the striate cortex is roughly constant with respect to eccentricity [18] most workers in the physiology of the geniculo-striate system have assumed that the origin of the magnification curve lies in the form of the density of the retinal ganglion cells themselves [9] which follow a distribution of the form of Equation (3). As in the previous discussion, it is evident that a (differential) magnification curve of the form of Equation (3) implies a logarithmic radial structure for the LGN retinotopic mapping, and thus raises the possibility that the source of the complex logarithmic structure of the striate cortex may lie in the LGN (and possibly the retinal ganglion cells). However, the available maps of the LGN show that this is not the case. Lines of equal azimuth and elevation from a grid which is approximately cartesian in the visual plane. They also form an approximately cartesian grid in the LGN [9]. The form of the

magnification curve is clearly in evidence in these plots, causing the central representation of the visual field to occupy a disproportionately large area. Nevertheless, the angular part of the complex logarithmic mapping is not present at the level of the LGN, and must occur in the projection of the LGN onto layer IVc of the striate cortex. Thus, the complex logarithmic structure of the striate cortex seems to be effected in two separate steps: 1) the form of the density of retinal ganglion cells, leading to a logarithmic *radial* structure in the optic tract, and LGN, 2) the projection of the LGN onto the cortex, where the angular reorganization of optic tract fibers is effected that leads to the final form of the striate cortex retinotopic map, as in Equation (4) above.

Secondary Visual Cortex

The quantitative data available on the secondary visual cortex is much less documented that that for the striate cortex. However, in recent years, the secondary visual cortex of the primate and the lower mammals has begun to be extensively studied. In a recent investigation of the organization of the second visual area (area 18) of the owl monkey, Allmann and Kaas [5] have published receptive field plots corresponding to straight line trajectories across the surface of visual area V–II. Their data is reproduced in Figure 2. It is evident from this figure that the image, under a straight line across the surface of V–II, is a spiral pattern of receptive fields in the tangent plane. Referring to Table 1, it can be seen that the mapping which images a spiral onto a straight line is the logarithmic conformal mapping.

In order to emphasize this point, Allman and Kaas' figure is reproduced in Figure 2. Also shown in this figure is a logarithmic spiral, for reference, and a semi-logarithmic polar plot of the receptive field centers corresponding to straight line trajectories in the periphery. Recalling that the equation of the logarithmic spiral is $r = Ae^{k\phi}$, it can be seen that the log of the radius should be linear with respect to the polar angle. The straight line plots (and the coefficients of linear regression) presented in Figure 2 support this statement. This procedure is not intended to be quantitative, but merely to support the observation that the spiral receptive field structure reported by Allman and Kaas does in fact represent a logarithmic structure.

Allman and Kaas emphasize in their paper that area V–I (area 17) is a "simple topological transformation of the visual hemifield" and call this a "first order transformation". They refer to V–II as a "second order transformation" because they feel that the simple retinotopy of the striate cortex is not maintained there. This is because area V–II forms a belt around the striate cortex (V–I) such that points above and below the horizontal meridian are mapped to points quite far apart in the cortical representation. However, aside from this peculiarity of the representation of the horizontal meridian, it would seem that the global structure of secondary visual cortex is described by a logarithmic spatial conformal mapping, as is the primary visual area.

In subsequent work, Allman and Kaas [6] have mapped the global receptive field structure of the medial visual area of the owl monkey. This data is shown in Figure 3.

Again each trajectory across the surface of the cortex corresponds to a logarithmic spiral trajectory in visual space. Also shown in Figure 3 is a plot on semilogarithmic paper of the radial versus the angular coordinates of the receptive field centers. These plots support the characterization of the receptive field trajectories as logarithmic spirals, analogous to those presented above for the secondary visual cortex (V–II). This characterization of the secondary visual cortex (area 18) and the medial visual area of the primate cortex as logarithmic conformal mapping is expected. Clasically, area 18 is described as a "mirror image" of area 17 [5], and the medial visual cortex is explicitly an image of the striate cortex [6]. The "mirror image" description of area 18 is called into question by the analysis of Allman and Kaas, cited above. Nevertheless, logarithmic spatial structure is clearly evident in these areas.

Somatosensory Cortex

The primate dorsal column-medial lemniscal component of the somatosensory projection subserves the modalities of touch and kinesthesis. One more synapse (at the level of the gracial or cuneate nuclei) than the visual system separates the cutaneous periphery from the primary cortical processor. The cutaneous periphery is represented by a map-like representation of the body, located in the post-central gyrus of the cerebral cortex (area S–1). This is termed the somatotopic map. The elegant experimental observations of Werner and Whitsel are of particular interest to the present discussion. Instead of determining the projection of the body to the cortex, Werner and Whitsel [34] measured the projection of straight lines of cells in the cortex (S–1) to the surface of the limbs. They found that "the receptive fields of the neurons progress, essentially, in bands around the limb, much as did the laces of a Roman soldier's footwear ...the sum total of all RF's represented in any mediolateral traverse of the cortical map describes a continuous spiral path around the limb". Coupling this observation with that of Mountcastle [21], that the size of the cutaneous

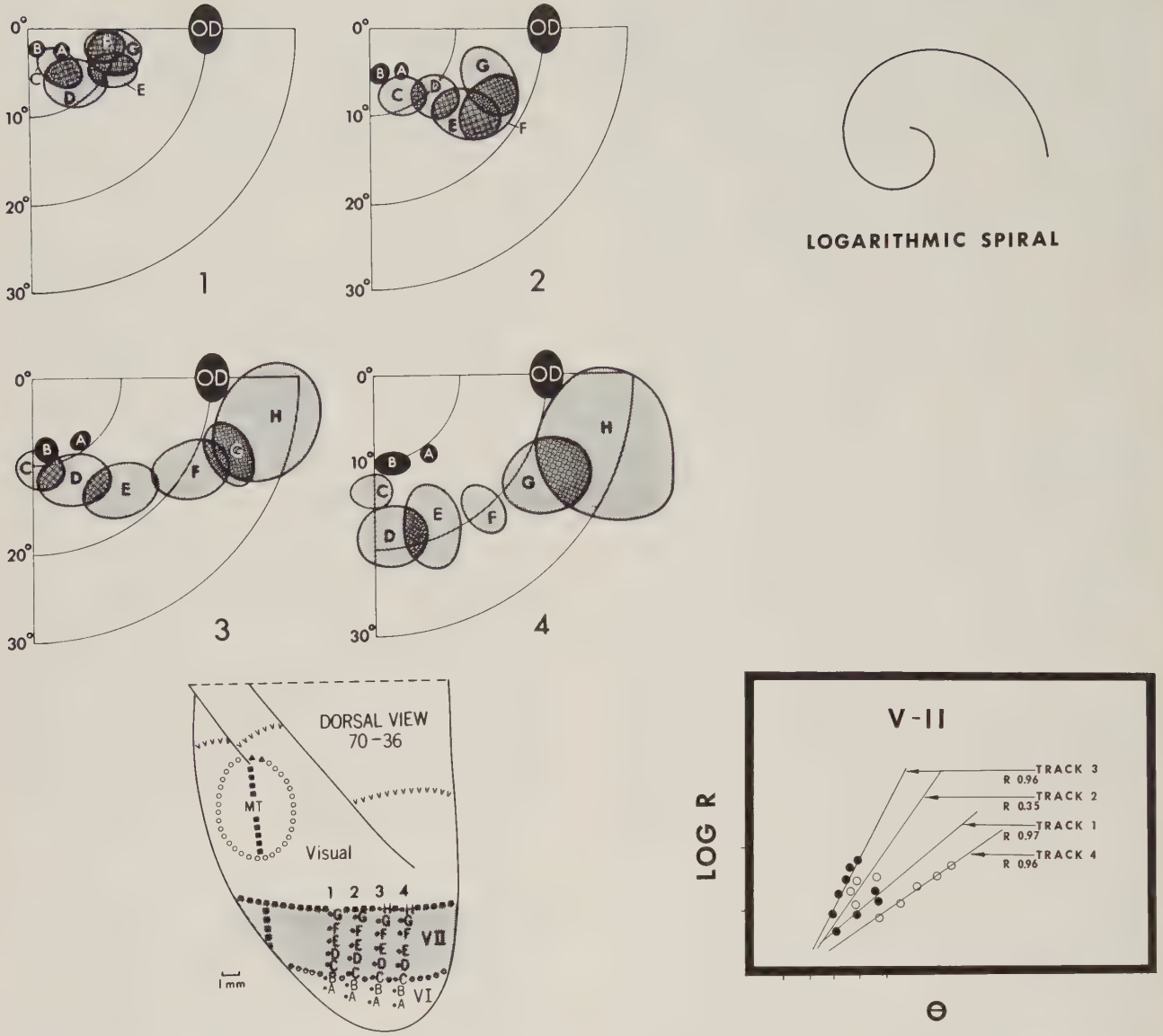

Fig. 2. On the left is reprinted the data of Allman and Kaas showing their results for the measurement of receptive field size and position, corresponding to straight lines across the secondary visual area of the monkey. The perimeter charts labeled 1, 2, 3, and 4 correspond to the anatomical locations indicated in the lower part of the figure. On the right is an example of a logarithmic spiral. Below the spiral is a semi-logarithmic plot of the radial position of the receptive field centers with respect to the corresponding angular positions. The hypothesis that these receptive field trajectories lie along logarithmic spirals is equivalent to the hypothesis that this semi-logarithmic plot should be linear. The coefficients of linear correlation to the best (least-squares) fit to a straight line are shown in the figure. The measurements were made directly from the figure of Allman and Kaas, starting from the first RF in V–II

receptive fields linearly increases with distance from the distal point of the limb, it is clear that the somatotopic mapping takes straight lines (in the cortex) to logarithmic spirals in the cutaneous periphery. This conclusion is supported by the further observations of Werner and Whitsel [35] that for rostro-caudal trajectories across the surface of S–1, "the sequence of receptive fields describe circular paths around the limb". With reference to Table 1 and Appendix 1, *the mathematical structure that this implies for the somatotopic mapping is the logarithmic conformal mapping, centered about the distal point of the limb.* To summarize the parallels between the visual and (somatic) maps: receptive field size for the visual (somatic) map scales linearly with distance from the foveal (distal) point of the receptor surface. Straight lines in the cortical representation correspond to receptive fields trajectories that are concentric circles, logarithmic spirals, or radial straight lines, depending on the orientation of the cortical

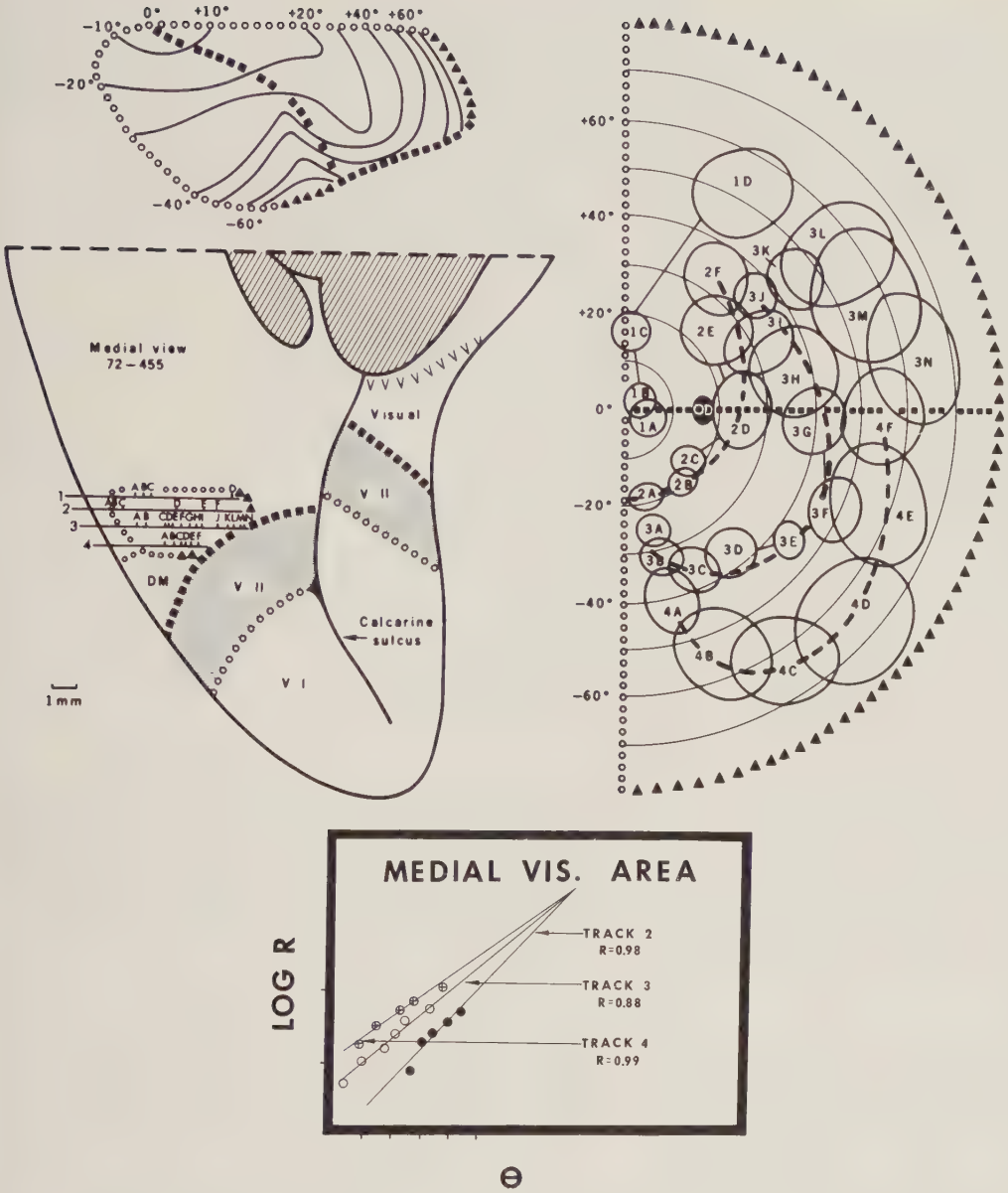

Fig. 3. Above is reprinted the figure of Allman and Kaas showing their measurements of receptive field size and position, corresponding to straight lines across the medial visual area of the monkey. On the right, sections of logarithmic spirals have been drawn through the receptive field trajectories (dashed lines), corresponding to the contiguous straight line tracks across the cortex shown on the right. Below is shown a semi-logarithmic plot of the radial position of the receptive field centers with respect to the corresponding angular positions. The hypothesis that these receptive field trajectories lie along logarithmic spirals is equivalent to the hypothesis that this semi-logarithmic plot should be linear. The coefficients of linear correlation to the best (least-squares) fit to a straight line are shown in the figure. The measurements were made directly from the figure of Allman and Kaas, starting from the first *RF* in the medial visual area

trajectories. Again, as in these case of the secondary visual areas, this discussion of the somatotopic mapping is qualitative; nevertheless, the observations of Werner and Whitsel, and Mountcastle imply that the analytic structure of the somatotopic mapping is the same as that found previously to account so parisomeously for the structure of visuotopic mappings.

The importance that this analysis has with regard to visual-haptic coordination of eye-limb activity is obvious, and will be discussed in more detail later in this paper. Additionally, the motor representation of the cortex is itself a mirror-image of the somatotopic representation. Thus, the visual, somatotopic, and motor maps of the primary cortical representation may be described, at least approximately, by the same mathematical function: the complex logarithm. A similar situation is known to exist in the superior colliculus, where superimposed visual, motor, somatic,

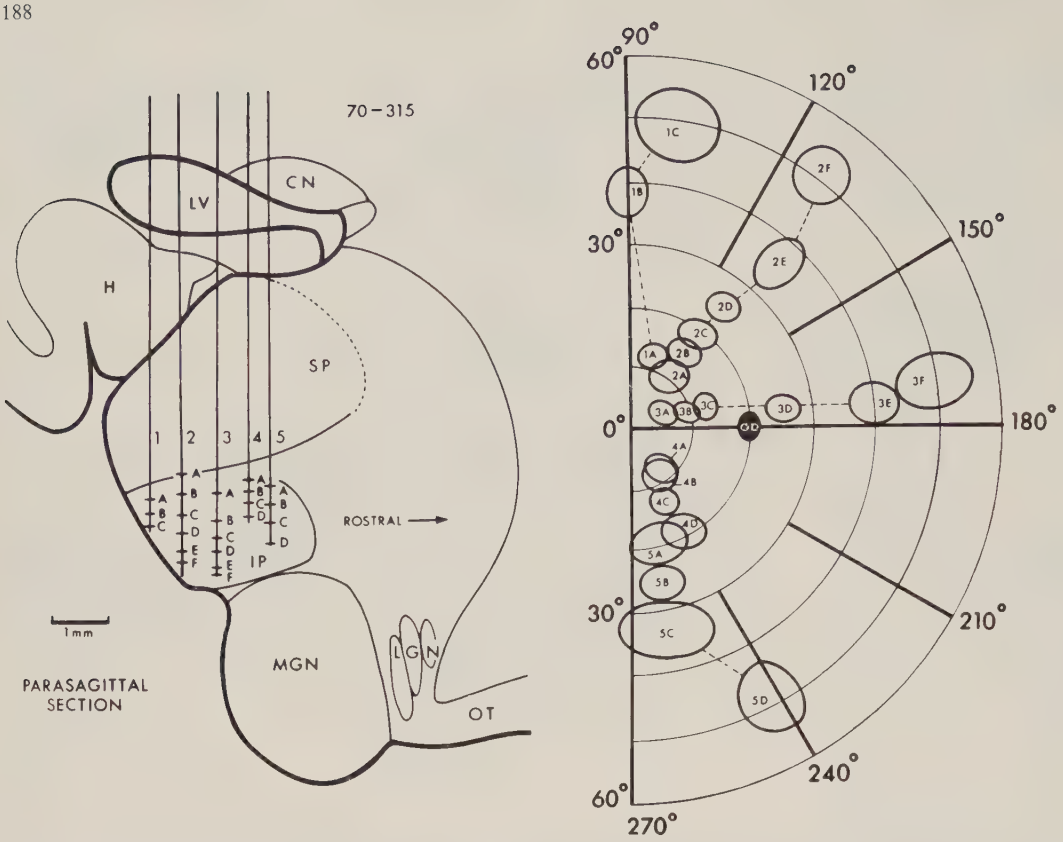

Fig. 4. A recent map of the retinotopic structure of the primate inferior pulvinar has been provided by Allman and Kaas. The visual field trajectories and the corresponding thalamic trajectories are shown in the figure. Clearly, parallel straight line trajectories in the inferior pulvinar correspond to radial straight line trajectories in the visual field. With reference to Table 1, this observation gives tentative support to the classification of the retinotopic structure of the pulvinar as a complex logarithmic map, like that of the primary and secondary visual cortex. It can be predicted from this data that, had the thalamic trajectories been rotated by 90 degrees, circular visual field trajectories would have been obtained; an intermediate angle of rotation would yield logarithmic spiral trajectories, as shown in Figures 2 and 3, for the secondary visual cortex

and auditory maps exist. These (linear) collicular maps are in registration with one another, both anatomically and functionally [13] and are thought to subserve the functional capabilities of the superior colliculis that have to do with visual orientation. The results of the present paper are very intriguing in this light, because they suggest the existence of a basic principle of sensory-motor function. A primary algorithm of the sensory system of the brain seems to be the creation of maps of the relevant sensory-motor spaces, in registration with one another. This is apparently the plan utilized by the (linear) tectal system and the (logarithmic) cortical system, as a general principle of sensory information processing.

Inferior Pulvinar

The inferior pulvinar is a large thalamic nucleus located in close proximity to both lateral geniculate and the superior colliculus. The pulvinar is a somewhat mysterious structure, both anatomically and functionally, and has been described as "terra incognita of the thalamus" [33]. Recently, it has been established that the inferior pulvinar receives a retinotopic projection of the visual field, in the primate [4]. A parasagital section of the brain, showing a number of straight line electrode trajectories, along with the corresponding receptive field plots, is shown in Figure 4.

It is clear from this figure that straight line trajectories in the brain correspond to radial straight line receptive field plots. Consequently, (with reference to Table 1 and Appendix 1), the retinotopic mapping of the pulvinar may be described, insofar as available data allows, by the complex logarithm function. This figure represents the only available data to date on the mapping of the inferior pulvinar, no magnification data is available. Consequently, the assignment of a complex logarithmic structure to the retinotopic map of the pulvinar is only tentative.

Allman and Kaas speculate that the source of the retinotopy of the pulvinar may lie either in the LGN, the superior colliculus, or the cortex. The puta-

tive logarithmic structure suggested in this paper would tend to group the pulvinar with the geniculostriate system, (which is generally logarithmic in structure) rather than with the tecto-fugal system (superior colliculus) which is generally linear in the structure of its retinotopy. Consequently the above analysis may provide some hints as to the function and anatomical relationship of this poorly understood thalamic visual area.

Sequence Regularity in the Striate Cortex

The previous analysis of the various receptotopic mappings of the sensory projection was concerned with the global nature of these mappings, with the mapping of entire receptor surfaces (the retina, the cutaneous surface) onto the corresponding central receiving areas. In the case of the striate cortex, the global logarithmic spatial structure holds at the level of layer IVc where the afferent input to the cortex arrives from the LGN [17]. In the surrounding laminae of the cortex, this precise topographic mapping is no longer valid; as is well known, the simple and complex cells in these laminae are responsive to straight line stimuli tuned about a range of angular orientation, and with definite stimulus velocity characteristics [16]. The local structure of the striate cortex has recently been examined in exquisite detail by Hubel and Wiesel in a series of paper culminating in their recent elegant demonstration of sequence regularity and the "hypercolumn" model [17]. A brief summary of this model, and the demonstration of sequence regularity among the simple cells of the striate cortex, will be presented, in order to demonstrate that the local mapping of cortical (LGN) afferents to the simple cells may be characterized as a logarithmic mapping, on the scale of a single hypercolumn.

In the original paper of Hubel and Wiesel [16] reporting the existence of simple cells, they speculated that the orientation tuning property of these simple cells arises from the convergence of a row of geniculate cells onto a single simple cell, as shown in Figure 5. Although the question of modeling the origin of simple cell orientation tuning is an active field of research in itself, the original model of Hubel and Wiesel is correct in its substantial details.

Recently, Hubel and Wiesel [17] have specified in detail the spatial arrangement of these columns, or slabs, of simple cells. The striate cortex of the macaque (and likely of the cat) is subdivided into two independent and overlapping series of columns termed "orientation slabs" and "ocular dominance columns". Each orientation slab represents tuning of simple cells over an angular range of 10–15 degrees. The width of these slabs is 25–50 μ. Thus, over a cortical traverse of from 0.5–1 mm, a complete traverse of the angular tuning variable (180°) is accomplished. This is the same distance which two ocular dominance columns span; the complete angular set of orientation tuning slabs, coupled with the binocular representation of two ocular dominance columns, is a functional unit of the striate cortex, called a hypercolumn.

This demonstration of "sequence regularity" shows, in the words of Hubel and Wiesel, that the striate cortex "after all is a remarkably uniform and homogeneous structure". In order to account for this regularity of orientation tuning, we have to deal with a situation as depicted in Figure 5. Each row of geniculate cells converges onto a slab of cortical cells, and the rows of geniculate cells rotate through regular angular increments, as the cortical representation moves through parallel slabs. It is obvious that in order to simultaneously satisfy the requirement of sequence regularity, as well as orientation tuning, the mapping that describes the wiring of LGN afferents to cortical simple cells must be very precisely constrained. In fact, with reference to Table 1, it is evident that the *formal mapping which takes equal angular strips to parallel strips is the complex logarithm.* If one describes the local mapping of LGN afferents (located in layer IVc) to simple cells (located in the surrounding laminae) by a local complex logarithmic mapping, about the hypercolumn center, then it is possible to satisfy the requirement that *rows of LGN cells converge onto simple cells in a spatially regular way such that equal angular increments in visual space correspond to equal linear steps in cortical space.* The analysis would seem to be particularly harmonious with the thinking of Hubel and Wiesel on this subject. They view each hypercolumn as a quasi-independent unit of the cortex... "capable of analyzing a region of visual field equal to the local field size" [17]. The image evoked by their model is of a cortex that is spanned by a mosaic of quasi-independent patches, each of which is responsible for the analysis of a small area of the visual field. The receptive fields are globally located across the surface of the cortex by a similar complex logarithmic mapping that describes the global relationship of the entire retinal surface to the cortical surface. The cortex is thus a concatenated logarithmic structure, whose structure in the large mirrors that of its local elements. This structure has a simple developmental rational, which will be discussed later in this paper. Furthermore, this concatenated logarithmic structure has some very potent information processing characteristics which may be of direct relevance to visual perception. These will now be illustrated.

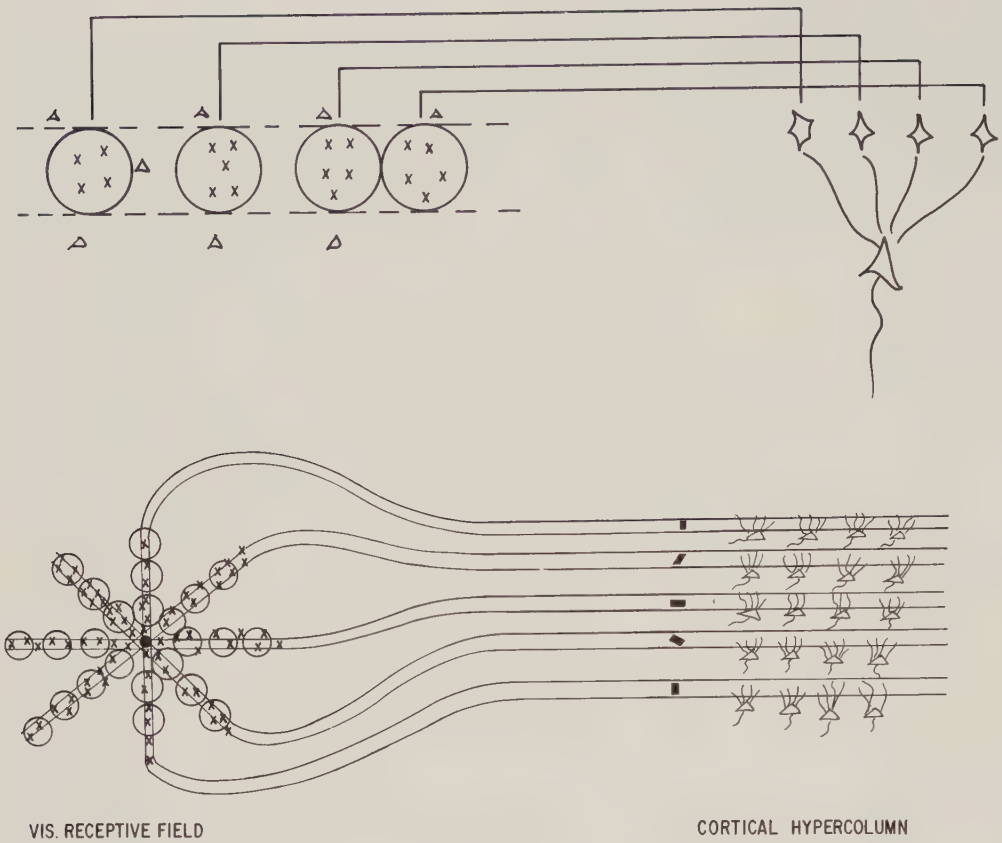

Fig. 5. Figure 5 shows a schematic representation of Hubel and Wiesel's suggestion for the origin of the orientation tuning of the simple cells of the striate cortex. A row of LGN cells (corresponding to a row of excitation at the retinal surface) converges onto a simple cell, whose response properties will then show orientation tuning. The recent demonstration of sequence regularity by Hubel and Wiesel is schematically represented in the bottom part of the figure. Here, a number of rows of LGN cells, arranged in equi-angular steps, are shown as they must project to the simple cells in order to maintain both orientation tuning and sequence regularity. The geometric statement of the sequence regularity property is that *equi-angular* steps in the visual (LGN) plane correspond to equal *linear* steps in the cortical plane. With reference to Table 1, it can be seen that the complex logarithm function provides this property. Consequently, it may be hypothesized that the projection, within the approximate area of representation of a receptive field at the cortex, of cortical afferents to simple cells, may be formally described as a local complex logarithmic mapping

Perceptual Consequences of Logarithmic Structure

Many years ago, Polyak [23] advanced the suggestion that there may exist a mathematical representation of the retina in the cortex. The present work supplies the mathematical form for this mapping: the complex logarithm of Equation (4). The anatomical and physiological thrust of this paper ends here. However, the fundamental reason for studying the anatomy and physiology of the visual system is to gain insight into its functional aspects. At present, our fundamental knowledge of perception is slight. Julesz [19] has said: "We still lack a physiological psychology of... visual perception. One of the greatest obstacles to its attainment is our inability even to guess the neural levels where certain perceptual phenomena might occur". One of these illusive perceptual phenomena is size invariance. We have no problem recognizing a familiar stimulus, whether it is near or far from us in space. The locus of retinal excitation due to the face of a friend is very different if that friend is sitting next to us, or is across the room. According to Sutherland [28], this size invariance property is one of the fundamental aspects of the visual system that any neural theory of perception must explain. The following discussion will demonstrate that the complex logarithm has a natural size invariance property. This mathematical fact, coupled with the previous anatomical and physiological analysis, suggests that the psychological property of size invariance may be subserved by the anatomical structure of the striate cortex. This is a hypothesis at present; it may be merely accidental that the mathematical properties of the retinotopic map automatically provides a size scaling effect. However, the lack of any viable neural theory for the existence of size invariance in visual perception makes this suggestion an attractive working hypothesis.

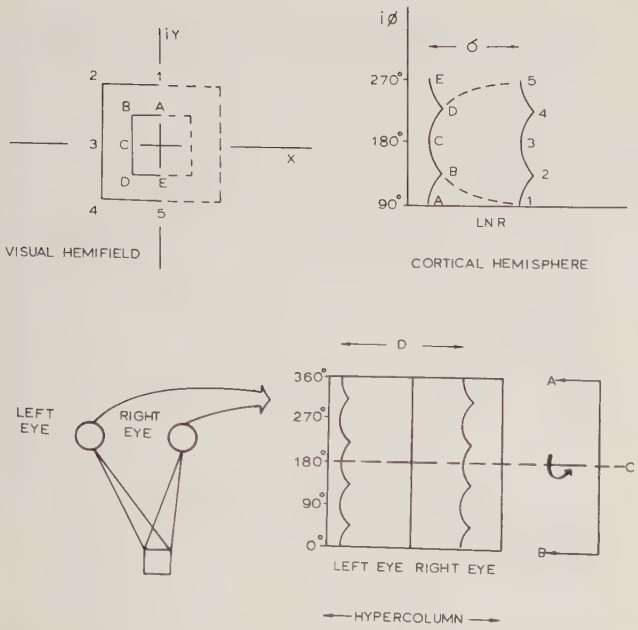

Fig. 6. The size-scaling property of the complex logarithm is graphically illustrated. The top of the figure shows the mappings of a large and small square, as they would appear across the surface of the unfolded and flattened cortex. The image of the square is an invariant; size dilitation merely causes this invariant image to shift across the cortical surface. The bottom of the figure shows the analagous mapping, under the local (hypercolumn) logarithmic mapping. In this figure, a small square element of the image space corresponding to a visual receptive field is depicted; the slightly different size of the retinal images are normalized by the complex logarithmic mapping. The relative shift, on the scale of a hypercolumn, is a possible cue for the disparity of the stimulus, since this relative shift is proportional to the relative difference in size of the left and right eye projections

A two dimensional contrast distribution (for example the grain of a photographic emulsion) may be represented as the locus of points (complex variable z_j) of each independent element of the pattern. The operator for size dilitation in complex variables is simple multiplication by a real constant k. The point z_j $(rje^{i\phi}j)$ is then taken to the point z_j $(kr_je^{i\phi}j)$. The locus of points $\log(z_i)$ is mapped to the locus $\log(kz_i)=\log(z_i)+\log(k)$. Thus, in the logarithmic (cortical) plane, size changes in the image plane reduce to a simple translation. The size of the image is thus invariant. This mathematical property of the complex logarithm is illustrated in Figure 6.

Chaikin and Wieman [10] have exploited this property of the complex logarithm, in a computer oriented pattern recognition approach. An earlier work in computer oriented pattern recognition [22] pointed out an additional useful property of processing pictorial information via the complex logarithm: multiplicative effects in the picture plane become additive effects in the logarithmic plane. Thus, the intensity distribution of a scene may be written as:

$$I(x, y)=R(x, y)\,U(x, y) \tag{9}$$

where R is the reflectance distribution of the stimulus and U is the illumination distribution of the ambient lighting. In the complex logarithmic plane the above relation becomes:

$$\log I(x, y)=\log R(x, y)+\log U(x, y)\,. \tag{10}$$

Thus, the reflectance and illumination may be treated separately and then additively combined. This simplification is not possible in the linear image plane.

These potent information processing capabilities of the complex logarithm have been exploited by workers in articial pattern recognition. As regards the problem of neural pattern recognition, it is not possible to state unequivocally whether or not the brain helps itself to the advantages of image processing outlined above. Nevertheless, it is a striking fact that both the primary and secondary visual cortex, the inferior pulvinar, and the somatotopic cortex as well, represent a complex logarithmic mapping of the sensory receptor surface onto a central neural surface. The preprocessing of spatial information by the complex logarithm may well be a crucial step in the functioning of the sensory system.

The size scaling property of the complex logarithm may have relevance to stereopsis. When the eyes fixate a stimulus, the two corresponding retinal projections will be, in general, of slightly different size. This size difference will be normalized by the complex logarithmic structure of the retinotopic map (both for the cortical projection as a whole, and for the local, hypercolumnar logarithmic structure described earlier). Psychological studies of steropsis have demonstrated the existence of this binocular "perceptual zooming" effect. Random dot stereograms may still be fused, even though the size scaling of the left and right images differs by up to 15% [19].

The need for a size-scaling mechanism in the visual system has been emphasized by a number of authors [19, 24, 25, 28]. Richards has pointed out that there is a correlation between size-scaling under changes in the vergence angles of the eyes (Emmerts Law) and binocular rivalry. He concludes that the neural site of size scaling precedes the site of binocular combination; it is after the chiasm, but before the cortex [24]. This is supported by the analysis of this paper, which locates the site of size-scaling to the projection of the LGN onto the striate cortex. It must be emphasized that the various psychological phenomena grouped under the general label of "size invariance" (Emmerts law, perceptual zooming; Sutherlands conception of size invariance) are diverse; no attempt is made to present a specific model. Rather, it is merely to be

pointed out that the cortical visuotopic mappings, which may be mathematically represented by the complex logarithm, operate on visual data that is automatically scaled for size, by the anatomical structure of the cortex. Whether this is an accident of anatomy, or has direct functional significance, is of course, a matter for further experimental study.

One of the principal cues for steropsis is binocular disparity; random dot stereograms which present a correlated (shifted) image to the left and right eyes create a very potent illusion of depth, as discovered by Wheatstone in the last century, and recently exploited by Julesz's [19] elegant investigations. Perhaps the neural basis of disparity as a cue for depth perception lies in the fact that the complex logarithm links a (cortical) shift to a (visual plane) size change, as derived above. Thus, the slightly different projections of the two eyes are normalized by the complex logarithm to the identical cortical pattern, with the shift proportional to the size difference, and ultimately, the disparity of the stimulus.

The fact that both the somatosensory and visual maps have the same logarithmic spatial structure has obvious relevance to the problem of cross-modal intergration of sensory information. Consider the following remark of Somjen [26]: "...What boggles the imagination is how the non-linearity of the somatic projection be matched with the different structure of the non-linearity of the visual projection. For while it is true that the somatic sensory figurines are more or less mirror images of the motor figurines, there is no correspondence whatsoever between the somatic projection and the visual projection. If eye-hand coordination is to be guided by the brain charts of visual space and of body-image, the two cannot be scaled by discordant nonlinear transformations."

Since a result of the present work is that both the primary sensory projection of each limb and the visuotopic projection of the retina, are *both* described by the complex logarithm, Somjens' particular objection to the perceptual relevance of the receptopic mappings is eliminated. As Gibson has emphasized from the psychological point of view the visual and haptic worlds are of "one piece" [14]. The fact that the visual and haptic maps available at the cortical level are of the same analytic structure provides a link between the psychology and the neurophysiology of the spatial senses.

The previous discussion of the complex logarithmic mapping and perception is speculative. Nevertheless, potentially rich insight into perceptual processes is apparent once the mathematical form of the retinotopic mapping is understood. This is particularly true since the topographical structure of the sensory system is at the present time felt to be of minor importance to sensory perception. This attitude is typified by the widely quoted study of Doty [12] (performed in 1958, before any of the "modern" results of cortical physiology had been accumulated), which concluded: "The topographical arrangement of the retino-cortical projection is in itself of minor importance or no importance in the visual analysis of geometrical patterns." Recently, Towe has analyzed this question with regard to columnar structure of visual and sensory-motor cortex. The crucial question concerns the fine-grain nature of the sensory mappings: are they continuous? Towe [30] remarks: "whether such (continuous) shifts, if reduced to the limits of experimental resolution, would continue to exhibit this (topographic) property has never been formally determined". This question, like many others in sensory neurophysiology, is still an open one. In the light of the results of the present work, it is timely to reopen, both experimentally, and theoretically, the issue of the relevance of the receptotopic mapping properties of the sensory system to the functional aspects of perception.

Morphology, Development and Logarithmic Spatial Structure

The assertion that something as forbidingly mathematical sounding as a logarithmic conformal mapping is a ubiquitous structural principle in the brain has a firm foundation in morphological biology. In the seminal work of D'Arcy Thompson [32], "On Growth and Form", first published over fifty years ago, the many common examples in biology of logarithmic spatial structure are discussed. They range from the beautiful shell of the Nautilus (and many other molluscans) to the horns of the ram, and the florets of the sunflower. Thompson suggests that there is a mathematical law of growth which is common to these diverse species. The characteristic shared is the property that a structure "shall widen and lengthen in the same unvarying proportions: and this simplest of laws is that which nature tends to follow. The shell, like the creature within it, grows in size but does not change its shape; and the existence of this constant ...similarity of form...may be made the basis of a definition of the equiangular (logarithmic) spiral".

Another important fact concerning logarithmic structure is that the real and imaginary parts of the complex logarithm are harmonic functions that are solutions to the diffusion equation (the laplacian) in polar coordinates [1]. Thus, a diffusion related growth process, in which a central active site releases a diffusing morphogenic substance would have its dynamics described by the complex logarithm. The lines of equal concentration would be given by

the real part of the complex logarithm and the lines of flow, or streamlines, by the imaginary part.

The suggestion that the striate cortex is a concatenated logarithmic structure (both locally and globally logarithmic) also has a simple interpretation in terms of developmental systems. Compound structure is frequently seen in biology, wherever an organism consists of a number of similar parts, and in which the development of the parts repeats more or less exactly the development of the whole organism. Examples are branching systems such as compound leaves, inflorescences, the lung trachae, blood vessels and so forth. Recently, the powerful mathematical apparatus of formal automation theory, or developmental languages, has begun to be applied to the growth and structure of biological organisms. Compound structure is particularly simple to model in this framework, and Lindenmeyer languages with a single recurrence formula have been found to be well suited to model compound developmental systems [15]. In any case, the compound logarithmic spatial structure suggested for the striate cortex in this work might be the simple expression of a common biological growth law.

The formal language theory approach to growth and development is essentially a combinatorial, finite mathematical method. Contrasting to this is the work of René Thom [31], who has tried to apply the differential topology of many dimensional spaces to the same general problem. In addition to these two lines of research, the present work suggests that the properties of a simple and familiar concept such as conformal mapping may in fact be useful in describing as complicated a morphological structure as the mammalian nervous system. These three lines of thought represent an initial assault on the formidable mathematical problem of describing form and structure in biology. It is fitting to close this work with a statement of D'Arcy Thompson, who wrote, over fifty years ago:

"How far even mathematics will suffice to describe, and physics to explain, the fabric of the body, no man can foresee. It may be that all the laws of energy, and all the properties of matter... are as powerless to explain the body as they are impotent to comprehend the soul. For my part, I think it is not so..."

Appendix 1

Associated with each analytic function $f(z)$, is a conformal mapping which affords an excellent visualization of the properties of the function $f(z)$. Conformal mapping enters naturally into many branches of mathematical physics, and in this way accounts for the immediate usefulness of complex function theory. When a conformal mapping is defined by an explicit analytic function $w=f(z)$, we naturally wish to gain information about the specific geometric properties of the mapping. One of the most fruitful ways is to study the correspondence of curves induced by the point transformation. The special properties of the function $f(z)$ may express themselves in the fact that certain simple curves are transformed into curves of a well known character. This information strengthens our visual conception of the mapping.

The complex logarithm may be written as:

$$f(z)=\ln z=\varrho+i\phi \tag{1}$$

using the polar form for the complex variable z. Thus, circles in the z plane (constant ϱ) are transformed into striaght lines in the w plane, parallel to the imaginary axis. Likewise, radial straight lines (constant ϕ) are transformed into straight lines in the w plane, parallel to the real axis. Logarithmic spirals in the z plane ($\varrho=Ae^{k\phi}$) are transformed to straight lines in the w plane, making a slope of $1/k$ with the real axis. Circles and radial straight lines are limiting cases of logarithmic spirals, with the constant k approaching 0 and ∞ respectively. Thus, in general, the complex logarithm maps logarithmic spirals to straight lines.

Acknowledgement. I would like to express my thanks to George Chaikin and Carl Wieman for sharing some of their results on the logarithmic mapping with me, to Bernie Karmel and Bob Thatcher for many useful discussions, to Gerhard Werner for useful comments and encouragement, and to E. Roy John for his intellectual and material support.

References

1. Ahlfors, L.: Complex analysis, New York: McGraw Hill 1966
2. Allman, J.M., Kaas, J.H.: A representation of the visual field in the caudal third of the middle temporal gyrus of the owl monkey (*Aoutus Trivirgatus*). Brain Res. **31**, 85–105 (1971a)
3. Allman, J.M., Kaas, J.H.: Representation of the visual field in striate and adjoining cortex of the owl monkey (*Aotus Trivirgatus*). Brain Res. **35**, 89–106 (1971b)
4. Allman, J.M., Kaas, J.H.: A representation of the visual field in the inferior nucleus of the pulvinar in the owl Monkey. Brain Res. **40**, 291–302 (1972)
5. Allman, J.M., Kaas, J.H.: The organization of the second visual area (V–II) in the owl monkey: A second order transformation of the visual hemifield. Brain Res. **76**, 247–265 (1974)
6. Allman, J.M., Kaas, J.H.: A representation of the visual field on the medial wall of occipital-parietal cortex in the owl monkey. Science **191**, 572–575 (1976)
7. Apter, J.T.: Projection of the retina on the superior colliculus of cats. J. Neurophysiol. **8**, 123–134 (1945)
8. Arbib, M.A.: The metaphorical brain. New York: Wiley 1972
9. Bishop, P.O., Kozak, W., Levick, W.R., Vakkur, G.J.: The determination of the projection of the visual field onto the lateral geniculate nucleus in the cat. J. Physiol. **163**, 503–539 (1962)
10. Chaikin, G., Wieman, C.: Submitted to Computer Graphics and Information Processing (1976)
11. Daniel, P.M., Whitteridge, D.: The representation of the visual field on the cerebral cortex in monkeys. J. Physiol. **159**, 203–221 (1961)
12. Doty, R.W.: Functional significance of the topographical aspects of the retino-cortical projection. In: The visual system: Neurophysiology and psychophysics, pp. 228–245 (Jung, R. ed.) Berlin - Göttingen - Heidelberg: Springer, 1961
13. Drager, U.C., Hubel, D.H.: Topography of visual and somatosensory projections to mouse superior colliculus. J. Neurophysiol. **39**, 91–103 (1976)
14. Gibson, J.J.: The senses as perceptual systems. Boston: Houghton Miflin 1966
15. Herman, G.T., Rozenberg, G.: Developmental systems and languages, Amsterdam, North Holland 1975

16. Hubel, D.H., Wiesel, T.N.: Receptive fields, binocular interaction and functional architecture in the cats visual cortex. J. Physiol. **160**, 106–154 (1962)
17. Hubel, D.H., Wiesel, T.N.: Sequence regularity and geometry of orientation columns in the monkey striate cortex. J. comp. Neurol. **158**, 267–293 (1974a)
18. Hubel, D.H., Wiesel, T.N.: Uniformity of monkey striate cortex: A parallel relationship between field size, scatter, and magnification factor. J. comp. Neurol. **158**, 295–302 (1974b)
19. Julesz, B.: Foundations of cyclopean perception. Chicago: University of Chicago Press 1971
20. Lorente de No: Anatomy of the eight nerve: the central projection of the nerve endings of the internal ear. Laryngoscope **42**, 1–38 (1933)
21. Mountcastle, V.: Modality and topographic properties of single neurons of cats somatic sensory cortex. J. Neurophysiol. **20**, 408–434 (1957)
22. Oppenheim, A.V.: Nonlinear filtering of multiplied and convolved signals. Proc. IEEE **56**, 1264–1291 (1968)
23. Polyak, S.: *The retina.* Chicago: University of Chicago Press, 1941; Chicago: Chicago Press, 1957
24. Richards, W.: Apparent modifiability of receptive fields during accomodation and convergence and a model for size constancy. Neurophysiologia **5**, 63–72 (1967a)
25. Richards, W.: Size scaling and binocular rivalry. J. Opt. Soc. Amer. **57**, 576 (1967b)
26. Somjen, G.: Sensory coding in the mammalian nervous system. New York: Appleton-Century-Crofts 1972
27. Stone, J.: A quantitative analysis of the distribution of ganglion cells in the cats retina, J. comp. Neurol. **124**, 337–352 (1965)
28. Sutherland, N.S.: Outlines of a theory of visual pattern recognition in animals and man. Proc. roy. Soc. B **171**. 297–317 (1968)
29. Talbot, S.A., Marshall, W.H.: Physiological studies on neural mechanisms of visual localization and discrimination. Amer. J. Ophthal. **24** 1255–1263 (1941)
30. Towe, A.L.: Notes on the hypothesis of columnar organization in somatosensory cerebral cortex. Brain Behav. Evol. **11**, 16–47 (1975)
31. Thom, R.: Structural stability and morphogenesis. New York: W. A. Benjamin 1975
32. Thompson, D'Arcy: On growth and form. Cambridge: University Press 1961
33. Walker, A.E.: Normal and pathological physiology of the thalamus. In: Introduction to stereotaxis with an atlas of the human brain pp. 291–316, Vol. I. Schaltenbrand, G., Bailey, P. (Eds.) Stuttgart: Thieme 1959
34. Werner, G., Whitsel, B.: Topology of the body representation in somatosensory area S–I of primates. J. Neurophysiol. **31**, 856–869 (1968)
35. Werner, G., Whitsel, B.C.: Functional organization of the somatosensory cortex. In: Handbook of Sensory Physiology Vol. II, pp. 621–700 (Iggo, ed.), Berlin - Heidelberg - New York: Springer 1973
36. Woolsey, C.N., Marshall, W.H., Bard, P.: Representation of cutaneous tactile sensibility in the cerebral cortex of the Monkey as indicated by evoked potentials. Bull. Johns Hopkins Hosp. **70**, 399–441 (1942)

Received: August 26, 1976

Eric Schwartz, PhD
New York Medical College
Brain Research Laboratories
Flower and Fifth Avenue Hospitals
Fifth Avenue at 106th Street
New York, NY 10029

Biol. Cybernetics 25, 195–203 (1977)

Biological Cybernetics

A Computer Simulation Model of the Afferent Part of the Visual Foveation System*

F. J. Tolkmitt
Max-Planck-Institut für biophysikalische Chemie, Göttingen, FRG

Abstract. It is argued that the duplicity notion of visual perception refers to two separate neural systems, the foveation and identification system. A computer simulation model for the afferent part of the foveation system was developed. It consists of a receptive matrix and a retinal, geniculate, and cortical network. Within the networks neurons were substituted by threshold gates. The retinal information of the model can be controlled by the geniculate network and is analyzed with regard to stimulus orientation and movement by hypercolumns of cortical gates. The implemented columnar organization preserves retinocortical continuity. Retinal and cortical information together provide the necessary prerequisites for the efferent part of the foveation system.

On the basis of studies in the vertebrae retina Schultze (1866) formulated the duplicity theory of visual perception which was based on the fact that the eye consists of two receptive systems, the rods and the cones. The rods populate the retinal periphery; they act at low luminances, are sensitive to moving objects without regard for detail, and leave little impression on consciousness. The cones occupy the fovea and taper off toward the periphery; they act at high luminances, provide color vision with high acuity, and give rise to full awareness. This duplicity notion has been supported by many psychophysical data in areas like dark adaption, flicker detection, spectral sensitivity, etc.

Lately, this notion has taken on a different dimension. Apparently the two sections of the retina subserve different behavioral functions. Peripheral vision seems to guide orienting behavior and triggers localization or foveation (Schiller and Stryker, 1972) of relevant stimuli which are subsequently analyzed or identified by foveal vision (Trevarthen, 1968). Ablation studies in the hamster have shown that stimulus foveation is mediated by the superior colliculus while its identification takes place in various parts of the visual cortex (Schneider, 1969). Judged by their orienting behavior, animals with ablated superior colliculus appear to be blind, even though they are perfectly capable to discriminate stimuli that are projected into their fovea. On the other hand, undercutting the visual cortex does not affect their orienting behavior but renders them incapable of performing visual discrimination tasks.

The behavioral consequences of selected ablation of superior colliculus and visual cortex suggest that foveation and identification of stimuli might be mediated by separate neural fiber systems. This seems to be the case in light of recent neurophysiological data. To clarify this point a quick glance at neural information processing is necessary. In general, receptors translate changes in luminous intensities into potential differences which are processed locally within the neural network of the retina. The results of the retinal analysis are sent via ganglion cells to the superior colliculus and through the lateral geniculate body to the visual cortex. The ganglion cells are driven by receptive fields (RF) with center-surround properties and have been classified into *X* and *Y* fibers (Enroth-Cugell and Robson, 1966) which pick up predominantly foveal and peripheral information, respectively (Stone and Holländer, 1971). The *X* fibers transmit to the visual cortex only, while the *Y* fibers send their information to the cortex and the superior colliculus (Stone and Dreher, 1973). Even though both fiber systems project into the visual cortex they remain essentially separate from retina through lateral geniculate body to cortex (Cleland et al., 1971). Their main functional differences are in terms of conduction times and response properties. The *X* fibers are slow conducting and give sustained responses to changes in illumination; the *Y* fibers are fast conducting and of transient response nature. Ikeda

* Supported by a grant from the Deutsche Forschungsgemeinschaft

and Wright (1974) have proposed that the latter are involved in the perception of movement and change while the former are suggested to deal with the detection of form.

There is evidence that even within the visual cortex the two sets of information are processed more or less independently of each other. In case of the cat it is known that area 17 receives *X* and *Y* afferents and area 18 only *Y* afferents (Stone and Dreher, 1973). Both areas send projections to the superior colliculus (Gilbert and Kelly, 1975) and the respective output cells seem to be under the control of the *Y* afferents even in area 17 (Singer et al., 1975). These efferent fibers enter the deeper layers of the superior colliculus while the superficial ones are innervated by the retinal *Y* fibers. These two streams of information merge within the superior colliculus (Wurtz et al., 1975) and the result enters the efferent pathways to the motor system of the brain stem.

So far it is still unclear how the superior colliculus performs the selection of pheripheral stimulus for foveation. Nevertheless, it seems justified to extrapolate the duplicity notion further. It is proposed that the rod-cone dichotomy in the retina is preserved throughout the whole neural processing chain and that it manifests itself in two separate visual systems, one for orienting behavior (foveation) and the other for pattern analysis (identification). The first one is driven by peripheral stimulation which is transmitted via fast conducting *Y* fibers to the superior colliculus and the visual cortex. At the latter it picks up preliminary information about stimulus features and routes it back to the superior colliculus for decisions on foveation. The second one is the identification system which receives its stimulation mainly from the fovea and sends it via slow conducting *X* fibers to the visual cortex only, from where it is cascaded through several processing stages for the purpose of form and color identification.

The Model

This paper presents the first step toward the development of a simulation model of the foveation system. The objective is a camera-computer system that consist of an afferent and efferent part. The afferent part is already existent and consists of a receptive matrix, the *Y* projections into the superior colliculus and the striate cortex, as well as the recurrent cortical information to the superior colliculus. The efferent part needs to be developed and is going to consist of a collicular decision processor, an efferent command repertoire, and a motor system for foveation of the camera (see Fig. 1). The system as a whole will foveate on its own accord on simple peripheral stimuli.

The following contribution is a description of the afferent part of the envisaged operating system. Throughout its development care was taken to emulate the structural and functional aspects of the mammalian visual system which will be referred to as the real system. This was done with the assumption that accurate simulation of the real system provides a good chance to approximate its operating characteristics. The feasibility of such an approach was demonstrated in an earlier model by Tolkmitt and Hammond (1975) which generated place, velocity, and direction information about peripheral stimuli. However, velocity and direction sensitivity were achieved by means of neuron substitutes that did not have sensitivity thresholds but were fired by specific input patterns.

An inconvenience inherent in all computer simulation models of neural networks is the fact that the neural units of such models are processed successively while neurons in the real system communicate with each other simultaneously. For that reason the continuous flow of information interchange within the model had to be fractionated into processing cycles, during each of which a sequential input-output mapping for all neural units is performed. The processing cycle constitutes therefore the basic time rate of the model.

The current model is built out of threshold gates which copy the functional characteristics of neurons. These characteristics are briefly as follows. The medium of information transmission within the neurons are temporal sequences of electrical impulses referred to as spontaneous firing rates (SFR). Communication between them takes place at synapses where the SFR of any given neuron can be either increased or decreased through excitatory or inhibitory stimulation of preceeding neurons. The threshold gates in the present model have SFRs that consist of continuous trains of zeros which are sporadically interrupted by ones, symbolizing the electrical impulses. As many input gates as desireable can converge on to a given threshold gate. They can be of either excitatory or inhibitory nature and their individual effects may be either equal or else are differentially weighted. In either case, during each processing cycle the algebraic sum of all inputs is compared against an arbitrarily chosen threshold value. If the sum exceeds the threshold the gate generates a pulse during that cycle.

The simulation model has in correspondence with the real system a receptive matrix, and a retinal, geniculate, and cortical network. To avoid confusion when referring to the simulation model the gates of the various networks are mnemonicized as gangs, genics, and corts.

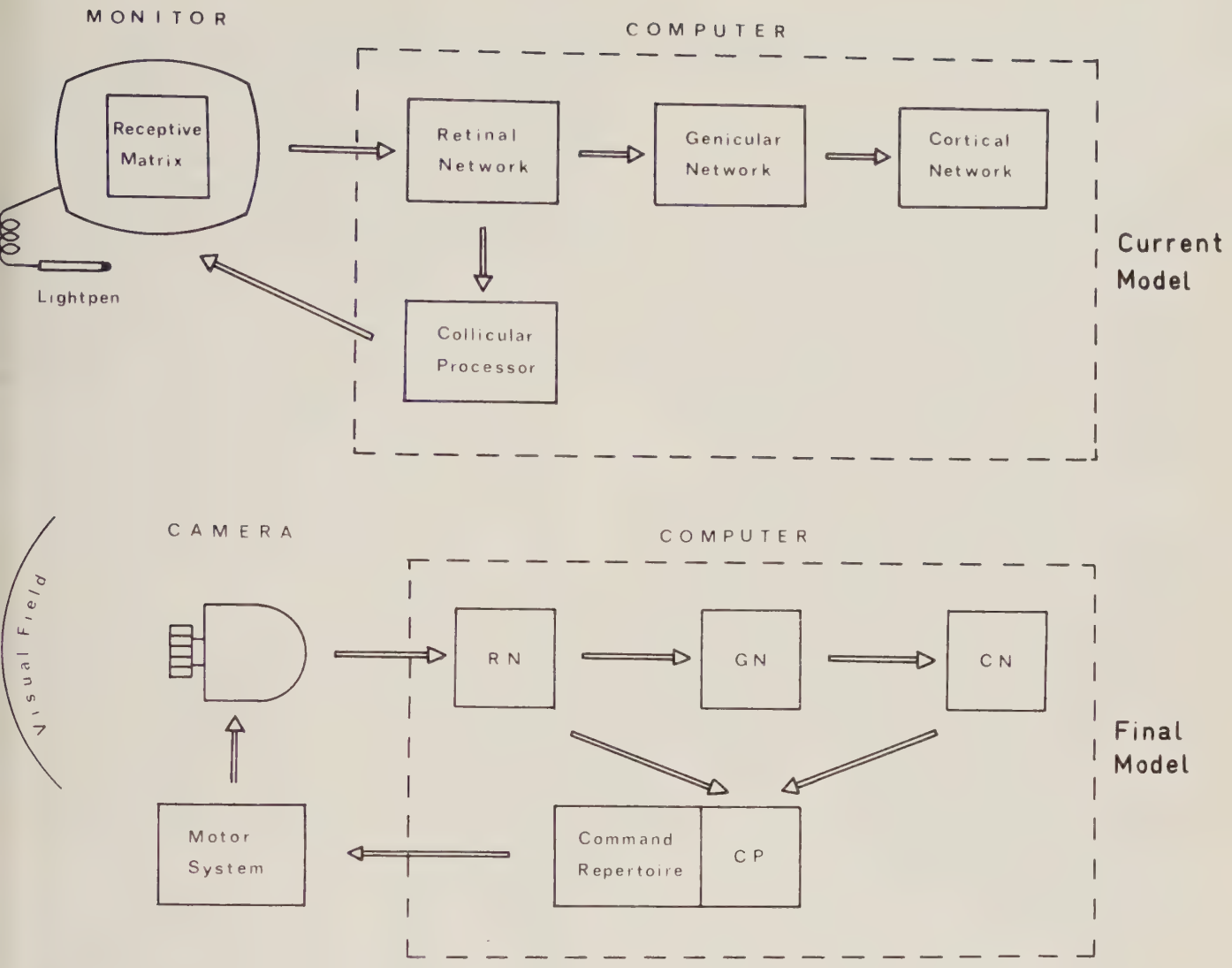

Fig. 1. The current and planned versions of the simulation model

The Retina

The circumference of a 32×32 receptor matrix is outlined on the face of a computer monitor and the receptors are sensitive to stimulation by a light pen. The equidistantly arranged receptors are grouped into overlapping receptive fields (RFs) of hexagonal shape with seven center and twelve peripheral receptors (see Fig. 2B). These RFs generate better cortical responses than the remaining ones that are outlined in Figure 2. The overlap between RFs is maximum, i.e., each receptor except for the marginal ones occupies the center of an RF. This means there are nearly as many RFs as there are receptors and each RF feeds into an on-center and off-center gang.

When not stimulated the gangs have an SFR of one spike per eight processing cycles. This is an arbitrary

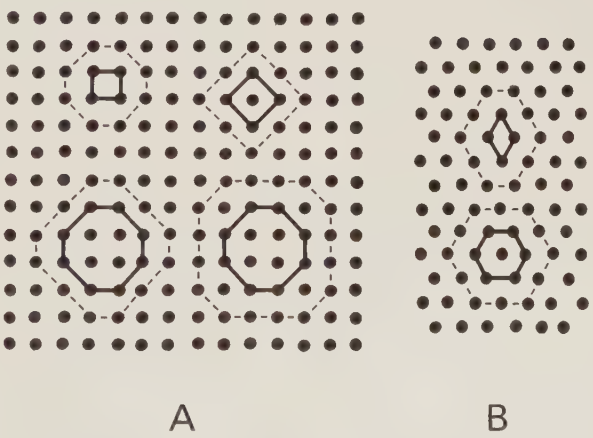

Fig. 2. Receptive fields with rectangular **A** and equidistant **B** arrangement of receptors. The hexagonal field in **B** was used in this model

value that could easily be changed. Changes in the RF input are modulated on to this SFR by means of the function

$$FR = \alpha(CN - CF/2) - \beta(PN - PF/2),$$

where FR stands for firing rate; C and P stand for the number of center and periphery receptors that are turned on (N) or off (F), where an off event carries only half the weight of an on event; α and β are weights that affect the extent of the modulation or the length of the signal; they are assigned positive or negative signs depending on whether the to-be-modulated gang is of on-center or off-center type, respectively. The number zeros or ones which are modulated on to the SFR of a gang is equivalent to the integer value of FR. Whether they will be all zeros or ones depends on the sign of FR as well as on the type of the gang.

According to this formula an antagonistic response of transient nature is modulated on to the SFR of a gang, depending on whether the center or periphery of its RF is stimulated. Transient responses to stimulation of antagonistic center-surround RFs are essentially the characteristics of *Y* cells in the real system. At the moment the values of α and β are chosen such that the maximum stimulation of either center or periphery of an RF will generate an absolute FR value of 16. It implies that the longest signal can consist of either 16 zeros or ones, indicating maximum inhibition or excitation, respectively. In general, the actual length of the gang signal that any RF will produce depends on its number of receptors that are either turned on or off. In this way the gangs give a topographic record of activity patterns on the receptive matrix, be they of *on* or *off* nature.

The translation of RF stimulation into SFR modulation of the gang could also be performed by means of gate networks, as was done in the model of Tolkmitt and Hammond (1975). However, incorporation of such networks increases the time for each processing cycle and makes the retinal system more rigid with regard to desired experimental changes of its translating properties.

Geniculate Net

On its way to the cortex the output of the gangs passes through the geniculate body. The physiological convergence of ganglion on geniculate cells is such that always one or two provide excitatory input while the surrounding ganglions have inhibitory effects (Singer and Creutzfeldt, 1970). The inhibition reaches the geniculate cell via interneurons which are driven by the surrounding ganglions as well as by geniculate collaterals (Szentágothai, 1973).

This neural net is implemented in terms of threshold gates in such a way that any particular genic is excited by just one gang and inhibited by an intergate. The latter is driven by several surrounding gangs and the genic's own collateral (see gating circuitry in Figure 3). The main function of such a network is that of signal attenuation. Without the inhibitory surround the gang would pass its signal faithfully to the genic. Because of the inhibitory intergate the signal is subjected to a certain attenuation, the extent of which depends on the sensitivity or threshold value of the intergate. If the collective input to the intergate exceeds its threshold value, it generates an output pulse which on the next processing cycle stops an excitatory pulse from passing through the genic. The intergates in this model have at least seven inputs, six gangs and one collateral genic (see Fig. 3). A threshold value of seven would render such an intergate insensitive to its input while at the next lower threshold value it would fire if all seven inputs were pulsing. An intergate with such a low sensitivity would practically have no effect on the signal transfer across the genic, while at the highest sensitivity setting, a threshold value of zero, the intergate would essentially block information passage through the genic. In general, increasing intergate sensitivity yields increasing signal attenuation.

The nature of the attenuation is further affected by various combinations of converging on-center and off-center gangs. As long as the input to intergates is homogeneous with regard to gang type, one can distinguish between four possible combinations of excitatory and inhibitory convergence: on-center excitation and on-center (N/N) or off-center (N/F) inhibition; and off-center excitation and on-center (F/N) or off-center (F/F) inhibition. The first and last type of convergence (N/N and F/F) are of synergistic nature, the two middle ones (N/F and F/N) are of antagonistic nature. As the type of excitation is irrelevant with regard to its attenuation, one would expect functional differences only between synergistic and antagonistic convergence. When the two were tested it was found that with increasing sensitivity of the intergate the gain of attenuation was faster for synergistic than for antagonistic convergence. As a result, the information cut-off point occurred earlier for the former than for the latter. At intermediate sensitivity settings of the intergate, signal attenuations was slightly greater for synergistic convergence. This was true for stationary as well as for moving stimuli. One could assume that this difference in attenuation gradually disappears if one were to replace the homogeneous input to the intergates with gangs of antagonistic center-surround structure (Singer and Creutzfeldt, 1970).

So far it was implicitly assumed that the number of surrounding gangs feeding into an intergate was constant. Varying that number gives rise to changes in the width of the inhibitory annulus that surrounds the RF

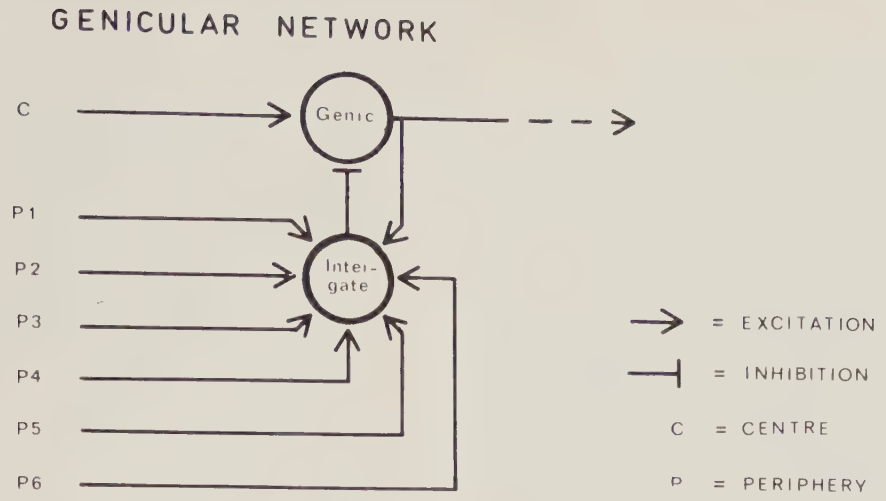

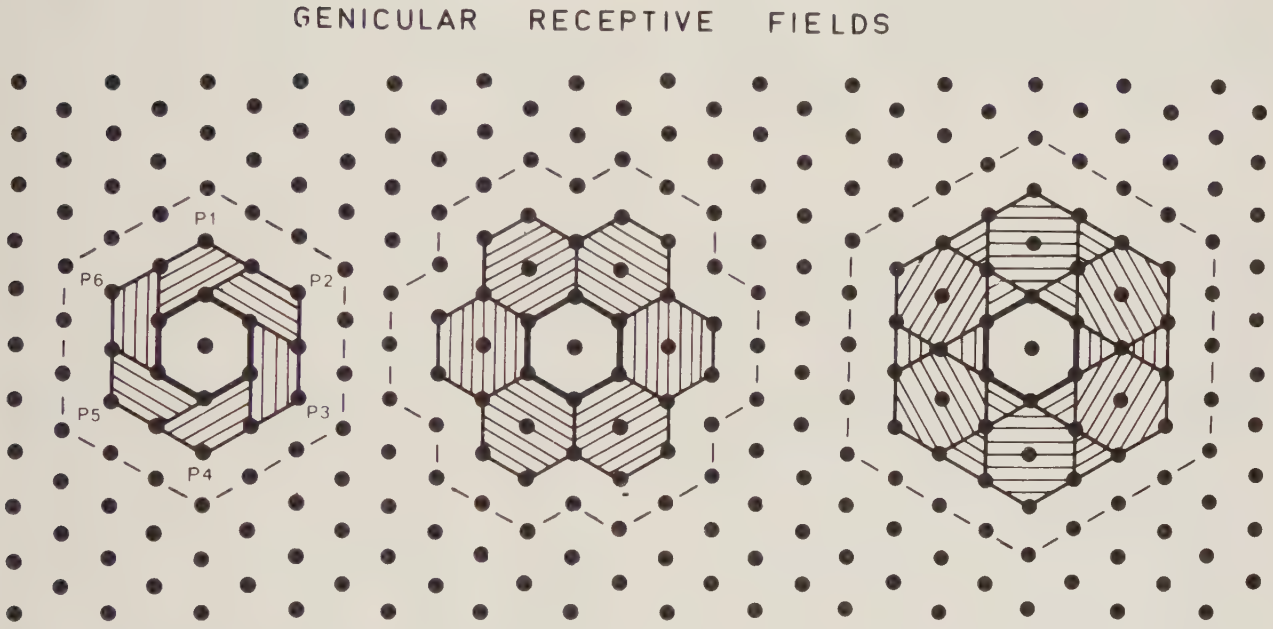

Fig. 3. Circuitry of the geniculate network with three corresponding RFs. The increasing inhibitory annulus (hatched area) results from an increasing number of gangs that feed into the inhibitory intergate. The hatched fields represent the centers (some are partly covered) of individual surrounding gangs and the broken line their joint periphery

of the excitatory gang. To test the effect of such a variation, three sets of surrounding gangs were fed into separate intergates, the layout of which is given in Figure 3. The hatched belt always indicates the extent of the RF centers of the surrounding gangs which yield inhibition via the intergate. The area within the hatched belt is the RF center of the exciting gang. No systematic changes with regard to signal attenuation were noticed for stationary stimuli. However, when using moving stimuli width of annulus and speed of stimulus correlated positively. Specifically, signal attenuation was more pronounced when fast moving stimuli traversed a geniculate RF with a wide rather than a small inhibitory annulus.

All in all, except for the signal attenuation, the geniculate network does not seem to affect the visual information in a way that might be of importance to its pattern analysis. This is in agreement with the physiological results on the ground of which the geniculate body is considered to be mainly a gating station for retinocortical information transfer (Doty et al., 1972). Behavioral data on the macaque monkey have shown that stimulation of the reticular formation improves tachistoscopic discrimination significantly (Fuster and Uyeda, 1962). It is assumed that during voluntary eye movement the reticular formation first blocks information passage through the geniculate body and augments it as soon as the eyes have reached the resting position.

Such a mechanism could be implemented in the current simulation model by globally affecting the sensitivity of all intergates. One way of doing this would be through common control lines to all intergates. Feeding into each intergate as many control lines as it receives gang inputs and setting their threshold values individually at half the number of all their inputs, provides the possibility to manipulate the sensitivity of all intergates. Without any control input the intergates would be insensitive because the gangs alone could not exceed their threshold values. Hence, there would be no geniculate inhibition and the retinal information could pass freely to the cortex. On the other hand, if all control lines were continuously active, any gang could generate geniculate inhibition and thereby block the retinocortical signals. Taking into consideration that synergistic and antagonistic convergence yield differential attenuation, it would be even possible to curtail selectively one stream of information while leaving the other relatively unaffected.

Cortical Net

The striate cortex is commonly divided into six layers, some of them are further subdivided. Within these layers two main classes of cells have been identified, stellates and pyramidals. Stellate cells are probably responsible for lateral distribution of information while pyramidal cells are involved in vertical information processing which is the mainstream in terms of processing analysis. Layer IV receives the main bulk of the geniculate input and exists entirely of stellate cells. From here information is distributed in both vertical directions. The individual layers are probably performing different analytical tasks.

The main hypothesis with regard to the functional structure of the visual cortex was put forward by Hubel and Wiesel (1962). They proposed a horizontal or hierarchical and a vertical or columnar organization. The hierarchy refers to the fact that the geniculate input to layer IV cascades in both directions through horizontal layers of cells which increase in complexity from simple through complex to hypercomplex and extract stimulus features like orientation, size, movement, and direction. The columnar organization was first proposed by Mountcastle (1957) who found the somatosensory cortex to be partitioned into modality specific, vertical columns which represent the receptive surface in discrete units. Penetrating electrodes vertically through the striate cortex of cats and monkeys, Hubel and Wiesel (1963, 1968) recorded cells of equal orientation specificity and concluded that the visual cortex too is partitioned into columns. They further suggested that there are two classes of superimposed but independent columns which represent stimulus orientation and ocular dominance.

The most controversial aspect of the columnar hypothesis is the implicit mosaic representation of the retina and its corollary that cells in adjacent columns should vary in discrete monotonic jumps along the relevant stimulus dimensions. Hubel and Wiesel (1974) claimed that this is the case for cells in the striate cortex of the monkey. However, they are squeezing the columnar concept to its limit since their orientation columns are only 25 to 50 μ wide which comes close to the diameter of a single cell. Similar data from the cat seem to suggest that the distribution of retinal points and the orientation specificity across the striate cortex are not discrete but continuous (Albus, 1975).

In spite of the recent objections against the columnar hypothesis (Towe, 1975) it was decided to implement such an organization for two reasons. First, a partitioned retinal representation in the cortex is economical in as much as one can avoid representational overlap which keeps the required gating circuit at a minimum. Second, the cortical columnes used in the present simulation model preserve continuity of retinal points across the cortex.

The nature of the implemented columns is such that each of them analyzes a small section of the receptive matrix in terms of all possible stimulus orientations and movement directions. It is therefore more appropriate to refer to them as hypercolumns since each of them consists of orientation columns of six possible angles. At the moment there are five layers of corts; one base layer of simple corts which provides inhibitory input to two layers of complex as well as hypercomplex corts which receive additional direct or indirect excitatory input from the genics. In Figure 4 is shown a cut through the layer of simple corts which corresponds to the fourth layer in the real cortex. The seven circular patches of corts are the bases of the hypercolumns and furthermore each cort is a member of an orientation column as indicated by the bars. One can distinguish six angles of orientation sensitivity and within each hypercolumn there are either three or four corts for each of the six orientations. Their RFs are always on a line through the midpoint of the hypercolumnar receptive surface and together they cover the whole width of it. Adjacent hypercolumns have adjacent and nonoverlapping receptive surfaces. Accordingly, the visual information contained in the receptive matrix is subdivided into small chunks and all of them are processed in parallel by identical hypercolumns.

The hypercolumns are a result of an orderly projection of genics on to corts. The subdivision of the receptive matrix was achieved by partitioning of the genics into groups of always 18 neighbouring gates,

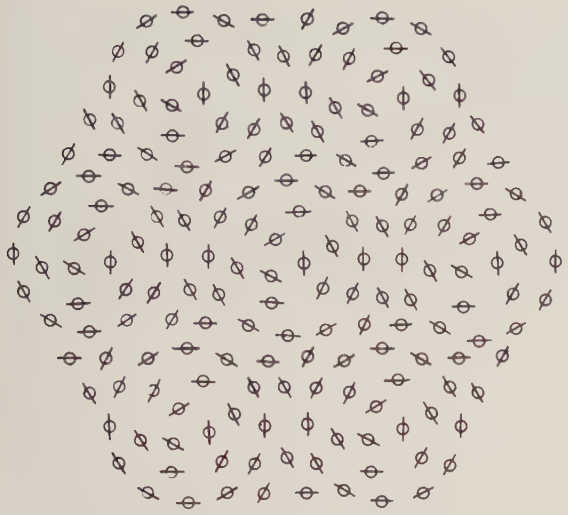

Fig. 4. Hypercolumnar arrangements of the corts. The bar through each gate indicates its orientation sensitivity

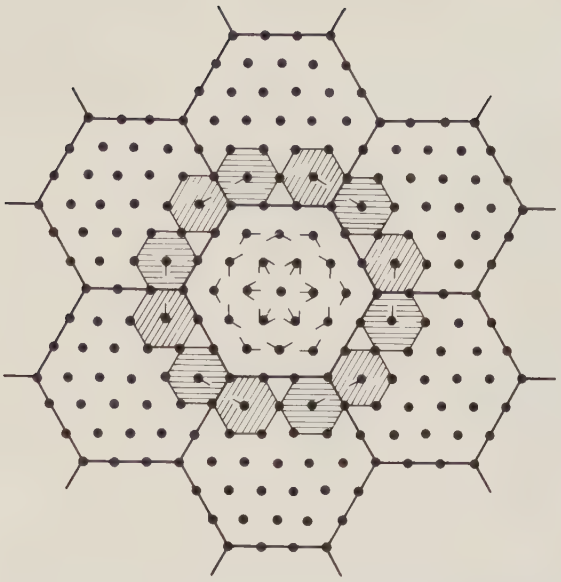

Fig. 5. Grouping of genics for cortical convergence. Each group creates a cortical hypercolumn. The paired convergence for the central group is explained in the text

where each group projects into its own hypercolumn of corts. The hexagons in Figure 5 indicate the partitioning for part of the genics. According to the literature only a few, maybe only one or two geniculate cells converge on to a cortical cell (Creutzfeldt et al., 1974). It was therefore decided to feed always two neighbouring genics into a cort which gives the latter a slightly elongated RF. During any given processing cycle the cort fires if both genics carry a signal which makes it orientation sensitive.

In Figure 5 the paired convergence for the center group of genics is symbolized by little extremeties which always point in the direction of the converging partner. It will be noticed that there are six different alignments of converging pairs, yielding the above mentioned angles of orientation sensitivity at the cortical level. All genics with extremeties converge on simple corts which in turn have inhibitory effect on complex corts. The latter are excited by genics with two or three extremeties. Since simple corts are of inhibitory nature, only the genics that are surrounded by the hatched belt provide excitatory information to the cortical column while the hatched belt itself demarcates the retinal area that exerts only inhibitory influence. The hatched fields themselves outline the size of the RF centers.

Apart from the excitatory geniculate input, each complex cort receives inhibitory input from those simple corts whose RFs are parallel and adjacent to its own. With only one inhibitory flank the cort becomes sensitive toward direction of stimulus movement, with flanks on both sides its orientation specificity is accentuated. All complex gates of particular orientation or direction sensitivity feed into separate hypercomplex gates. This makes the former sensitive to a particular line of orientation irrespective of its position within the RF of the whole column and sensitizes the latter even further toward direction of stimulus movement.

So far there are five layers of gates within each hypercolumn. A layer of simple corts with broad orientation sensitivity, two layers of complex corts with accurate orientation and precursory direction sensitivity, and two hypercomplex layers with advanced sensitivities of both types. The corts in all layers of the hypercolumns are more or less orientation sensitive and those of identical orientation are stacked on top of each other. This provides for vertical orientation columns which are frequently reported in the literature. Furthermore, as was pointed out already, the orientation of all corts are arranged tangentially around the centers of the hypercolumns which leads to the circular patches of gates in Figure 4. A straight line drawn across several hypercolumns will pass along corts whose orientation specificities shift continuously in the same direction, interrupted occasionally by reversals depending on the angle of the line. Similar results have been reported recently when penetrating electrodes horizontally through the striate cortex. They have been taken either as support for a columnar organization (Hubel and Wiesel, 1974) or as evidence for a retinocortical continuity (Albus, 1975). The two principles are commonly believed to be mutually exclusive (Towe, 1975), yet, the cortical organization of the present simulation model demonstrates that they can coexist. The cortical hypercolumns of this model subdivide the

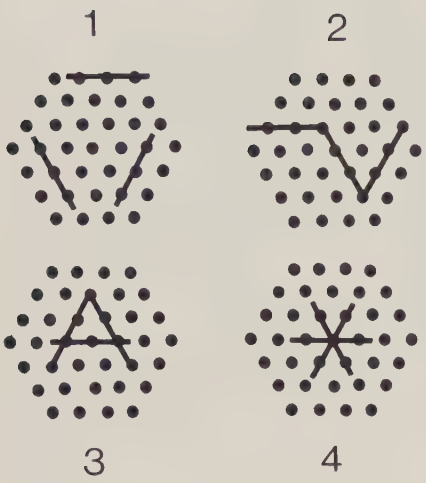

Fig. 6. Different contour constellations within a hypercolumnar receptive surface. In numerical order they cause increasing gang reactions while all four trigger identical responses in the corresponding contourgate

receptive matrix into distinctly separate areas which manifests itself in the fact that the retinal information of all areas is analyzed in parallel with regard to the relevant stimulus features. In spite of the columnar arrangement, the retinotopic representation in the cortex is continuous across hypercolumns. This is evident from the fact that the RFs of corts along any hypothetical line in Figure 4 shift continuously across the receptive matrix, even when crossing the boundaries between hypercolumns.

Conclusions

In its present form the simulation model captures some major aspects of the afferent *Y* system. Gangs with antagonistic center-surround RFs produce a topographical record of the activity centers (stimulation) on the receptive matrix by means of transient responses. They are attenuated by the geniculate gate network because of the inhibitory intergates. This provides an option for gating the retinal information such that it can pass during rest periods of the receptive matrix and gets blocked when the matrix moves. Due to the columnar organization of the cortex, the receptive matrix is subdivided into separate areas and the partitioned information is analyzed in parallel. This structure agrees with the columnar hypothesis without violating the reported retinocortical continuity. Within each hypercolumn line orientation and movement directions are extracted out of the stimulus material which are well documented processing features of the striate cortex.

The features the striate cortex extracts out of the stimulus material are very basic and tend to be of linear and moving nature. Since this information flows back to the superior colliculus which is a processing center for the peripheral retina, it probably reflects the extent of the form analysis that is performed on peripheral stimuli. One can demonstrate this fact to oneself by performing a quick test. Fixate a point in front of you and move a pencil through your peripheral visual field. You will notice that it is easy to perceive movement and its direction. It is also easy to tell the orientation of the pencil and when using objects of varying extent you can recognize their length and size. However, it is practically impossible to make out any finer aspects of the stimulus like color, texture, and details. Apart from the fact that identification of peripheral stimuli is poor, it is still better for linear forms like squares and triangles than for curved ones like circles (Collier, 1931; Munn and Geil, 1931). Although forms are poorly identified, their appearance is readily detected (Handel and Christ, 1969). When linear stimuli are projected into the peripheral retina they trigger the awarness that something has entered the visual field but the person is not able to tell what it is. That is exactly the kind of situation one would expect to preceed foveation.

In order to simulate that situation, contour detectors or contourgates are currently developed within each cortical hypercolumn. They respond to a set of contours irrespective of where in the hypercolumnar field they occur and in what constellation (see Fig. 6). To distinguish between the four contour arrangements another discriminative mechanism is needed. One such possible mechanism is given by the output of the corresponding gangs. The four different constellations excite the RFs of individual gangs in various degrees. It is interesting to note that the longest gang responses are caused by adjacent or overlapping contours which frequently form regular and symmetrical patterns. It should be possible to design networks of threshold gates that detect the joint occurrence of a response of a certain contourgate and long signals from several corresponding gangs. In case of detection of such a joint event, a foveation command could be issued to move the center of the receptive matrix to the relevant stimulus, the exact location of which can be derived from the triggering gangs. By proper integration of retinal and cortical information it should become possible to distinguish between regular and irregular patterns, thereby securing a mechanism for the selection of peripheral stimuli and the generation of motor commands for the foveation of the receptive matrix.

Within the broader context of visual perception such a simulation model would represent a first approximation of the neural processes involved in stimulus foveation which is a prerequisite for its correct identification in a normal viewing situation. Appar-

ently, the discriminative ability of the *Y* system is sufficient to distinguish interesting and meaningful stimuli from irrelevant ones. It is possible that this selection is performed in the superior colliculus and that it is based on the distiction between regular and irregular forms. While in this simulation model the receptive matrix would be focussed on that regular form that causes the strongest excitation, it appears to be certain that other factors like memory, context, motivation, etc. participate in the mammalian foveation decision.

References

Albus, K.: The spatial organization of the orientation domain in cat's area 17. Paper presented at the 7th. International Neurobiology Meeting, Göttingen, 1975

Cleland, B.G., Dubin, M.W., Levick, W.R.: Sustained and transient neurons in the cat's retina and lateral geniculate nucleus. J. Physiol. **217**, 473–496 (1971)

Collier, R.M.: An experimental study of form perception in indirect vision. J. Comp. Physiol. Psychol. **11**, 281–290 (1931)

Creutzfeldt, O.D., Kuhnt, U., Benevento, L.A.: An intercellular analysis of visual cortical neurons to moving stimuli: Responses in a co-operative neural network. Exp. Brain Res. **21**, 251–274 (1974)

Doty, R.W., Wilson, P.D., Bartlett, J.R.: Mesencephalic control of lateral geniculate nucleus in primates. I. Electrophysiology. Exp. Brain Res. **18**, 189–203 (1970)

Enroth-Cugell, C., Robson, J.G.: The contrast sensitivity of retinal ganglion cells of the cat. J. Physiol. **187**, 517–552 (1966)

Fuster, J.M., Uyeda, A.A.: Facilitation of tachistoscopic performance by stimulation of midbrain tegmental points in the monkey. Exp. Neurol. **6**, 384–406 (1962)

Gilbert, C.D., Kelly, J.P.: The projections of cells in different layers of the cat's visual cortex. J. Comp. Neurol. **163**, 81–106 (1975)

Handel, S., Christ, R.E.: Detection and identification of geometric form using peripheral and central viewing. Percept. Psychophys. **6**, 47–49 (1969)

Hubel, D.H., Wiesel, T.N.: Receptive fields, binocular interaction, and functional architecture in the cat's visual cortex. J. Physiol. **160**, 106–154 (1962)

Hubel, D.H., Wiesel, T.N.: Shape and arrangement of columns in the cat's striate cortex. J. Physiol. **165**, 559–568 (1963)

Hubel, D.H., Wiesel, T.N.: Receptive fields and functional architecture of monkey striate cortex. J. Physiol. **195**, 215–243 (1968)

Hubel, D.H., Wiesel, T.N.: Sequences of regularity and geometry of of orientation columns in the monkey striate cortex. J. Comp. Neurol. **158**, 267–294 (1974)

Ikeda, H., Wright, M.J.: Evidence for sustained and transient neurons of cat's visual cortex. Vis. Res. **14**, 133–136 (1974)

Mountcastle, V.B.: Modality and topographic properties of single neurons of cat's somatic sensory cortex. J. Neurophysiol. **20**, 408–434 (1975)

Munn, N.L., Geil, G.M.: A note on peripheral form discrimination. J. Gen. Psychol. **5**, 78 88 (1931)

Schiller, P.H., Stryker, M.: Single-unit recording and stimulation in superior colliculus of the alert rhesus monkey. J. Neurophysiol. **35**, 915–924 (1972)

Schneider, G.E.: Two visual systems. Science **163**, 895 902 (1969)

Schultze, M.: Zur Anatomie und Physiologie der Retina. Arch. mikr. Anat. **2**, 175–286 (1866)

Singer, W., Creutzfeldt, O.D.: Reciprocal lateral inhibition of on- and off-center neurones in the lateral geniculate body of the cat. Exp. Brain Res. **10**, 311–330 (1970)

Singer, W., Tretter, F., Cynader, M.: Organization of striate cortex: A correlation of receptive-field properties with afferent and efferent connections. J. Neurophysiol. **38**, 1080–1098 (1975)

Stone, J., Dreher, B.: Projections of *X*- and *Y*-cells of the cat's lateral geniculate nucleus to areas 17 and 18 of visual cortex. J. Neurophysiol. **36**, 551–567 (1973)

Stone, J., Holländer, H.: Optic nerve axon diameters measured in the cat retina: Some functional considerations. Exp. Brain Res. **13**, 498 503 (1971)

Szentágothai, J.: Neuronal and synaptic architecture of the lateral geniculate nucleus. In: Handbook of Sensory Physiology. Vol. VII/3. Jung, R. (Ed.): Central Visual Information B. Berlin-Heidelberg-New York: Springer 1973

Tolkmitt, F.J., Hammond, I.J.: Single cell recordings from the visual cortex of a computer. Psychol. Res. **38**, 65–80 (1975)

Towe, A.L.: Notes on the hypothesis of columnar organization in somatosensory cerebral cortex. Brain Behav. Evol. **11**, 16–47 (1975)

Trevarthen, C.B.: Two mechanisms of vision in primates. Psychol. Forsch. **31**, 299–337 (1968)

Wurtz, R.H., Mohler, C.W., Robinson, D.L.: Visualmotor integration in monkey superior colliculus. Paper presented at the 7th. International Neurobiology Meeting, Göttingen 1975

Received: September 10, 1976

Dr. Frank J. Tolkmitt
Center for Systems Neurosciences
University of Massachusetts
Amherst, MA 01003, USA

Biol. Cybernetics 25, 205–208 (1977)

Biological Cybernetics

The Signal-Flow Diagram of the Oculomotor Control System, — and its Transferability to the More Intricate Skeletomotor Control System

P. Lässig

Carl-Ludwig-Institute of Physiology, Karl-Marx-University Leipzig, GDR

Abstract. A signal-flow diagram of the oculomotor control system has been derived which is able to describe the three modes of its action 1) pursuit movements 2) voluntary saccadic movements and 3) the passive non-innervated state of extraocular muscles which exists during sleep. It has been taken into consideration that in the smooth pursuit system there is a neural integrator in order to bring back to zero the error between the position of the eye and an external constant reference point. [Evidence for integration in oculomotor pathways we have from experiments by Cohen and Komatsuzaki (1972) who used stimulation of the pontine reticular formation.] All this is achieved by a system of variable structure with three states. In skeletomotor systems likewise there are smooth compensatory movements and voluntary movements and a state without any innervation. Some neurological diseases can be interpreted as an impairment of switching at special spots of the signal-flow diagram or as a disconnection of signal-pathways, respectively. From this can be concluded that the signal-flow diagram derived for the rather lucid oculomotor control system should be able to describe the basic function of skeletomotor control systems, too.

1. Introduction

As for the system theoretical view of the environmental orientation of man three aspects are of importance: 1) an organism is coupled to the environment by receptors, 2) in spite of this coupling voluntary movements are possible, 3) muscles effecting movements can temporarily be in a passive state. Those three aspects are prominent in optical orientation, they are less clearly obvious than in the innervation of eye muscles when it comes to body or limb movements, respectively. Here they occur only in pathological cases, and also in gravity orientation. Confining our attention at first to optical orientation, where eye position is controlled in relation to an object it is possible to derive a control system characterized by three states. This control system is then successfully transferred to skeletomotor control systems. The three states correspond to the smooth tracking movements, the voluntary saccadic movements and the passive state of muscles, respectively.

2. Smooth Tracking and Voluntary Eye Movements

The eye tracking system stabilizes the picture of the moving target on the fovea. If the tracking error increases over and above a definite value, saccadic eye movements will appear. Figure 1 shows only the control loop for smooth tracking movements; the signal-flow diagram represents the state of the system for tracking eye movements, which we will define as a "state of smooth movement".

Since in a proportional control system the tracking error would increase permanently by the movement of a target with constant velocity it is necessary to assume the presence of an integrating element in the forward path of the eye tracking system. Crone and

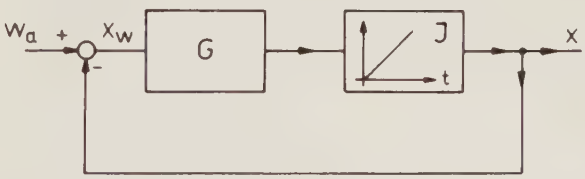

Fig. 1. Signal-flow diagram of the system for smooth tracking movements; "state of smooth movement": w_a external command variable; target angle; x controlled variable; eye angle; x_w tracking error; difference between target and eye angle; I integrating element; G transfer element, in which are especially concentrated the dead time; t time

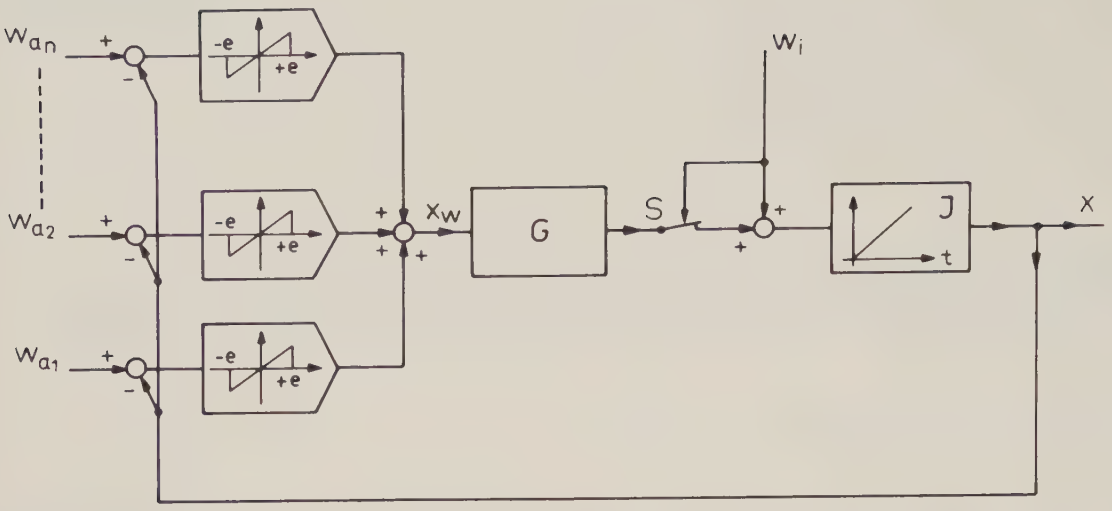

Fig. 2. Signal-flow diagram of the system for smooth tracking and voluntary saccadic movements; "state of smooth movement": $w_i = O$ (*S*—closed); "state of saccadic movement": $w_i \neq O$ (*S*—open); w_{an} potential external command variables; potential target angles; w_i internal command variable; desire to move; *S* switch in the loop for smooth tracking movements; *e* threshold for tracking error; x, x_w, *I*, *G*, *t*—see Figure 1

Verduyn Lunel (1968) experimenting on the closed loop and after-images showed that the tracking error in the case of a constant velocity of the command variable will be constant, this will also hold for the error in a control loop with an integrating element in the forward path. Kommerell and Klein (1971), also working with after-images, showed that the controlled variable will steadily increase with a constant command variable, if the loop is open. Cohen and Komatsuzaki (1972) when applying electrical stimulation to the paramedian zone of the pontine reticular formation in rhesus monkeys proved the existence of integration in oculomotor pathways.

To make possible a target change Lässig (1973) suggested a nonlinear static characteristic with threshold *e* (Fig. 2). This threshold would be a function of attention as shown by results of Weese Puckett and Steinman (1969) for tracking movements. Such a nonlinear static characteristic would be equivalent to the phenomenon known as tunnel vision in perception (Trevarthen, 1968). Potential targets in the environment are matched by the external command variables w_{an} of Figure 2. As soon as the aligned error x_w falls below threshold *e*, one of the command variables becomes effective. With the internal command variable w_i the position of the eye ball can be changed by a saccade, the minimal intersaccadic interval is to be found in the region of 0.2 s. It is assumed (Reinhardt and Zuber, 1971), that the time dependence of w_i is equivalent to time dependences of motoneurone discharge during one saccadic movement. In Figure 2 we disregard pulse-frequency modulation and antagonistic muscles, and therefore the voluntary pulse w_i is a pulse of constant amplitude and variable length. The sign will determine the direction of the eye movement whereas pulse duration will determine the angle of rotation of the eye ball.

Any movement from one target to another will require an opening of the closed loop for smooth tracking movements, otherwise an error signal would work against the voluntary saccade. The signal-flow diagram with the switch *S* in an "open" position (Fig. 2) shows the state of the system for tracking and voluntary movements, which we will define as a "state of saccadic movement". A fact pointing to the existence of such a switch is the visual suppression during saccadic movements (Duffy and Lombroso, 1968), this suppression is not complete and effects the perception of images. It was as yet not shown that the error signal is suppressed in the same way, but this is something we have to assume, in addition the error value might be suppressed by blinks. Haberich and Fischer (1958) investigated voluntary eye movements occurring along with head movements and found that a quick rotation of the eye ball normally took place during blinks. Moreover already infants aged two years showed that an average of 80 p.c. of all blinks is linked with voluntary eye and head movements.

If there is no target after a voluntary eye movement the new position is nevertheless maintained for a long time, compared to a minimal intersaccadic interval. This function will be described as a "holding function" and it will be assigned to the state of saccadic movement, because both ontogenetically and phylogenetically it is closer to a saccadic movement than to a smooth tracking movement.

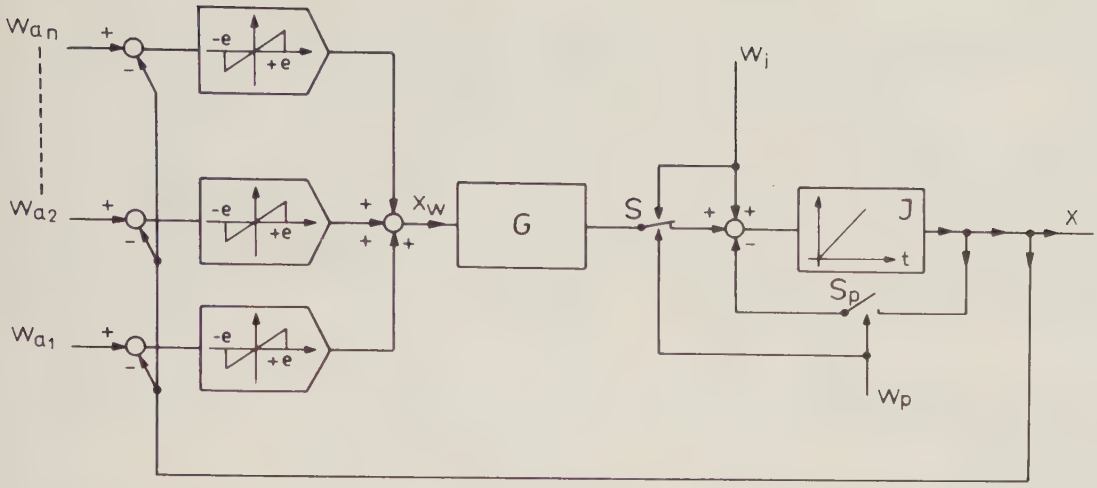

Fig. 3. Completed signal-flow diagram of the system for smooth tracking and voluntary saccadic movements including adjustability of the "state of passivity of muscles"; "state of smooth movement": $w_i = O$, $w_p = O$ (S—closed, S_p—open); "state of saccadic movement": $w_i \neq O$, $w_p = O$ (S—open, S_p—open); "state of passivity of muscles": $w_i = O$, $w_p \neq O$ (S—open, S_p—closed); w_p signal to switch on the "state of passivity of muscle"; S_p switch in the feedback path of the integrating element; x, x_w, I, G, t see Figure 1; w_{an}, w_i, S, e see Figure 2

A third state, which will be described as a "state of passivity of muscles" will have to be considered since eye muscles may also lack innervation which is observed during sleeping (Breinin, 1957). For this state we have to introduce a switch S_p in an additional feedback path and another command variable w_p (Fig. 3). When the switch S_p will be closed, we face a time-lag element instead of an integrating element and output x will be proportional to the error value x_w. In this case, so as to guarantee that the muscles are definitely passive the switch S must be open. The signal-flow diagram of Figure 3 represents—with switch S open and switch S_p closed—the state of passivity of muscles of the system for tracking and voluntary eye movements.

3. Movement of the Muscles of the Skeletomotor System

The control system model for eye movements as described above may be transferred on to the skeletomotor system, as discerning three states would help interpret movements of skeletal muscles among other things. In the latter system the movements typical of these states are disguised by effects of changing load conditions and a diversity of voluntary movements. Only in special cases do the states appear in a clearcut form: Saccadic movements may be seen where the upper threshold frequency by load does not smooth quick voluntary movements, something that applies to voluntary finger movements of people (Wachholder, 1928). In the same way as it holds for voluntary eye movements we find a complete inhibition of the antagonist of voluntary movements of the skeletal muscles. Wachholder demonstrates alternating innervation also for so-called "versteifte" (stiffened) movements, where agonist and antagonist are seemingly operating simultaneously.

A psychiatric symptom, the so-called "Haltungsverharren" (holding of a position) amounts to the equivalent of a stationary position of the eye ball after a voluntary eye movement. In this case positions of head or limbs for instance are kept up without fatigue, any intention to do so will not be necessary (Fernandes, 1937). Healthy persons don't show any such "Haltungsverharren" because following a voluntary innervation the muscles will automatically become passive, whereas in the case of "Haltungsverharren" this must be performed by an additional voluntary movement.

In pathological cases, tracking movements can be observed, too (Fernandes, 1937). Here patients feel an enforced urge to track with their hands the movements of the hand of the experimenter, only guided by their tactile receptors. This points to an integrator in the skeletomotor control system as the phenomenon "Haltungsverharren" does.

The third state, the "state of passivity of muscles" occurs in skeletal muscles during sleep (Jouvet, 1967) and, contrary to the eye muscles, while people relax (Ralston and Libet, 1953).

References

Breinin, G.M.: Electromyographic evidence for ocular muscle proprioception in man. A.M.A. Arch. Ophthalm. **57**, 176—180 (1957)

Cohen, B., Komatsuzaki, A.: Eye movements induced by stimulation of the pontine reticular formation: Evidence for integration in oculomotor pathways. Exp. Neurol. **36**, 101—117 (1972)

Crone, R. A., Verduyn Lunel, H. F. E.: Autokinesis and the perception of movement: The physiology of eccentric fixation. Vision Res. **9**, 89—101 (1969)

Duffy, F. H., Lombroso, C. T.: Electrophysiologic evidence for visual suppression prior to the onset of a voluntary saccadic eye movement. Nature (Lond.) **218**, 1074—1075 (1968)

Fernandes, B.: Klinische Untersuchungen über motorische Erscheinungen bei Psychosen und organischen Hirnkrankheiten. Abhandlungen aus der Neurologie, Psychiatrie, Psychologie. Berlin: Karger 1937

Haberich, F. J., Fischer, M. H.: Die Bedeutung des Lidschlags für das Sehen beim Umherblicken. Pflüg. Arch. ges. Physiol. **267**, 626—635 (1958)

Jouvet, M.: Neurophysiology of the states of sleep. Physiol. Rev. **47**, 117—177 (1967)

Kommerell, G., Klein, U.: Über die visuelle Regelung der Okulomotorik: Die optomotorische Wirkung excentrischer Nachbilder. Vision Res. **11**, 905—920 (1971)

Lässig, P.: Das Ruck-Gleit-Peilprinzip der Orientierung am Beispiel des Einsatzes der Augenmotorik bei Augenfolge- und Blickbewegungen. Nova Acta Leopoldina **211**, 313—327 (1973)

Ralston, H. J., Libet, B.: The question of tonus in skeletal muscle. Amer. J. phys. Med. **32**, 85—92 (1953)

Reinhart, R. J., Zuber, B. L.: Parameters of the control signals for saccadic eye movement: Electrical stimulation and modelling. Exp. Neur. **30**, 148—161 (1971)

Trevarthen, C. B.: Two mechanisms of vision in primates. Psychol. Forsch. **31**, 299—337 (1968)

Wachholder, K.: Willkürliche Haltung und Bewegung, insbesondere im Lichte elektrophysiologischer Untersuchungen. Ergebn. Physiol. **26**, 568—775 (1928)

Weese Puckett, J. De, Steinman, R. M.: Tracking eye movements with and without saccadic correction. Vision Res. **9**, 695–703 (1969)

Received: September 23, 1976

Dipl.-Ing. P. Lässig
Carl-Ludwig-Institute of Physiology
Karl-Marx-University Leipzig
Liebigstr. 27
GDR 701 Leipzig

Biol. Cybernetics 25, 209–226 (1977)

Biological Cybernetics

Dependency as a Measure to Estimate the Order and the Values of Markov Processes

H. Nakahama, M. Yamamoto, N. Ishii, H. Fujii, and K. Aya

Division of Neurophysiology, Institute of Brain Diseases, Tohoku University School of Medicine, Sendai, Department of Information Engineering, Nagoya Institute of Technology, Nagoya, and Division of Human Engineering, Shibaura Institute of Technology, Oomiya, Saitama, Japan

Abstract. To evaluate the order and the values of Markov properties of the time series of events, we have proposed a statistical measure "dependency": $D_m=(H_0-H_m)/H_0$, where H_0 and H_m are Shannon's entropy and the m-th order conditional entropy, respectively. It is indicated that $\tilde{D}_m=\sum_{\nu=1}^{m}(\hat{D}_\nu-\bar{D}_\nu^{\mathrm{sh}})$ is a better point estimator of D_m, giving a total value of the m-th order Markov process. Here $\hat{D}_m$ and $\bar{D}_m^{\mathrm{sh}}$ are the estimate of D_m and the arithmetic mean of $\hat{D}_m^{\mathrm{sh}}$ when the m-th order shuffling is made many times for a given observed series, respectively. The value $\hat{D}_m-\bar{D}_m^{\mathrm{sh}}=d_m$ represents Markov value of the order m. Under the assumption that the series has continuous variables and the normal distribution, simplified dependency is defined by $\hat{\mathscr{D}}_m=\frac{1}{2}\{\log_2|S_m|-\log_2|S_{m+1}|\}$, where $|S_m|$ is the determinant of serial correlation coefficients. It is shown that $\hat{\mathscr{D}}_m$ is practically useful for the estimation of the order and the values of Markov processes with small sample size. It is also indicated that $\mathscr{D}_m$ analysis is basically equivalent to the least mean-square analysis of autoregressive models.

1. Introduction

Since the papers of Nakahama et al. (Nakahama, 1966; Nakahama and Nishioka, 1966; Nakahama et al., 1966), we have continued the investigation of dependency which represents the order and the values of Markov properties of the time series of events. As spike trains are regarded as stochastic point processes, dependency is applicable for these processes. In an earlier paper of this series (Nakahama et al., 1971), a report was made on maintained spike trains recorded from single neurons of the ventrobasal complex (VB), the lateral geniculate nucleus (LGN), the mesencephalic reticular formation (MRF) and the red nucleus (RN). The VB and LGN neurons are known to process input information precisely and promptly: the function is phasic. This was related to the fact that the maintained activity of these neuron groups had no or weak Markov properties: the state of the neuron depends little on its past activity. If time dependence of the maintained spike activity in these groups were of great extent, it might be inappropriate for processing input information. The MRF and the RN neurons are known to regulate the general state of the brain and to associate with the posture, respectively: the function of these neurons is tonic. This may have a bearing on the fact that the maintained activity of these neuron groups had higher order and values of Markov properties: the state of the neuron depends highly on its past activity. Then these suppositions were confirmed with the use of a statistic composed of the determinants of the serial correlation coefficients, in which the shuffling method was introduced (Nakahama et al., 1972). This statistic was shown, with semi-Markov processes generated by simulation techniques, to be a useful measure with small sample size (Nakahama et al., 1974). Thereafter this statistic was improved for the point estimator of dependency (Nakahama et al., 1975a, 1975b).

The purpose of preceding and present studies is to determine the order and the values of Markov properties of neuronal spike trains with the use of dependency. However the relationship between the estimate of dependency and dependency in the population has not necessarily been clear in our previous papers described above. Moreover the nature of shuffling has still been a matter of speculation. The present study was designed to secure the information of these. Here the methods of analysis and obtained results are described, together with some remarks about the state space and possible significance of dependency. It is to be noted that definition, designation and notations of this paper varies considerably from those of our previous papers.

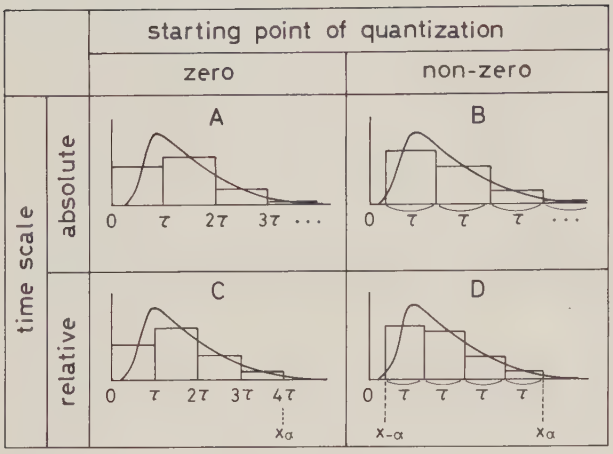

Fig. 1A—D. Scheme to illustrate the quantization of time intervals x_t by equal bin width τ. **A** and **B** show time scales chosen by absolute time; and **C** and **D**, by relative time according to the distribution of x_t. **A** and **C** indicate starting points of quantization at time *zero*; and **B** and **D**, at *non-zero* time. When $n_s=4$, $\tau=x_\alpha/4$ **C** and $\tau=(x_\alpha-x_{-\alpha})/4$ **D**

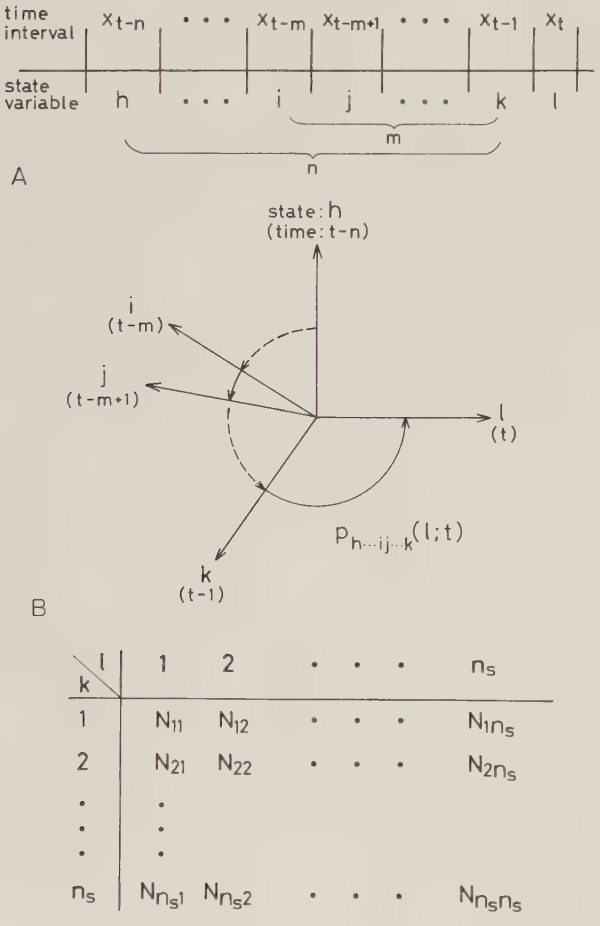

Fig. 2A—C. Diagram illustrating the relation between time interval sequence $\{x_t\}$ and state variables $h...ij...kl$ **A**, transition probability at time t **B**, and joint interval histogram in the set of states (k, l) when $m=1$ **C**

2. Methods

Fourteen interval sequences with various probability distributions generated by computer were employed (Fig. 12): 2 normal processes (Appendix 1); 3 gamma (Appendix 2); 2 Wold's Markov (Appendix 3); and 7 semi-Markov (Appendix 4).

It is problem how to determine total number of states n_s and bin width τ for the calculation of dependency. Let $\tau=(x_{\max}-x_{\min})/n_s$, where $x_{\max}$ and $x_{\min}$ are the maximum and minimum value of consecutive intervals $\{x_t\}$ $(t=1, 2, ..., N)$, respectively. Then there is a possibility that inadequately long bin width is determined, when extremely long and/or short intervals exist in an interval sequence. Therefore we set the following: $\tau=(x'_{\max}-x'_{\min})/n_s$, $x'_{\max}=\mu+3\sigma$ and $x'_{\min}=\mu-3\sigma$, where μ and σ are the mean and standard deviation of $\{x_t\}$, respectively. When $x_{\max}<x'_{\max}$, the value of a cumulative 99,9 % point is newly set by $x'_{\max}$; and when $x_{\min}>x'_{\min}$, the value of a cumulative 0.1 % point by $x'_{\min}$. Thereafter in the case of $x_t>x'_{\max}$, x_t is regarded as belonging to the highest n_s-th state; and of $x_t<x'_{\min}$, x_t as the lowest 1st state. For the calculation of simplified dependency, we set the following: $x_t=x'_{\max}$ when $x_t>x'_{\max}$; and $x_t=x'_{\min}$, when $x_t<x'_{\min}$.

Uniform pseudorandom numbers were generated with the multiplicative congruential method (Naylor et al., 1967). That is,

$$n_{i+1}\equiv a\cdot n_i \pmod P \quad (i=0, 1, 2,...)$$

$$r_i=n_i/P,$$

where a is a constant multiplier and "mod P" means that $a\cdot n_i$ is divisible by multiples of integer P with remainder n_{i+1}. Then $\{n_i\}$ is a sequence of *non-negative* integers, and r_i is a uniform pseudorandom number defined by the unit interval (0, 1). Such a generation of pseudorandom numbers causes the overflow of register and needs a full word length. Accordingly the values a and P are necessary to be chosen and determined according to the computer employed. Here we generated the pseudorandom numbers by setting an initial starting value $n_0=6351339885$, $a=5^{11}$ and $P=2^{30}$. Thereafter the following statistical tests of the pseudorandom numbers were made: the frequency, serial, lagged product, run and gap tests. These are based on the chi-square test for goodness of fit. The randomness of a sequence of pseudorandom numbers which we generated is acceptable at a 1 % level of significance, when sample size $N=250$, 500, 1000, 2000, 4000, 8000, 16000, 32000.

For the generation of interval sequences and the computations we used HITAC 8800/8700 system (one word, 32 bits) consisted of large scale computers.

3. Dependency for Discrete Variables

3.1 Choice of Random Variables

For the analysis of stochastic point process we could adopt either the times between events or the number of events in an arbitrary unit interval as random variables. Since these two aspects of process are considered to be fundamentally equivalent (Cox and Lewis, 1966), we conveniently deal with the times between events in this paper. In the case of regarding the time intervals as variate of state space, there are two standpoints in which variate is discrete or continuous.

Firstly we treat with discrete state space. We could constitute state space in different ways for the interval sequence. It is usually employed to quantize the time intervals by equal bin width. In this case, as will be seen in Figure 1, starting point of quantization could be

chosen by either *zero* or *non-zero;* and time scale, by either absolute or relative time. On the other hand, there is a method to quantize the time intervals by unequal bin widths. For example, after distributing observed intervals equally (Nakahama et al., 1974) or normally (Nakahama et al., 1975a) the transformed intervals is quantized by equal bin width. In this paper we take the following position (Fig. 1D).

Let

$$\{i\},\ i=1,2,3,\ldots,n_s$$

be the finite state space for time intervals x_t quantized by equal bin width. Here n_s represents a total number of states, and bin width τ is determined by the following equation:

$$\tau=\frac{x_\alpha-x_{-\alpha}}{n_s}, \tag{1}$$

where $x_{-\alpha}$ and x_α are the lower and upper α point of the distribution of x_t, respectively. We assume that x_t of $x_t \leqq x_{-\alpha}$ and of $x_t > x_\alpha$ corresponds to state 1 and n_s, respectively (see Methods). Then

$$(i-1)\tau < x_t - x_{-\alpha} \leqq i\tau, \tag{2}$$

where x_t corresponds to state i. In this definition of state space, x_t is quantized by relative time scale in the distribution.

3.2 Condition of the m-th Order Markov Process

In the population, let

$$p_{h\ldots ij\ldots k}(l;t) \tag{3}$$

denote the transition probability of state l at time t, given state k at time $t-1$ ... and state j at time $t-m+1$ and state i at time $t-m$ ... and state h at time $t-n$, where the value of $h,\ldots,i,j,\ldots,k,\ l$ is one of $1,2,\ldots,n_s$, respectively, and $t=n+1, n+2, n+3, \ldots$ (Fig. 2A, B). In the case of a stationary Markov process Equation (3) becomes independent of t, and is given by

$$p_{h\ldots ij\ldots k}(l). \tag{4}$$

Then the necessary and sufficient condition of the m-th order Markov process in the state space given by Equation (2) is as follows:

$$\underbrace{p_{h\ldots ij\ldots k}}_{n}(l)=\underbrace{p_{ij\ldots k}}_{m}(l) \neq \underbrace{p_{j\ldots k}}_{m-1}(l). \tag{5}$$

Equality in Equation (5) holds for all $n(n \geqq m+1)$ and for all combinations of states $(h,\ldots,i,j,\ldots,k,l)$. Inequality in Equation (5) holds for at least one combination of states $(i,j,\ldots,k,l)$.

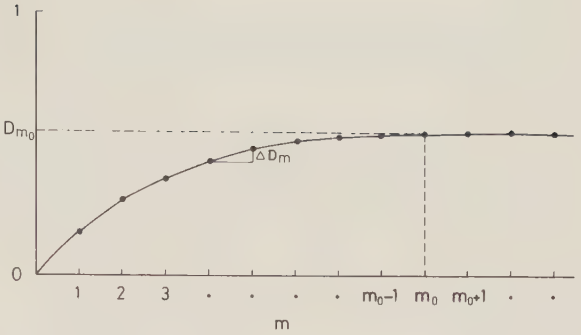

Fig. 3. Schematic representation of the relation between m and D_m. When we let m_0 denote m where $\Delta D_m=0$, m_0 gives the order of Markov process. Then D_{m_0} represents the total value of Markov property

3.3 Definition of Dependency in the Population

The transition probability matrix is employed to represent the Markov process in a given state space. It is one of the main points of time series analyses to estimate both the order of Markov process and the transition probability matrix from the observed series of events. From this aspect we have proposed dependency as one of statistical measures to represent both the order and the pattern of the transition probability matrix.

The m-th order dependency D_m in the population is defined by

$$D_m=\frac{H_0-H_m}{H_0}, \tag{6}$$

where H_0 and H_m are Shannon's (1949) entropy and conditional entropy with the m-th order, respectively. That is,

$$H_0=-\sum_l p(l)\log_2 p(l), \tag{7}$$

and

$$H_m=-\sum_{ij\ldots kl}\ldots\sum p(i,j,\ldots,k,l)\log_2 p_{ij\ldots k}(l), \tag{8}$$

where $p(l)$ and $p(i,j,\ldots,k,l)$ are a probability of state l and a joint probability of states $(i,j,\ldots,k,l)$, respectively. When we describe the necessary and sufficient condition of the m-th order Markov process by using H_0 and H_m, the following expression holds:

$$H_0 \geqq H_1 \geqq H_2 \geqq \ldots \geqq H_{m-1} > H_m = H_{m-1} = H_{m+2} = \ldots. \tag{9}$$

Accordingly the following expression holds (Nakahama et al., 1972):

$$D_1 \leqq D_2 \leqq \ldots \leqq D_{m-1} < D_m = D_{m+1} = D_{m+2} = \ldots. \tag{10}$$

The order of Markov process is determined by using Equation (10). As indicated in Figure 3, D_m is the

monotonically increasing function of m. Let ΔD_m denote the increment of D_m concerning m:

$$\Delta D_m = D_m - D_{m-1}, \tag{11}$$

where $D_0 = 0$. When $\Delta D_m = 0$ for all $m \geqq m_0 + 1$, the least value of m_0 gives the order of Markov process. Here we designate the value ΔD_m as Markov value of the order m.

The range of D_m covers the values between 0 and 1 for all m (Nakahama et al., 1972):

$$0 \leqq D_m \leqq 1.$$

In the case of independent process, the order of Markov process is 0, and the rows of the transition probability matrix have the same distribution.

Then

$$D_m = 0 \ (m = 1, 2, \ldots).$$

When a stochastic process has Markov properties, the rows of the transition probability matrix have the different distributions. In the limit case, the transition probability of a special state is 1 for each row, and that of other states is 0. Here the process is completely dependent. In this case,

$$D_m = 1 \ (m = 1, 2, \ldots).$$

Thus D_m is a statistical measure which represents degrees of dependence of Markov process. Moreover D_m is a generalized statistical measure which represents pattern of nonlinear dependence, and is different from correlation coefficient which is based on linear hypothesis.

3.4 Statistical Inference on the Order of Markov Process

In the population, the condition of the m-th order Markov process is given by Equation (11). Here we describe how to infer the order of Markov process from stationary sample sequence of finite size N with the use of an estimator of D_m.

We define the following vector series for $m+1$ consecutive intervals drawn from the observed interval sequence $\{x_t\}$, $t = 1, 2, \ldots, N$:

$$\mathfrak{X}_{t,m} = \{x_{t-m}, x_{t-m+1}, \ldots, x_{t-1}, x_t\},$$
$$t = m+1, m+2, \ldots, N. \tag{12}$$

Let $N_{ij\ldots k}$ be joint frequencies in the set of states $(i, j, \ldots, k)$ among $\mathfrak{X}_{t,m}$, $t = m+1, m+2, \ldots, N$, and let $N_{ij\ldots kl}$ be joint frequencies in the set of states $(i, j, \ldots, k, l)$ (Fig. 2C). Then the estimates of the m-th order joint probability and conditional probability are given by

$$\hat{p}(i, j, \ldots, k, l) = \frac{N_{ij\ldots kl}}{N-m}, \tag{13}$$

and

$$\hat{p}_{ij\ldots k}(l) = \frac{N_{ij\ldots kl}}{N_{ij\ldots k}}, \tag{14}$$

respectively. Accordingly the estimate of H_m is given by

$$\hat{H}_m = -\sum_{ij\ldots}^{n_s} \cdots \sum_{kl=1}^{n_s} \frac{N_{ij\ldots kl}}{N-m} \log_2 \frac{N_{ij\ldots kl}}{N_{ij\ldots k}}. \tag{15}$$

The estimate of H_0 is as follows:

$$\hat{H}_0 = -\sum_{l-1}^{n_s} \frac{N_l}{N-m} \log_2 \frac{N_l}{N-m}, \tag{16}$$

where $N_l = \sum_{ij\ldots}^{n_s} \cdots \sum_{k=1}^{n_s} N_{ij\ldots kl}$.

From Equations (15) and (16) the estimate of D_m is given by

$$\hat{D}_m = \frac{\hat{H}_0 - \hat{H}_m}{\hat{H}_0}. \tag{17}$$

We consider the problem of testing the hypothesis for the estimate of the order of Markov process with $\hat{D}_m$, under the null hypothesis:

$$\Delta D_m = D_m - D_{m-1} = 0; \tag{18}$$

and under the alternative:

$$\Delta D_m = D_m - D_{m-1} > 0. \tag{19}$$

In order to test the hypothesis for the observed value $\Delta \hat{D}_m$ it is necessary to obtain the sampling distribution of $\Delta \hat{D}_m$ when the null hypothesis is true, where

$$\Delta \hat{D}_m = \hat{D}_m - \hat{D}_{m-1}. \tag{20}$$

However so far it seems to be difficult to derive the distribution analytically.

Here we consider getting the sampling distribution of $\Delta \hat{D}_m$ empirically. To do this it is necessary to compute $\Delta \hat{D}_m$ from sample series drawn from the population in which the null hypothesis of Equation (18) is true. In such a population the order of Markov properties is equal to or less than $m-1$; and the m-th order transition probability is equal to the $(m-1)$th order one:

$$p_{ij\ldots k}(l) = p_{j\ldots k}(l) \tag{21}$$

for the set of all states $(i, j, \ldots, k, l)$.

Here we introduce one of the shuffling methods in order to obtain the distribution of $\Delta \hat{D}_m$. First we observe sample series drawn from the assumed population of the m-th order Markov process. When sample size of the observed original series is sufficiently large, the estimate of the $(m-1)$th order transition probability is approximately equal to the value in the population:

$$\hat{p}_{j\ldots k}(l) \approx p_{j\ldots k}(l). \tag{22}$$

Therefore we could assume that the value $p_{j\ldots k}(l)$ is known. Then we interchange the first component x_{t-m} in the vector series $\mathfrak{X}_{t,m}$ given by Equation (12) with term x^{sh}_{t-m} drawn randomly from the original series $\{x_t\}$. We define the following vector series:

$$\mathfrak{Y}_{t,m}=\{x^{\mathrm{sh}}_{t-m}, x_{t-m+1}, \ldots, x_{t-1}, x_t\},$$
$$t=m+1, m+2, \ldots, N. \tag{23}$$

Here the distribution of $\{x^{\mathrm{sh}}_{t-m}\}$ corresponds to that of $\{x_t\}$. We designate this operation as the m-th order shuffling. The estimates of the m-th and the $(m-1)$th order transition probability computed from $\mathfrak{Y}_{t,m}$ are given by

$$\hat{p}_{i^{\mathrm{sh}}j\ldots k}(l) \quad \text{and} \quad \hat{p}_{j\ldots k}(l),$$

respectively. This expression indicates that only the estimate of the m-th order transition probability in the original vector series is varied by the m-th order shuffling. From Equation (22) x^{sh}_{t-m} and $(x_{t-m+1}, \ldots, x_{t-1}, x_t)$ is independent of each other. Therefore under the assumption of Equation (22).

$$E(\hat{p}_{i^{\mathrm{sh}}j\ldots k}(l)) \approx p_{j\ldots k}(l). \tag{24}$$

Equation (24) indicates that generated vector series with this shuffling method is sample vector series drawn from the population in which Equation (21) is satisfied. Accordingly it is enough to obtain empirical distribution of

$$\Delta\hat{D}^{\mathrm{sh}}_m=\hat{D}^{\mathrm{sh}}_m-D_{m-1}, \tag{25}$$

in order to get the distribution of $\Delta\hat{D}_m$, where $\hat{D}^{\mathrm{sh}}_m$ and D_{m-1} are computed from $\hat{p}_{i^{\mathrm{sh}}j\ldots k}(l)$ and $p_{j\ldots k}(l)$, respectively.

We consider how to determine the critical value of $\Delta\hat{D}_m$ at a given level of significance in order to test the null hypothesis as shown in Equation (18). To do this 14 time series models were employed (Table 1; Appendices 1—4), and the shuffling was made many times with generated pseudorandom numbers for each time series.

The empirical distribution of $\Delta\hat{D}^{\mathrm{sh}}_m$ of our models, where the shuffling was made 100 times for each model, resembled normal in the case of $n_s=5$ and 10 (Fig. 4). Accordingly we could obtain the critical value of $\Delta\hat{D}^{\mathrm{sh}}_m$, ΔD^{α}_m, for a given level of significance α with the use of the arithmetic mean of $\Delta\hat{D}^{\mathrm{sh}}_m$, $\Delta\bar{D}^{\mathrm{sh}}_m$, and of the standard deviation $SD(\Delta\hat{D}^{\mathrm{sh}}_m)$ calculated in value by the shuffling of a smaller number of times. That is,

$$\Delta D^{\alpha}_m=SD(\Delta\hat{D}^{\mathrm{sh}}_m)\cdot C_{\alpha}+\Delta\bar{D}^{\mathrm{sh}}_m, \tag{26}$$

where C_{α} is the upper α point of the unit normal distribution.

The empirical distribution of $\Delta\hat{D}^{\mathrm{sh}}_m$ was relatively distorted from the normal distribution in the case of $n_s=2$ and 3 (Fig. 4). In this case we could regard the largest value of $\Delta\hat{D}^{\mathrm{sh}}_m$ as a critical value at a level of significance $\alpha=1/n$, when the shuffling was made n times (Appendix 5). From Tables 1 and 2 it is seen that ΔD^{α}_m is practically useful for the estimation of the order of Markov process.

Table 1. Parameters for 14 interval sequences and their expected order of Markov properties

Model Name	μ	σ	ϱ_1	ϱ_2	ϱ_3	expected order
NORML 113	80.2	20.0	0.465	0.002	−0.000	≧1
NORML 013	80.2	19.8	0.007	−0.011	0.006	0
GAMMA 115	65.3	19.6	0.444	−0.009	−0.016	≧1
GAMMA 015	65.5	19.9	−0.009	0.011	0.004	0
GAMMA 132	37.0	21.0	0.317	−0.003	−0.019	≧1
WOLDS 101	74.6	64.6	−0.158	0.030	0.002	1
WOLDS 001	76.3	64.6	−0.013	−0.009	−0.002	0
SEMI 1133	104.9	20.5	0.364	0.306	0.234	≧1
SEMI 1213	109.4	19.3	0.343	0.141	0.063	≧1
SEMI 1353	119.1	24.7	0.384	0.156	0.072	1
SEMI 1363	110.1	19.5	−0.522	0.312	−0.174	≧1
SEMI 1116	107.0	20.3	0.326	0.252	0.173	≧1
SEMI 2133	102.9	20.8	0.212	0.318	0.173	≧2
SEMI 2026	126.5	33.1	0.162	0.421	0.136	≧2

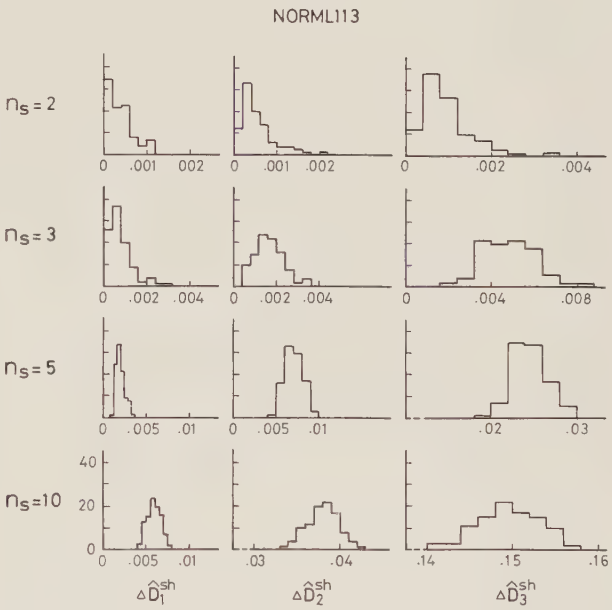

Fig. 4. An example showing the empirical distributions of $\Delta\hat{D}^{\mathrm{sh}}_m$. Since shuffling was made 100 times, the total number of values of $\Delta\hat{D}^{\mathrm{sh}}_1$, $\Delta\hat{D}^{\mathrm{sh}}_2$ and $\Delta\hat{D}^{\mathrm{sh}}_3$ was 100, respectively. Ordinates, frequency. $N=4000$

3.5 Point Estimation of D_m from the Sample Sequence

$\hat{D}_m$ has a distribution in a given sample size N. In the case of samples of small size, the bias of $\hat{D}_m$ is large from the true value D_m. If sample size is sufficiently large, the bias becomes negligibly small. However in the experi-

Table 2. Estimated order of Markov properties with $\Delta\hat{D}_m(n_s=2,3,5;\ m=1\text{–}3)$ and $\Delta\hat{\mathscr{D}}_m$ (continuous; $m=1\text{–}10$)

Model Name	estimated order			
	$n_s=2$	$n_s=3$	$n_s=5$	continuous
NORML 113	2	2	2	6
NORML 013	0	0	0	0
GAMMA 115	2	2	2	6
GAMMA 015	0	0	0	0
GAMMA 132	1	2	2	2
WOLDS 101	1	1	1	1
WOLDS 001	0	0	0	0
SEMI 1133	$\geqq 3$	$\geqq 3$	2	4
SEMI 1213	1	1	1	1
SEMI 1353	2	1	1	1
SEMI 1363	2	2	1	2
SEMI 1116	$\geqq 3$	$\geqq 3$	2	4
SEMI 2133	$\geqq 3$	$\geqq 3$	2	5
SEMI 2026	2	2	2	2

In the case of $n_s=2, 3$, ΔD_m^{α} = maximum value of $\Delta\hat{D}_m^{\mathrm{sh}}$; and shuffling was made 100 times. When $n_s=5$, Equation (26) was employed, where $\alpha=0.01$; shuffling, 10 times. In the case of $\Delta\hat{\mathscr{D}}_m$, $\alpha=0.01$. $N=4000$

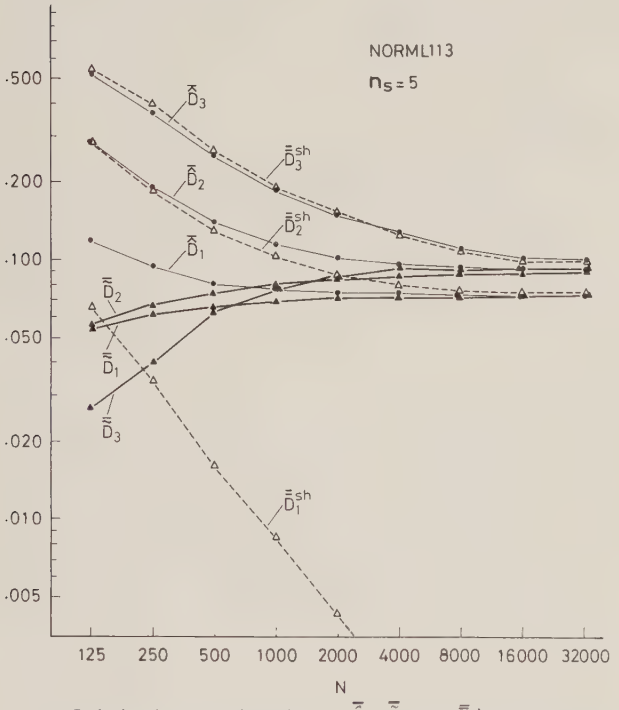

Fig. 5. Relation between the values of $\bar{\tilde{D}}_m$, $\bar{\tilde{D}}_m$ and $\bar{\tilde{D}}_m^{\mathrm{sh}}$ (ordinate) and sample size (abscissa), respectively. $\bar{\tilde{D}}_m$ and $\bar{\tilde{D}}_m^{\mathrm{sh}}$ are monotonically decreasing functions of N; and $\bar{\tilde{D}}_m$, monotonically increasing function.

ments of neurophysiology, we are often confronted with difficulties to get samples of sufficiently large size satisfied with the stationarity conditions. It is highly desirable to estimate the value D_m of spike trains with samples of relatively small size. It is from this aspect that we have proposed a statistic to get better point estimate of D_m, whose bias is relatively small, by utilizing $\hat{D}_m^{\mathrm{sh}}$.

Let $\bar{D}_m^{\mathrm{sh}}$ be the arithmetic mean of $\hat{D}_m^{\mathrm{sh}}$ when the m-th order shuffling was made n times for a given observed series. Then we could define the following measure as an estimator of D_m;

$$\tilde{D}_m = \sum_{\nu=1}^{m} d_\nu, \tag{27}$$

where

$$d_\nu = \hat{D}_\nu - \bar{D}_\nu^{\mathrm{sh}}. \tag{28}$$

From the properties of the shuffling procedure

$$\bar{D}_m^{\mathrm{sh}} \to D_{m-1} \quad (N\to\infty, \text{ in prob}).$$

Then

$$d_m \to \Delta D_m = D_m - D_{m-1} \quad (N\to\infty, \text{ in prob}). \tag{29}$$

Accordingly

$$\tilde{D}_m \to D_m \quad (N\to\infty, \text{ in prob}).$$

That is, $\tilde{D}_m$ converges in probability to D_m. Here Markov value of the order m, ΔD_m, is estimated by d_m.

Figure 5 indicates that $\tilde{D}_m$ converges more rapidly than $\hat{D}_m$. The bias of $\tilde{D}_m$ is relatively small. For example (Fig. 5),

$$\frac{|\bar{\tilde{D}}_1(N=250)-D_1|}{D_1} = \frac{|0.0957-0.0726|}{0.0726} = 0.32$$

and

$$\frac{|\bar{\tilde{D}}_1(N=250)-D_1|}{D_1} = \frac{|0.0617-0.0726|}{0.0726} = 0.15,$$

where the value $\tilde{D}_1(N=8000)$ is used for the true value D_1. That is, the bias of $\tilde{D}(N=250)$ from D_1 is 15%, while that of $\hat{D}_1(N=250)$ from D_1 is 32%. Similar results were obtained on all other models (Table 3).

Here it will be explained that the bias of $\tilde{D}_m$ is smaller than that of $\hat{D}_m$. As will be seen in Figure 6, when $N\to\infty$

$$\bar{\tilde{D}}_m \downarrow D_m \tag{30}$$

and

$$\bar{\tilde{D}}_m^{\mathrm{sh}} \downarrow D_{m-1}, \tag{31}$$

where $\bar{\tilde{D}}_m^{\mathrm{sh}}$ is the arithmetic mean of $\bar{D}_m^{\mathrm{sh}}$ for subsequences subdivided from the original series, and $\downarrow$ indicates monotonical decrease, Equations (30) and (31) are analytically proved (Appendix 6). From Equations (27) and (28)

$$\bar{\tilde{D}}_m \uparrow D_m, \tag{32}$$

where $\uparrow$ indicates monotonical increase (Fig. 6). Then if $D_m \ll 1/2$,

$$|\bar{\tilde{D}}_m - D_m| < |\bar{\hat{D}}_m - D_m| :$$

the bias of $\tilde{D}_m$ is smaller than that of $\hat{D}_m$ (Fig. 6). This indicates that $\tilde{D}_m$ is better than $\hat{D}_m$ as a point estimator of D_m. However as n_s and/or m increase the larger sample size is needed for the use of $\tilde{D}_m$.

4. Dependency for Continuous Variables

4.1 Definition of Dependency for Continuous Variables

The numerator of D_m given by Equation (6) represents mutual information, which increases monotonically and converges to mutual information in continuous space when $n_s \to \infty$ (Fig. 7). On the other hand the denominator of Equation (6), H_0, diverges in value as $n_s \to \infty$ (Fano, 1961). Accordingly we define mutual information as dependency for continuous variables:

$$D'_m = H_0 - H_m \qquad (n_s \to \infty). \tag{33}$$

To estimate D'_m it needs large sample size. Then we introduce a parametric method where the normal distribution is assumed for the time series.

4.2 Definition of Simplified Dependency

We shall now be concerned with dependency of normal process. In the case of the m-dimensional normal distribution, the joint entropy for continuous random variable is as follows:

$$Z_m = \log_2 (2\pi e)^{\frac{m}{2}} |a_{ij}^m|^{\frac{1}{2}}, \tag{34}$$

where $|a_{ij}^m|$ is the determinant of the covariance matrix (a_{ij}^m) (Shannon and Weaver, 1949). That is,

$$|a_{ij}^m| = \sigma^{2m} |S_m| ,$$

where

$$|S_m| = \begin{vmatrix} 1 & \varrho_1 & \cdots & & \varrho_{m-1} \\ \varrho_1 & 1 & \varrho_1 & \cdots & \varrho_{m-2} \\ \vdots & \varrho_1 & & & \vdots \\ & \vdots & & & \varrho_1 \\ \varrho_{m-1} & \varrho_{m-2} & \cdots & \varrho_1 & 1 \end{vmatrix}, \tag{35}$$

and ϱ_i is the i-th order serial correlation coefficient. Then dependency for continuous variables, i.e. mutual information, is given by the following equation:

$$\begin{aligned} D'_m &= H_0 - H_m \qquad (n_s \to \infty) \\ &= Z_1 + Z_m - Z_{m+1} , \end{aligned} \tag{36}$$

where Z_m is joint entropy (Nakahama et al., 1972).

When we replace D'_m for the normal distribution by $\mathscr{D}_m$, the following equation holds from Equations (34) and (36):

$$\mathscr{D}_m = \tfrac{1}{2} \{ \log_2 |S_m| - \log_2 |S_{m+1}| \} , \tag{37}$$

where

$$|S_{m+1}| = \begin{vmatrix} 1 & \varrho_1 & \cdots & & \varrho_{m-1} & \varrho_m \\ \varrho_1 & 1 & \varrho_1 & \cdots & \varrho_{m-2} & \varrho_{m-1} \\ \vdots & \vdots & & & \vdots & \vdots \\ \varrho_{m-1} & \varrho_{m-2} & \cdots & & 1 & \varrho_1 \\ \varrho_m & \varrho_{m-1} & \cdots & & \varrho_1 & 1 \end{vmatrix}. \tag{38}$$

Here we designate $\mathscr{D}_m$ as simplified dependency.

Table 3. Comparison between the bias of $\hat{D}_1$ and of $\tilde{D}_1$ when $n_s = 5$ and $N = 250$

Model Name	Bias of $\hat{D}_1$	Bias of $\tilde{D}_1$
NORML 113	0.32	0.15
GAMMA 115	0.46	0.00
GAMMA 132	0.73	0.10
WOLDS 101	3.21	0.24
SEMI 1133	0.59	0.02
SEMI 1213	0.34	0.25
SEMI 1353	0.22	0.09
SEMI 1363	0.15	0.08
SEMI 1116	0.62	0.20
SEMI 2133	1.50	0.39
SEMI 2026	2.31	0.56

Bias of $\hat{D}_1 = |\bar{\hat{D}}_1 (N=250) - D_1| / D_1$; and of $\tilde{D}_1 = |\bar{\tilde{D}}_1 (N=250) - D_1| / D_1$. The value of $\hat{D}_1 (N=8000)$ is used for the true value D_1. Values $\bar{\hat{D}}_1$ and $\bar{\tilde{D}}_1$ are arithmetic mean of $\hat{D}_1$ and $\tilde{D}_1$ calculated, respectively, from 16 subsequences chosen randomly from a sequence ($N = 8000$)

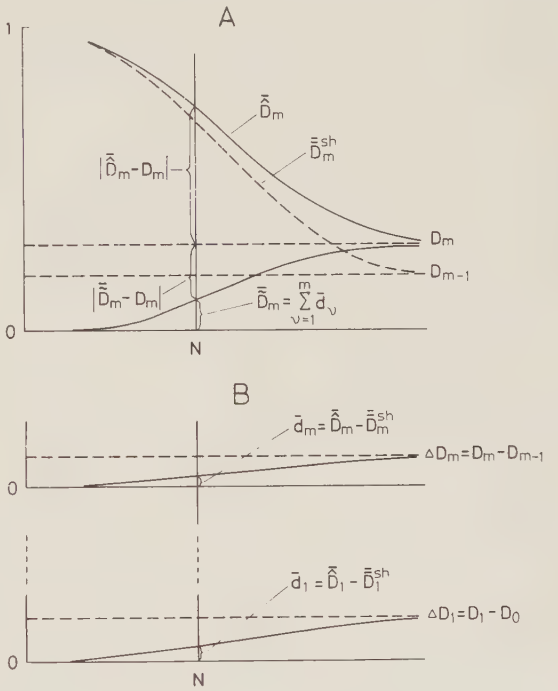

Fig. 6A and B. Scheme illustrating smaller bias of $\tilde{D}_m$ than $\hat{D}_m$. Explanations see text

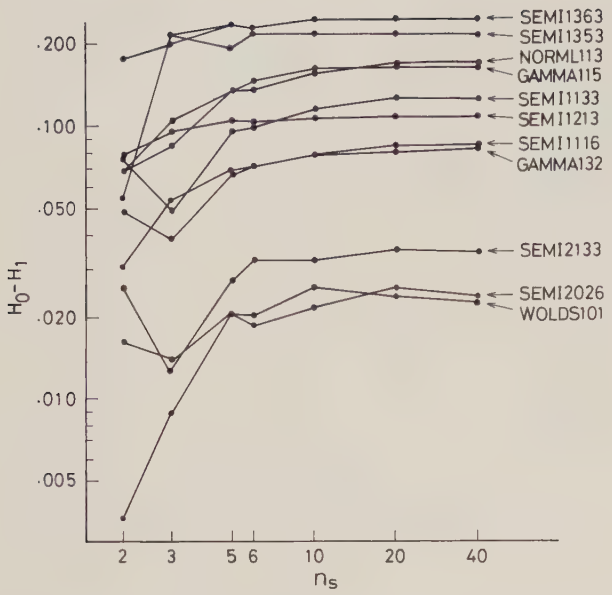

Fig. 7. Relation between H_0-H_1 and n_s. Values H_0-H_1 are estimated by $\tilde{D}_1 \times H_0$. $N=8000$ when $n_s=2$–10; and $N=32000$ when $n_s=20$, 40

4.3 Inference of the Order by Simplified Dependency

The estimate of simplified dependency $\mathscr{D}_m$ is given from Equation (37) by the following equation in the case of a finite sample size:

$$\hat{\mathscr{D}}_m=\tfrac{1}{2}\{\log_2|\hat{S}_m|-\log_2|\hat{S}_{m+1}|\}, \tag{39}$$

where $|\hat{S}_m|$ is the estimate of $|S_m|$, being calculated from $\hat{\varrho}_1, \hat{\varrho}_2, \ldots, \hat{\varrho}_{m-1}$. The value $\hat{\varrho}_i$ is calculated from the original vector series given by Equation (12), and

$$\hat{\varrho}_i=\frac{1}{N-m-i}\frac{1}{\sigma^2}\sum_{t=m+2}^{N-m-i}(x_{t-m+j}-\bar{x})(x_{t-m+k}-\bar{x}) \tag{40}$$

for

$$i=|j-k|=1,2,\ldots,m-1.$$

The null hypothesis for the test of the order of Markov process is as follows:

$$\Delta\mathscr{D}_m=\mathscr{D}_m-\mathscr{D}_{m-1}=0. \tag{41}$$

Accordingly if we could obtain the sampling distribution of Markov value of the order m, $\Delta\hat{\mathscr{D}}_m$, when the null hypothesis is true, we could test the hypothesis concerning the observed value $\Delta\hat{\mathscr{D}}_m$:

$$\Delta\hat{\mathscr{D}}_m=\hat{\mathscr{D}}_m-\hat{\mathscr{D}}_{m-1} \tag{42}$$

As described previously [3.4], to obtain the sampling distribution of $\Delta\hat{\mathscr{D}}_m$ it is enough to obtain the distribution of

$$\Delta\hat{\mathscr{D}}_m^{\mathrm{sh}}=\hat{\mathscr{D}}_m^{\mathrm{sh}}-\mathscr{D}_{m-1}. \tag{43}$$

Here $\hat{\mathscr{D}}_m^{\mathrm{sh}}$ is the estimate of $\mathscr{D}_m$ when the m-th order shuffling is made. That is,

$$\hat{\mathscr{D}}_m^{\mathrm{sh}}=\tfrac{1}{2}\{\log_2|\hat{S}_m^{\mathrm{sh}}|-\log_2|\hat{S}_{m+1}^{\mathrm{sh}}|\}, \tag{44}$$

where

$$|\hat{S}_m^{\mathrm{sh}}|=\begin{vmatrix} 1 & \hat{\varrho}_1^{\mathrm{sh}} & \cdots & & \hat{\varrho}_{m-1}^{\mathrm{sh}} \\ \hat{\varrho}_1^{\mathrm{sh}} & 1 & \hat{\varrho}_1 & \cdots & \hat{\varrho}_{m-2} \\ \vdots & \hat{\varrho}_1 & & & \vdots \\ & \vdots & & & \hat{\varrho}_1 \\ \hat{\varrho}_{m-1}^{\mathrm{sh}} & \hat{\varrho}_{m-2} & \cdots & \hat{\varrho}_1 & 1 \end{vmatrix} \tag{45}$$

and

$$|\hat{S}_{m+1}^{\mathrm{sh}}|=\begin{vmatrix} 1 & \hat{\varrho}_1^{\mathrm{sh}} & \cdots & & \hat{\varrho}_{m-1}^{\mathrm{sh}} & \hat{\varrho}_m^{\mathrm{sh}} \\ \hat{\varrho}_1^{\mathrm{sh}} & 1 & \hat{\varrho}_1 & \cdots & \hat{\varrho}_{m-2} & \hat{\varrho}_{m-1} \\ \vdots & \vdots & & & \vdots & \vdots \\ \hat{\varrho}_{m-1}^{\mathrm{sh}} & \hat{\varrho}_{m-2} & \cdots & & 1 & \hat{\varrho}_1 \\ \hat{\varrho}_m^{\mathrm{sh}} & \hat{\varrho}_{m-1} & \cdots & & \hat{\varrho}_1 & 1 \end{vmatrix} \tag{46}$$

from the definition of the shuffling described previously [3.4]. Here $\hat{\varrho}_i^{\mathrm{sh}}$ is the estimate of correlation coefficient calculated from the shuffled vector series given by Equation (23), and

$$\hat{\varrho}_i^{\mathrm{sh}}=\frac{1}{N-m-i}\frac{1}{\sigma^2}\sum_{t=m+1}^{N-m-i}(x_{t-m}^{\mathrm{sh}}-\bar{x})(x_{t-m+i}-\bar{x}) \tag{47}$$

for

$$i=1,2,\ldots,m.$$

On the other hand, when sample size N is sufficiently large, $\hat{\varrho}_i(i=1,2,\ldots,m-1)$ is regarded as fixed not to vary by the shuffling, and is given by Equation (40) similarly to the original series. Therefore $\mathscr{D}_{m-1}$ is regarded as known, and is given by

$$\mathscr{D}_{m-1}\approx\hat{\mathscr{D}}_{m-1}=\tfrac{1}{2}\{\log_2|\hat{S}_{m-1}|-\log_2|\hat{S}_m|\}. \tag{48}$$

From Equations (43)—(48) $\Delta\hat{\mathscr{D}}_m^{\mathrm{sh}}$ is obtained.

Under the condition that $|\hat{S}_m|$ is known, $|\hat{S}_{m+1}^{\mathrm{sh}}|$ of Equation (44) is as follows (Appendix 7):

$$|\hat{S}_{m+1}^{\mathrm{sh}}|=|\hat{S}_m|\left(1-\frac{\chi_m^2}{N}\right), \tag{49}$$

where χ_m^2 is given by Equation (105) and has the chi-square distribution with m degrees of freedom.

When $m=1$, from Equations (43), (44) and (49)

$$\begin{aligned}\Delta\hat{\mathscr{D}}_1^{\mathrm{sh}}&=\hat{\mathscr{D}}_1^{\mathrm{sh}}\\&=-\tfrac{1}{2}\log_2|\hat{S}_2^{\mathrm{sh}}|\\&=-\tfrac{1}{2}\log_2\left(1-\frac{\chi_1^2}{N}\right).\end{aligned} \tag{50}$$

Equation (50) indicates that $\Delta\hat{\mathscr{D}}_1^{\mathrm{sh}}$ is a monotonically increasing function of χ_1^2. Accordingly we could obtain the critical value of $\Delta\hat{\mathscr{D}}_1^{\mathrm{sh}}$, $\Delta\mathscr{D}_1^{\alpha}$, for a given level of significance α with the use of the critical value $\chi_1^2(\alpha)$.

That is,

$$\Delta\mathscr{D}_1^{\alpha} = -\tfrac{1}{2}\log_2\left(1-\frac{\chi_1^2(\alpha)}{N}\right). \tag{51}$$

It was shown in our models that the critical values calculated by Equation (51) were located in an appropriate point of the empirical distribution of $\Delta\hat{D}_1^{sh}$ (Fig. 8). This indicates that Equation (51) is applicable for the determination of the critical value of $\Delta\hat{\mathscr{D}}_1^{sh}$.

In the case of $m \geqq 2$, it is theoretically shown that Equations (50) and (51) could also be used when $N \gg m$ (Appendix 8). In fact, the empirical distribution of $\Delta\hat{\mathscr{D}}_m^{sh}$ for $m=1,2,\ldots,10$ corresponded well with each other (Fig. 9). Accordingly we could use Equation (51) as the critical value, $\Delta\mathscr{D}_m^{\alpha}$, of $\Delta\hat{\mathscr{D}}_m^{sh}$ (Table 4).

4.4 Point Estimation of Simplified Dependency

The values of simplified dependency $\hat{\mathscr{D}}_m$ converge rapidly to constant values as m increases when $m \leqq 10$ and $N \geqq 1000$ (Fig. 10). The bias of the point estimate of $\mathscr{D}_m$ is small. Accordingly from the viewpoint of practice, it is not necessary to shuffle the original sequence when we use $\hat{\mathscr{D}}_m$ for the point estimation of $\mathscr{D}_m$. The profile of $\hat{\mathscr{D}}_m$ for simulated models is indicated in Figure 11 as a function of m. The values $\hat{\mathscr{D}}_m$ increase monotonically and converge to a constant value as m increases.

4.5 Relation between Simplified Dependency and Autoregressive Analysis

Firstly we consider a stationary autoregressive series x_t. If we assume the normality of x_t, x_t generated by the following linear relation gives the best estimate of x_t in terms of $x_{t-1}, x_{t-2}, \ldots, x_{t-m}$, since $E[x_t|x_{t-1}, x_{t-2}, \ldots, x_{t-m}] = a_0 + a_1 x_{t-1} + a_2 x_{t-2} + \ldots + a_m x_{t-m}$ (Wilks, 1962; Papoulis, 1965):

$$x_t = a_0 + a_1 x_{t-1} + a_2 x_{t-2} + \ldots + a_m x_{t-m} + \varepsilon_t, \tag{52}$$

where ε_t is the residual in the estimation. The expected value of ε_t and the mean-square error of ε_t are given by the following equations, respectively:

$$E[\varepsilon_t] = E[\{x_t - (a_0 + a_1 x_{t-1} + a_2 x_{t-2} + \ldots + a_m x_{t-m})\}] = 0, \tag{53}$$

$$E[\varepsilon_t^2] = E[\{x_t - (a_0 + a_1 x_{t-1} + a_2 x_{t-2} + \ldots + a_m x_{t-m})\}^2]. \tag{54}$$

The coefficients a_i which minimize Equation (54) are given by the solutions of the following equations:

$$\begin{aligned} &a_1 + \varrho_1 a_2 + \varrho_2 a_3 + \ldots + \varrho_{m-1} a_m = \varrho_1, \\ &\varrho_1 a_1 + a_2 + \varrho_1 a_3 + \ldots + \varrho_{m-2} a_m = \varrho_2, \\ &\quad\vdots \\ &\varrho_{m-1} a_1 + \varrho_{m-2} a_2 + \varrho_{m-3} a_3 + \ldots + a_m = \varrho_m \end{aligned} \tag{55}$$

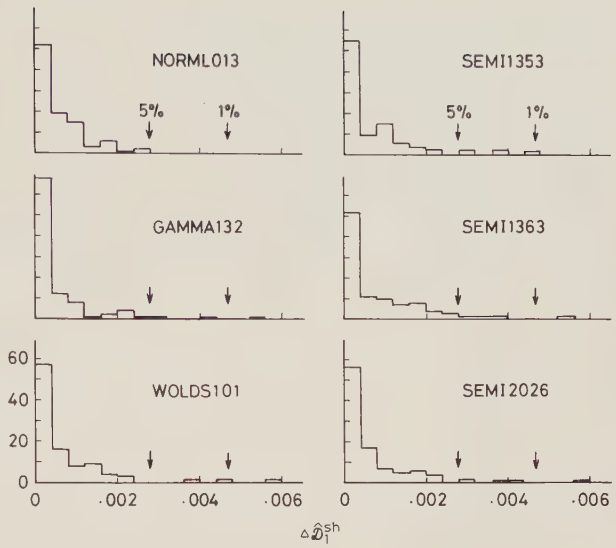

Fig. 8. Some examples of the empirical distributions of $\Delta\hat{\mathscr{D}}_1^{sh}$. The arrows show the theoretical upper α points ($\alpha = 5\%, 1\%$). Shuffling was made 100 times. Ordinates, frequency. $N = 1000$

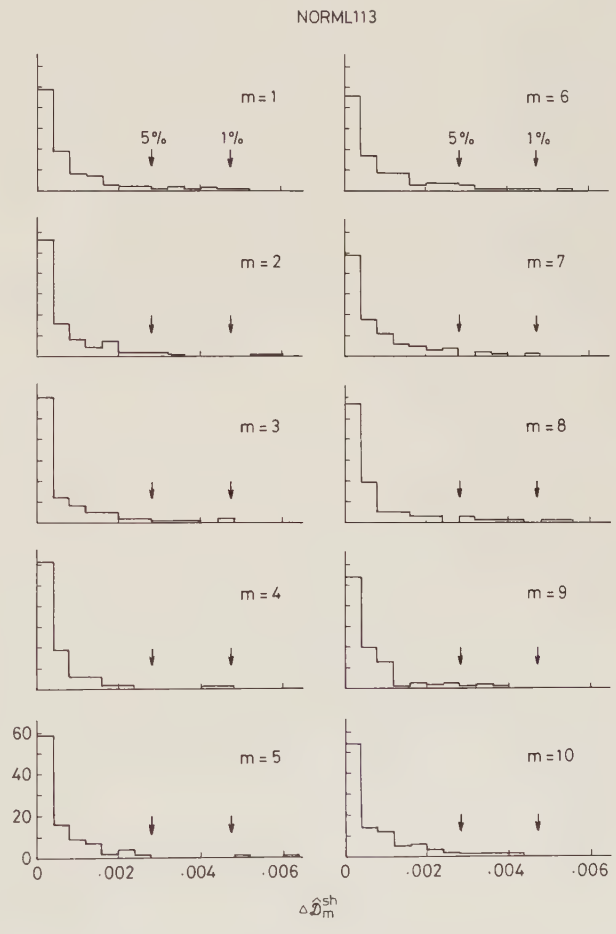

Fig. 9. An example illustrating the empirical distributions of $\Delta\hat{\mathscr{D}}_m^{sh}$ ($m = 1-10$). Other explanations are the same as in Figure 8

Table 4. Critical values $\Delta\hat{\mathcal{D}}_m^{\alpha}$

N	$\Delta\hat{\mathcal{D}}_m^{\alpha=0.01}$	$\Delta\hat{\mathcal{D}}_m^{\alpha=0.05}$
125	0.0393	0.0225
250	0.0194	0.0094
500	0.0096	0.0055
1000	0.0047	0.0028
2000	0.0024	0.0014
4000	0.0012	0.0007
8000	0.0006	0.0003

and

$$a_0=\mu\left(1-\sum_{i=1}^{m} a_i\right), \tag{56}$$

where $\mu=E(x_t)$. Then the least mean-square error e_m is given by the following:

$$e_m=\sigma_0^2\left(1-\sum_{i=1}^{m} a_i\varrho_i\right), \tag{57}$$

where $\sigma_0^2=\mathrm{Var}(x_t)$. Furthermore for normal process the conditional variance σ_m^2 equals the least mean square error:

$$\begin{aligned}\sigma_m^2&=E[\{x_t-(a_0+a_1x_{t-1}+a_2x_{t-2}+\ldots+a_mx_{t-m})\}^2\\&\quad|x_{t-1},x_{t-2},\ldots,x_{t-m}]\\&=E[\{x_t-(a_0+a_1x_{t-1}+a_2x_{t-2}+\ldots+a_mx_{t-m})\}^2]\\&=e_m\end{aligned}$$

In general, the increase of the previous data improves the estimation with the decrease of σ_m^2.

Secondly we consider how to determine the order of dependence in normal process. The linear correlation ratio is defined by the following equation (Wilks, 1962):

$$\eta_m=\frac{\sigma_m^2}{\sigma_0^2}=1-\sum_{i=1}^{m} a_i\varrho_i. \tag{58}$$

It is evident that $0\leqq\eta_m\leqq 1$. The value 0 occurs only if $P[x_t=E[x_t|x_{t-1},x_{t-2},\ldots,x_{t-m}]|x_{t-1},x_{t-2},\ldots,x_{t-m}]=1$, that is, for normal process, if and only if $x_t, x_{t-1},\ldots$, and x_{t-m} are properly linearly dependent. The value 1 occurs only if x_t and $(x_{t-1}, x_{t-2}, \ldots, x_{t-m})$ are uncorrelated, that is, for normal process, if and only if x_t and $(x_{t-1}, x_{t-2}, \ldots, x_{t-m})$ are independent. We could determine the order of dependence with the linear correlation ratio η_m. The linear correlation ratio η_m decreases monotonically as the order m increases. Let $\Delta\eta_m$ denote the increment of η_m concerning m:

$$\Delta\eta_m=\eta_m-\eta_{m-1}. \tag{59}$$

If $\Delta\eta_m=0$ for all $m\geqq m_0+1$, then m_0 gives the order of dependence. In fact, if $\eta_m=\eta_{m+1}$,

$$\begin{aligned}&E[x_t|x_{t-1},x_{t-2},\ldots,x_{t-m}]\\&\quad=E[x_t|x_{t-1},x_{t-2},\ldots,x_{t-m-1}].\end{aligned} \tag{60}$$

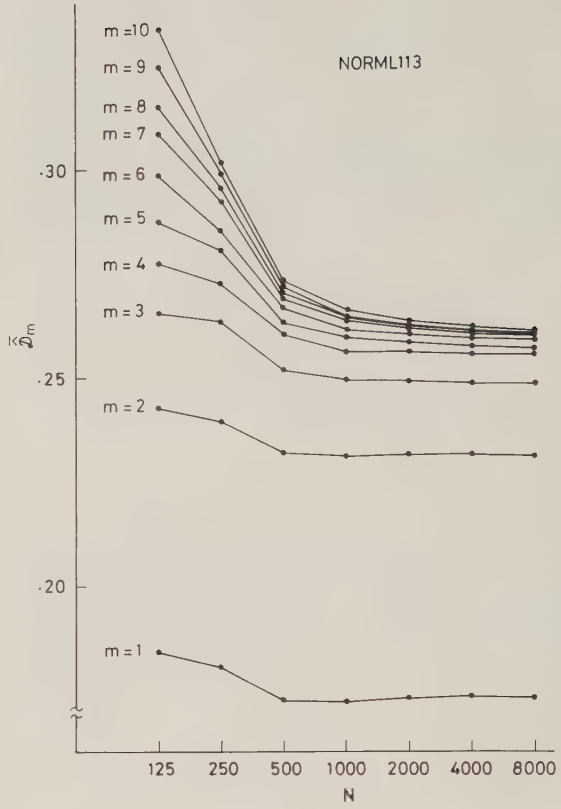

Fig. 10. An example indicating the relation between $\bar{\hat{\mathcal{D}}}_m$ $(m=1-10)$ and N (125–8000)

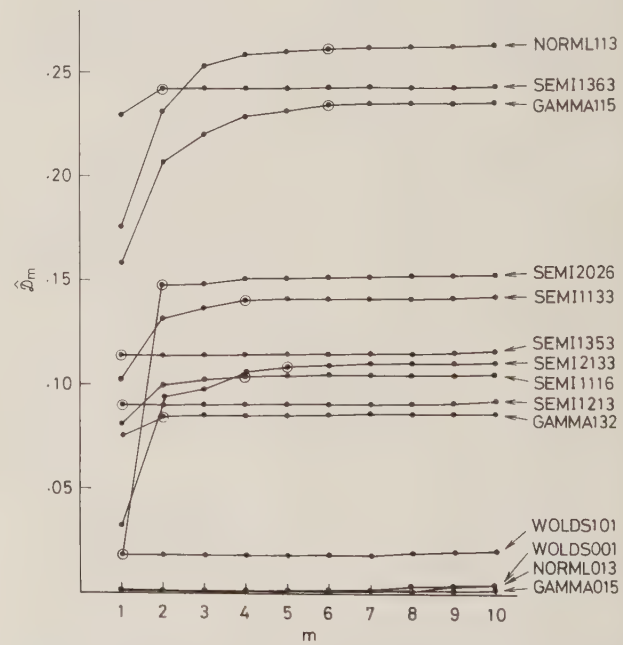

Fig. 11. Relation between $\hat{\mathcal{D}}_m$ and m. The values m corresponding to open circles indicate the order of Markov properties of each models estimated with $\Delta\hat{\mathcal{D}}_m^{\alpha}$ $(\alpha=0.01)$. $N=4000$

Eq. (60) indicates that the normal process concerned is the m-th order Markov process. The above description suggests us that this autoregressive analysis is equivalent to simplified dependency analysis. Simplified dependency defined by Equation (37) reduces to

$$\mathscr{D}_m = \frac{1}{2}\log_2 \frac{|S_m|}{|S_{m+1}|}. \tag{61}$$

Equation (38) reduces to

$$|S_{m+1}| = \begin{vmatrix} 1-a_1\varrho_1-a_2\varrho_2 & \cdots & -a_m\varrho_m & \varrho_1 & \varrho_2 & \varrho_m \\ \varrho_1-a_1-a_2\varrho_1 & \cdots & -a_m\varrho_{m-1} & 1 & \varrho_1 & \varrho_{m-1} \\ \varrho_2-a_1\varrho_1-a_2 & \cdots & -a_m\varrho_{m-2} & \varrho_1 & 1 & \varrho_{m-2} \\ \vdots & & & \vdots & \vdots & \vdots \\ \varrho_m-a_1\varrho_{m-1}-a_2\varrho_{m-2} & \cdots & -a_m & \varrho_{m-1} & \varrho_{m-2} & 1 \end{vmatrix}. \tag{62}$$

From Equation (55), Equation (62) becomes

$$|S_{m+1}| = \frac{\sigma_m^2}{\sigma_0^2}|S_m|.$$

Accordingly

$$\frac{|S_m|}{|S_{m+1}|} = \frac{\sigma_0^2}{\sigma_m^2} = \frac{1}{\eta_m}.$$

Then Equation (61) reduces to

$$\mathscr{D}_m = \frac{1}{2}\log_2 \frac{1}{\eta_m}. \tag{63}$$

Furthermore $\Delta\mathscr{D}_m$ can also be expressed in terms of η_m:

$$\Delta\mathscr{D}_m = \mathscr{D}_m - \mathscr{D}_{m-1} = -\frac{1}{2}(\log_2\eta_m - \log_2\eta_{m-1}). \tag{64}$$

Equations (63) and (64) indicate that simplified dependency is calculated from the correlation ratio η_m.

5. Concluding Remarks

5.1 Physical Meaning of Dependency

Dependency is a statistical measure representing degrees of dependence of Markov process. Degrees of time dependent or Markov properties of the time series of events are compared with each other with this measure.

Dependency is essentially different from serial correlation coefficient which is usually employed for expressing time dependent properties. Serial correlation coefficients are expressed as the profile of the coefficients of each order (Fig. 12). On the other hand, a total value of time dependent properties of a time series is represented by dependency, but not by serial correlation. For example, as shown in Figures 11 and 12, it is indicated with the use of dependency that the value of Markov properties of a model NORML 113 ($\hat{\mathscr{D}}_{10}=0.263$) is approximately twice as large as that of another model SEMI 1133 ($\hat{\mathscr{D}}_{10}=0.143$).

It seems to be generally convinced that the higher the order of Markov process, the larger the degree of time dependence. However this is not necessarily correct. When a time series has the higher order Markov property with very small values, its degree of time dependence could not be regarded as large. Even if the order is lower, there are certain cases in which the degrees of time dependence could be regarded as large (Fig. 11). Thus dependency gives a quantity to evaluate the degrees of dependence as well as the order of Markov process. Even from this viewpoint, dependency forms a new notion of Markov properties.

5.2 Markov Value

Markov value of the order m is given by ΔD_m and $\Delta\mathscr{D}_m$ for discrete and continuous variables, respectively. This represents the contribution to a total value of Markov properties given by dependency D_m and $\mathscr{D}_m$. Accordingly the profile of Markov values of each order m ($m=1,2,\ldots,m$) expresses the weights of the contribution to the total value (Fig. 13). The order of Markov process is effectively determined with the value m in which Markov value becomes to be approximately *zero*.

The estimate of Markov value for continuous variables, $\Delta\hat{\mathscr{D}}_m$, has very small bias, and the critical value of $\Delta\hat{\mathscr{D}}_m^{\mathrm{sh}}$ could be determined by $\Delta\mathscr{D}_1^{\alpha}$ [Eq. (51)] regardless of m (Table 4). On the other hand, in the case of the estimation of Markov value for discrete variables, $\Delta\hat{D}_m$ has large bias, although d_m has small one. Accordingly to estimate Markov value it is effective to employ d_m. To estimate a total value of Markov properties it is useful to employ $\tilde{D}_m$, since the bias of $\tilde{D}_m$ is smaller than that of $\hat{D}_m$.

The following equation holds from Equations (20) and (28):

$$d_m = \Delta\hat{D}_m + (\hat{D}_{m-1} - \bar{D}_m^{\mathrm{sh}}), \tag{65}$$

where $\hat{D}_{m-1}$ is known, and $\bar{D}_m^{\mathrm{sh}}$ is obtained by the m-th order shuffling. Then the critical value of d_m is obtainable from that of $\Delta\hat{D}_m$.

5.3 Effectiveness of Shuffling

The m-th order shuffling [3.4] offers an effective method to obtain the sampling distribution of $\Delta\hat{D}_m^{\mathrm{sh}}$ for

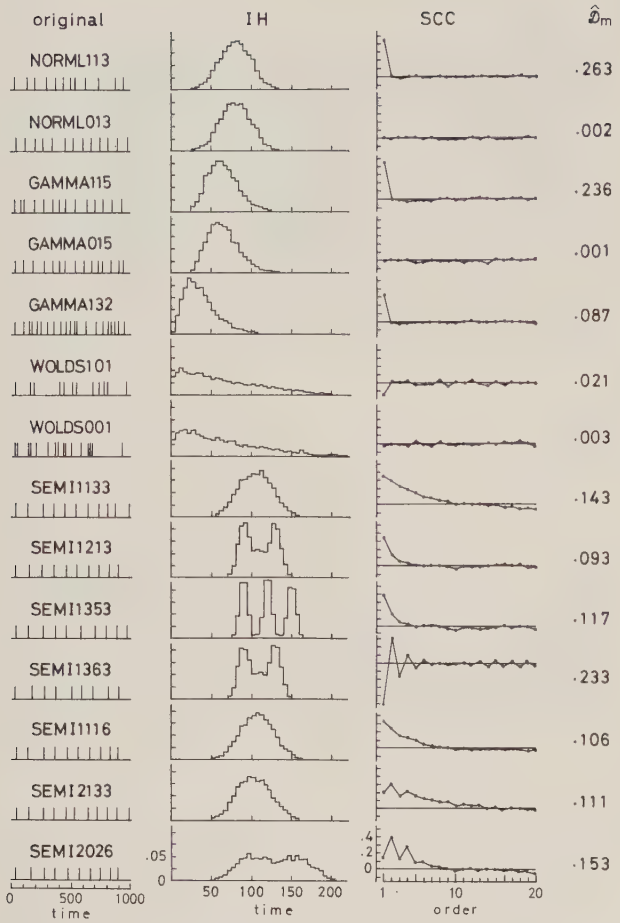

Fig. 12. Showing the pattern of original interval sequences of 14 models, their interval histograms (IH) with bin width 5 time units, serial correlograms (SCC), and the value $\hat{\mathcal{D}}_m$ for $m=10$. $N=4000$

the purpose of the order estimation and to get $\tilde{D}_m$ which is a better point estimator of D_m. In these cases sample size is necessary to be sufficiently large.

To get a better point estimate of D_m and to estimate the order, it is empirically concluded with the use of $\tilde{D}_m$ that the following condition for sample size is necessary to hold:

$$N \gtrsim 10 \times n_s^{m+1} . \tag{66}$$

This corresponds to the condition that more than 10 entries, in the mean, are necessary for each one of unit bins to estimate the transition probability.

5.4 State Space and Definition of Dependency

Dependency is defined by Equation (6) for the state space of discrete variables. According to this definition, the values of dependency cover between 0 and 1, and the degrees of Markov properties of the time series are compared with each other regardless of entropy H_0 or uncertainty of the series. For example we could compare the degree of Markov properties of German words with that of English ones, although H_0s of these words are different.

For the state space of continuous variables it is impossible to define dependency in the same manner of Equation (6) [4.1]. Then we have defined, in this paper, dependency for continuous variables by the limit of mutual information when $\tau \to 0$. In this case the values of dependency are non-negative numbers.

Under the assumption that the time series has continuous variables and the normal distribution,

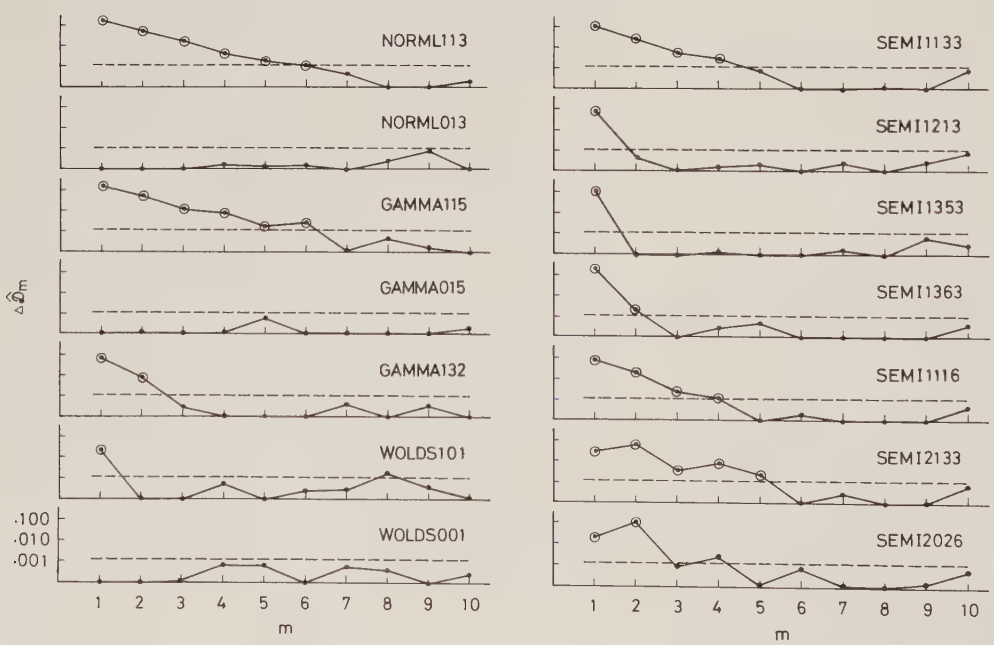

Fig. 13. Relation between Markov values $\Delta\hat{\mathcal{D}}_m$ (ordinates) and m (abscissae). Broken lines, critical values $\Delta\mathcal{D}_m^{\alpha}$ ($\alpha=0.01$) when $N=4000$ (see Table 4). Other explanations are the same as in Figure 11

simplified dependency $\mathscr{D}_m$ is defined by Equation (37). The statistic $\hat{\mathscr{D}}_m$ is practically useful for the estimation of the order and the values of Markov properties with relatively small sample size.

When the state space of the time series is not determined uniquely to our present knowledge such as in neuronal spike trains or when the sampling distribution is considerably distorted from the normal, it might be necessary for the estimation of the order and the values to use dependency of both discrete and continuous variables. By comparing with these results we could obtain a valid conclusion.

5.5 Relation among D_m, D'_m and $\mathscr{D}_m$

If we define Markov process of continuous variables in the normal distribution by the discrete state space quantized by τ, the following relation holds among D_m and D'_m and $\mathscr{D}_m$:

$$D_m \times H_0 \to D'_m = \mathscr{D}_m(\tau \to 0, n_s \to \infty). \tag{67}$$

This is based on the theorem that mutual information which is the numerator of D_m increases monotonically to converge to a constant value when $\tau \to 0$ (Fano, 1961). It is indicated in Table 5 that Equation (67) holds when $m=1$.

Appendix 1

Generation of Normally Distributed Interval Sequence. According to the central limit theorem, the probability distribution of the sum of k independently and identically distributed random variables r_j with respective means μ_j and variances σ_j^2, as k becomes very large, approaches the normal distribution asymptotically with mean $\mu_x = \sum_{j=1}^{k} \mu_j$ and variance $\sigma_x^2 = \sum_{j=1}^{k} \sigma_1^2$ (Cramér, 1963).

Let r_j be uniformly distributed mutually independent variables defined by the unit interval (0, 1). Then

$$x_t = \sigma_x \left(\frac{12}{k}\right)^{\frac{1}{2}} \cdot \left(\sum_{j=1+(t-1)(k-P)}^{k+(t-1)(k-P)} r_j - \frac{k}{2} \right) + \mu_x \quad (t=1,2,\ldots) \tag{68}$$

forms the normal distribution with μ_x and σ_x^2 (Naylor et al., 1967). In order to generate a time series $\{x_t\}$ $(t=1,2,\ldots)$ with serial correlation coefficients ϱ_i, P $(1 \leqq P < k)$ of the r_j random numbers are necessary to be common to the successive sums. Here ϱ_i of $\{x_t\}$ is given by

$$\varrho_i = 1 - \frac{k-P}{k} i, \tag{69}$$

if $i \leqq k/(k-P)$.

The interval sequence (NORML 113) is generated when $\mu_x = 80.0$, $\sigma_x = 20.0$, $k=24$ and $P=11$. Then $\varrho_1 = 0.46$. NORML 013 is obtained as a result of 2 times shuffling of NORML 113 when $N = 32000$.

Table 5. Relation among D_1, D'_1, and $\mathscr{D}_1$

Model Name	D_1	D'_1	$\mathscr{D}_1$
NORML 113	0.0354	0.169	0.176
GAMMA 115	0.0331	0.164	0.158
GAMMA 132	0.0167	0.083	0.076
WOLDS 101	0.0047	0.023	0.018
SEMI 1133	0.0261	0.124	0.103
SEMI 1213	0.0213	0.108	0.090
SEMI 1353	0.0447	0.218	0.115
SEMI 1363	0.0488	0.247	0.230
SEMI 1116	0.0180	0.086	0.081
SEMI 2133	0.0072	0.034	0.033
SEMI 2026	0.0047	0.024	0.019

The value of $\tilde{D}_1(N=32000)$ is used for the true value D_1, when the state space of the interval sequence is considered to be discrete $(n_s=40)$; and $\tilde{D}_1 \times H_0(N=32000)$ for D'_1 and $\hat{\mathscr{D}}_1(N=8000)$ for $\mathscr{D}_1$, when the state space is considered to be continuous

Appendix 2

Generation of Time Series with Gamma Distribution. The probability distribution of the sum of k independent exponential variables each with parameter α is gamma with parameters α and k (Naylor et al., 1967).

Let r_j be uniformly distributed mutually independent variables defined by the unit interval (0, 1). Then

$$x_t = -\frac{1}{\alpha} \sum_{j=1+(t-1)(k-P)}^{k+(t-1)(k-P)} \ln r_j = -\frac{1}{\alpha} \ln \prod_{j=1+(t-1)(k-P)}^{k+(t-1)(k-P)} r_j \tag{70}$$

forms the gamma distribution with mean k/α and variance k/α^2. To generate a time series $\{x_t\}$ with ϱ_i, P of the r_j random numbers are necessary to be common to the successive products. Here ϱ_i is also given by Equation (69).

The interval sequence (GAMMA 115) is generated when $\mu_x = k/\alpha = 67.0$, $\sigma_x^2 = k/\alpha^2 = 400.0$, $k=11$, and $P=5$. Then $\varrho_1 = 0.45$. GAMMA 015 is obtained as a result of 2 times shuffling of GAMMA 115 when $N=32000$. GAMMA 132 is generated when $\mu_x = 37.5$, $\sigma_x^2 = 468.7$, $k=3$ and $P=1$. Then $\varrho_1 = 0.33$.

Appendix 3

Interval Sequence Generated by Wold's Markov Process. Here the outline of the generation is described (Wold, 1948; Cox and Lewis, 1966). A detailed description is available in the paper of Yanaru and Nakahara (1974). Let the following equation be the 2-dimensional probability density function for random variables x_t, x_{t+1} $(t=1,2,3,\ldots)$:

$$f_2(x_1, x_2) = \frac{1}{2}(x_1+x_2)\exp\{-(x_1+x_2)\} \quad (x_1, x_2 \geqq 0). \tag{71}$$

Then marginal probability density function for x_2 is given by

$$f_1(x_2) = \frac{1}{2}(1+x_2)\exp(-x_2) \tag{72}$$

Since $f_2(x_1, x_2) \neq f_1(x_1) f_1(x_2)$, x_1 is dependent on x_2. In the case of $x_2 < \infty$, $f_1(x_2) > 0$. Then the conditional probability density function is as follows:

$$g_1(x_1|x_2) = f_2(x_1, x_2)/f_1(x_2)$$
$$= \frac{x_1 + x_2}{1 + x_2} \exp(-x_1) \quad (x_1 \geqq 0, 0 \leqq x_2 < \infty). \tag{73}$$

For the generation of the interval sequence the following transition probability distribution function derived from the transition probability density function is employed:

$$F(x|x_2) = \int_0^x g_1(x_1|x_2). \tag{74}$$

Let U be the uniform random number of the interval (0, 1), then it is sufficient to obtain the root $x = x_1$ of the following equation:

$$U = F(x|x_2). \tag{75}$$

That is, in our case

$$F(x|x_2) = \int_0^x \left(\frac{x_1 + x_2}{1 + x_2}\right) \exp(-x_1) dx_1$$
$$= 1 - \{1 + A(x_2)x\} \exp(-x), \tag{76}$$

where

$$A(x_2) = \frac{1}{1 + x_2}.$$

Then

$$\{1 + A(x_2)x\} \exp(-x) = 1 - U.$$

Since $1 - U$ is also the uniform random number, it is sufficient to solve the following equation:

$$\{1 + A(x_2)x\} \exp(-x) - U = 0.$$

Here we obtain various distributions by varying the coefficient Θ of the following equation:

$$\left\{1 + \frac{\Theta x}{1 + \Theta x_2}\right\} \exp(-\Theta x) - U = 0. \tag{77}$$

We solve Equation (77) with the Newton-Raphson method. When the initial value of x_2 is given, and random number U is generated, the root of Equation (77), $x = x_1$, is obtained if the convergence condition is satisfied. Let $x = x_1$ be the 1st interval of the sequence. Then x_1 is substituted for x_2 in Equation (77), and random number U is newly generated. The 2nd interval is obtained as the root of Equation (77). Similarly the 3rd... intervals are derived. To exclude the influence of the initial value, the first 100 intervals are abandoned.

The interval sequence (WOLDS 101) is generated when $\Theta = 1.0$. WOLDS 001 is obtained as a result of 2 times shuffling of WOLDS 101 when $N = 32000$.

Appendix 4

Interval Sequence Generated by Semi-Markov Process. The rows of the transition matrix $[P_{ij}]$ are utilized to generate a Markov chain. In the following generation of the 1st order Markov chain is described. Let r be a uniform random number in the (0, 1) interval, and i be a previous state of the intervals. If

$$\sum_{q=1}^{j} P_{iq} < r \leqq \sum_{q=1}^{j+1} P_{iq} \tag{78}$$

is satisfied, the next state becomes j. From a given probability distribution corresponding to j an interval is generated. Here we give the normal distribution with mean μ_q ($q = 1, 2, \ldots, j, \ldots, n_s$) and standard deviation σ at each state k. Thus the interval sequence generated by the n_s-state 1st order semi-Markov process is obtained (Perkel et al., 1967; Nakahama et al., 1974). The interval sequence generated by the 2nd order semi-Markov process is similarly obtained with the 3-dimensional transition matrix.

The interval sequence of the 1st order semi-Markov process (SEMI 1133) were generated with the transition matrix

$$\begin{bmatrix} 0.85 & 0.10 & 0.05 \\ 0.45 & 0.10 & 0.45 \\ 0.05 & 0.10 & 0.85 \end{bmatrix}$$

with $\mu_1 = 90.0$, $\mu_2 = 105.0$, $\mu_3 = 120.0$ and $\sigma = 15.0$; SEMI 1213, with

$$\begin{bmatrix} 0.60 & 0.20 & 0.20 \\ 0.45 & 0.10 & 0.45 \\ 0.20 & 0.20 & 0.60 \end{bmatrix}$$

with $\mu_1 = 90.0$, $\mu_2 = 110.0$, $\mu_3 = 130.0$ and $\sigma = 7.0$; SEMI 1353, with

$$\begin{bmatrix} 0.6 & 0.2 & 0.2 \\ 0.2 & 0.6 & 0.2 \\ 0.2 & 0.2 & 0.6 \end{bmatrix}$$

with $\mu_1 = 90.0$, $\mu_2 = 120.0$, $\mu_3 = 150.0$ and $\sigma = 5.0$; SEMI 1363, with

$$\begin{bmatrix} 0.10 & 0.20 & 0.70 \\ 0.45 & 0.10 & 0.45 \\ 0.70 & 0.20 & 0.10 \end{bmatrix}$$

with $\mu_1 = 90.0$, $\mu_2 = 110.0$, $\mu_3 = 130.0$ and $\sigma = 7.0$; and SEMI 1116, with

$$\begin{bmatrix} 0.60 & 0.20 & 0.10 & 0.05 & 0.03 & 0.02 \\ 0.35 & 0.25 & 0.20 & 0.10 & 0.05 & 0.05 \\ 0.30 & 0.25 & 0.20 & 0.10 & 0.10 & 0.05 \\ 0.05 & 0.10 & 0.10 & 0.20 & 0.25 & 0.30 \\ 0.05 & 0.05 & 0.10 & 0.20 & 0.25 & 0.35 \\ 0.02 & 0.03 & 0.05 & 0.10 & 0.20 & 0.60 \end{bmatrix}$$

with $\mu_1 = 90.0$, $\mu_2 = 97.0$, $\mu_3 = 104.0$, $\mu_4 = 111.0$, $\mu_5 = 118.0$, $\mu_6 = 125.0$ and $\sigma = 15.0$.

The interval sequence of the 2nd order semi-Markov process (SEMI 2133) were generated with the transition matrix

$$\begin{array}{c} \\ (1,k) \\ \\ \\ (2,k) \\ \\ \\ (3,k) \\ \\ \end{array} \begin{array}{c} (l) \\ \left[\begin{array}{ccc} 0.85 & 0.05 & 0.10 \\ 0.75 & 0.10 & 0.15 \\ 0.65 & 0.15 & 0.20 \\ \hdashline 0.60 & 0.10 & 0.30 \\ 0.55 & 0.10 & 0.35 \\ 0.45 & 0.05 & 0.50 \\ \hdashline 0.30 & 0.15 & 0.55 \\ 0.25 & 0.10 & 0.65 \\ 0.10 & 0.05 & 0.85 \end{array}\right] \end{array}$$

with $\mu_1 = 90.0$, $\mu_2 = 105.0$, $\mu_3 = 120.0$ and $\sigma = 15.0$, where an entry of the matrix $((j, k), l)$ indicates transition probability from state k to state l following state j ($j, k, l = 1 \sim 3$); SEMI 2026, with

$$
\begin{array}{c}
 \\
(1,k) \\
 \\
 \\
 \\
 \\
 \\
 \\
(2,k) \\
 \\
 \\
 \\
 \\
 \\
 \\
(3,k) \\
 \\
 \\
 \\
 \\
 \\
 \\
(4,k) \\
 \\
 \\
 \\
 \\
 \\
 \\
(5,k) \\
 \\
 \\
 \\
 \\
 \\
 \\
(6,k) \\
 \\
 \\
 \\
 \\
 \\
 \\
\end{array}
\begin{array}{|cccccc|}
\multicolumn{6}{c}{(l)} \\
\hline
0.60 & 0.20 & 0.10 & 0.05 & 0.03 & 0.02 \\
0.55 & 0.20 & 0.10 & 0.05 & 0.05 & 0.05 \\
0.50 & 0.20 & 0.10 & 0.10 & 0.05 & 0.05 \\
0.45 & 0.25 & 0.10 & 0.10 & 0.05 & 0.05 \\
0.40 & 0.25 & 0.15 & 0.10 & 0.05 & 0.05 \\
0.35 & 0.25 & 0.15 & 0.10 & 0.10 & 0.05 \\
\hline
0.30 & 0.25 & 0.20 & 0.10 & 0.10 & 0.05 \\
0.30 & 0.25 & 0.20 & 0.10 & 0.05 & 0.10 \\
0.30 & 0.20 & 0.15 & 0.05 & 0.10 & 0.20 \\
0.25 & 0.25 & 0.20 & 0.05 & 0.10 & 0.15 \\
0.25 & 0.20 & 0.15 & 0.10 & 0.10 & 0.20 \\
0.25 & 0.20 & 0.10 & 0.10 & 0.15 & 0.20 \\
\hline
0.30 & 0.15 & 0.05 & 0.05 & 0.15 & 0.30 \\
0.30 & 0.15 & 0.05 & 0.05 & 0.15 & 0.30 \\
0.25 & 0.15 & 0.10 & 0.10 & 0.15 & 0.25 \\
0.25 & 0.15 & 0.10 & 0.10 & 0.15 & 0.25 \\
0.20 & 0.15 & 0.15 & 0.15 & 0.15 & 0.20 \\
0.20 & 0.15 & 0.15 & 0.15 & 0.15 & 0.20 \\
\hline
0.20 & 0.15 & 0.15 & 0.15 & 0.15 & 0.20 \\
0.20 & 0.15 & 0.15 & 0.15 & 0.15 & 0.20 \\
0.25 & 0.15 & 0.10 & 0.10 & 0.15 & 0.25 \\
0.25 & 0.15 & 0.10 & 0.10 & 0.15 & 0.25 \\
0.30 & 0.15 & 0.05 & 0.05 & 0.15 & 0.30 \\
0.30 & 0.15 & 0.05 & 0.05 & 0.15 & 0.30 \\
\hline
0.20 & 0.15 & 0.10 & 0.10 & 0.20 & 0.25 \\
0.20 & 0.10 & 0.10 & 0.15 & 0.20 & 0.25 \\
0.15 & 0.10 & 0.05 & 0.20 & 0.25 & 0.25 \\
0.20 & 0.10 & 0.05 & 0.15 & 0.20 & 0.30 \\
0.10 & 0.05 & 0.10 & 0.20 & 0.25 & 0.30 \\
0.05 & 0.10 & 0.10 & 0.20 & 0.25 & 0.30 \\
\hline
0.05 & 0.10 & 0.10 & 0.15 & 0.25 & 0.35 \\
0.05 & 0.05 & 0.10 & 0.15 & 0.25 & 0.40 \\
0.05 & 0.05 & 0.10 & 0.10 & 0.25 & 0.45 \\
0.05 & 0.05 & 0.10 & 0.10 & 0.20 & 0.50 \\
0.05 & 0.05 & 0.05 & 0.10 & 0.20 & 0.55 \\
0.02 & 0.03 & 0.05 & 0.10 & 0.20 & 0.60 \\
\hline
\end{array}
$$

with $\mu_1=90.0, \mu_2=105.0, \mu_3=120.0, \mu_4=135.0, \mu_5=150.0, \mu_6=165.0$, and $\sigma=15.0$.

Appendix 5

Relation Between the Number of Times of the Shuffling and Significance Level. Let $y_1, y_2 \ldots, y_n$ be random samples of $\Delta\hat{D}_m^{\mathrm{sh}}$, and p_i be the probability of class i, where

$$\sum_{i-1}^{r} p_i = 1 .$$

The probability that the maximum value of $y_1, y_2, \ldots, y_n$ falls into class k is as follows:

$$\gamma = P\left(\max_{1 \leqq j \leqq n} y_j = k\right) = n\left(\sum_{i=1}^{k-1} p_i\right)^{n-1} p_k \tag{79}$$

We put

$$\sum_{i=1}^{k-1} p_i = 1 - \alpha, \qquad 0 < \alpha \ll 1 ,$$

and assume

$$p_{k+j-1} = \beta^j \qquad (j = 1, 2, \ldots).$$

Then

$$\alpha = \sum_{j-1}^{\infty} p_{k+j-1} = \frac{\beta}{1-\beta},$$

and

$$p_k = \beta - \frac{\alpha}{1+\alpha}.$$

Accordingly from Equation (79)

$$\gamma = n(1-\alpha)^{n-1}\frac{\alpha}{1+\alpha}. \tag{80}$$

We obtain n which gives maximum value of γ. Let n be the continuous variable. Then

$$\frac{d\gamma}{dn} = \{(1-\alpha)^{n-1} + n(1-\alpha)^{n-1}\ln(1-\alpha)\}\frac{\alpha}{1+\alpha} = 0 .$$

Accordingly

$$\ln(1-\alpha) = -\frac{1}{n}. \tag{81}$$

From Equation (81)

$$n \approx \frac{1}{\alpha}. \tag{82}$$

In this case the maximum value of γ is as follows:

$$\gamma = \frac{(1-\alpha)^{1/\alpha}}{1-\alpha^2} \tag{83}$$

For example when $\alpha = 0.01$,

$$\gamma \approx 0.373 .$$

That is, γ is relatively large in value. This suggests that the maximum value of $\Delta\hat{D}_m^{\mathrm{sh}}$ is approximately regarded as a critical value for significance level $\alpha = 1/n$ when the shuffling is made n times.

Appendix 6

Proof of $\hat{D}_m \downarrow D_m$ *and* $\bar{\bar{D}}_m^{\mathrm{sh}} \downarrow D_{m-1}$. We prove the following equations:

$$\hat{D}_1 \downarrow D_1 \qquad (N \to \infty), \tag{84}$$

and

$$\bar{\bar{D}}_1^{\mathrm{sh}} \downarrow D_0 = 0 \qquad (N \to \infty). \tag{85}$$

We sample interval sequences of size N from the population and calculate

$$\hat{H}_0 = -\sum_{i=1}^{n_s} \frac{N_i}{N}\log_2\frac{N_i}{N} \tag{86}$$

for each sequence, where N_i is frequency of state i. Then the arithmetic mean of $\hat{H}_0$ is the estimate of $E(\hat{H}_0)$. Let $p(i)$ be the probability of state i in the population. Since

$$E(N_i/N) = p(i)$$

and

$$\frac{N_i}{N} \to p(i) \qquad (N \to \infty, \text{ in prob}),$$

$$\hat{H}_0 \to -\sum_{i-1}^{n_s} p(i)\log_2 p(i)$$

$$= H_0 \qquad (N \to \infty, \text{ in prob}). \tag{87}$$

That is, $\hat{H}_0$ is the consistent estimate of H_0.

The following equation holds:

$$E(\hat{H}_0)=E\left\{-\sum_{i=1}^{n_s}\frac{N_i}{N}\log_2\frac{N_i}{N}\right\}$$
$$=\frac{1}{\ln 2}\sum_{i=1}^{n_s}E\left\{\sum_{k=1}^{\infty}\frac{1}{k}\frac{N_i}{N}\left(1-\frac{N_i}{N}\right)^k\right\}$$
$$=\frac{1}{\ln 2}\sum_{i=1}^{n_s}\sum_{k=1}^{\infty}\frac{1}{k}\left\{\frac{1}{N^k}E(N-N_i)^k-\frac{1}{N^{k+1}}E(N-N_i)^{k+1}\right\}.$$

Let $M(\Theta)$ be moment generating function of $N-N_i$. Then

$$M(\Theta)=E\{e^{\Theta(N-N_i)}\}$$
$$=\sum_{N_i=0}^{N}e^{\Theta(N-N_i)}\binom{N}{N_i}p_i^{N_i}(1-p_i)^{N-N_i}$$
$$=\sum_{N_i=0}^{N}\binom{N}{N_i}(1-q(i))^{N_i}\{q(i)e^{\Theta}\}^{N-N_i}$$
$$=[1-q(i)+q(i)e^{\Theta}]^N,$$

where

$$q(i)=1-p(i)=p(1)+\ldots+p(i-1)+p(i+1)+\ldots+p(n_s)$$
$$<1.$$

Since $E[(N-N_i)^k]=M^{(k)}(0)$,

$$E(\hat{H}_0)=\frac{1}{\ln 2}\sum_{i=1}^{n_s}\left\{\frac{M^{(1)}(0)}{N}-\sum_{k=2}^{\infty}\frac{M^{(k)}(0)}{k(k-1)N^k}\right\},$$

where

$$M^{(k)}(0)=\left.\frac{d^kM(\Theta)}{d\Theta^k}\right|_{\Theta=0}.$$

Then

$$E(\hat{H}_0)=\frac{1}{\ln 2}\left[\sum_{i=1}^{n_s}\left(q(i)-\tfrac{1}{2}q^2(i)-\tfrac{1}{6}q^3(i)-\ldots-\frac{1}{k(k-1)}q^k(i)\ldots\right)\right.$$
$$\left.-\frac{1}{N}\frac{n_s-1}{2}-O\left(\frac{1}{N}\right)\right]. \tag{88}$$

On the other hand,

$$H_0=-\sum_{i-1}^{n_s}p(i)\log_2 p(i)$$
$$=\frac{1}{\ln 2}\sum_{i=1}^{n_s}(1-q(i))\sum_{k}^{\infty}\frac{q^k(i)}{k}$$
$$=\frac{1}{\ln 2}\sum_{i=1}^{n_s}\left(q(i)-\tfrac{1}{2}q^2(i)-\tfrac{1}{6}q^3(i)\ldots-\frac{1}{k(k-1)}q^k(i)\ldots\right).$$

Accordingly

$$E(\hat{H}_0)=H_0-\frac{1}{N}A_0-O\left(\frac{1}{N}\right), \tag{89}$$

where $A_0=(n_s-1)/2$.

We consider estimating conditional entropy

$$H_1=-\sum_{i,j=1}^{n_s}p(i,j)\log_2 p_i(j) \tag{90}$$

by

$$\hat{H}_1=-\sum_{i,j=1}^{n_s}\frac{N_{ij}}{N}\log_2\frac{N_{ij}}{N_i}. \tag{91}$$

Here $p(i,j)$ is joint probability of the combination of state (i,j), $p_i(j)$ is conditional probability of state j following state i, and N_{ij} is frequency of the state (i,j) in sample sequence of size N. Then N_{ij}/N, N_{ij}/N_i, and N_i/N are the consistent estimate of $p(i,j)$, $p_i(j)$, and $p(i)$, respectively. Accordingly Equation (91) is the consistent estimate of Equation (90):

$$\hat{H}_1\to H_1 \quad (N\to\infty, \text{ in prob}). \tag{92}$$

The expected value of $\hat{H}_1$ is expressed by the following equation in the same way as in the case of $E(\hat{H}_0)$:

$$E(\hat{H}_1)=H_1-\frac{1}{N}A_1-O\left(\frac{1}{N}\right), \tag{93}$$

where $A_1=(n_s^2-n_s)/2$.

Let $\bar{\hat{H}}_0$ and $\bar{\hat{H}}_1$ be the arithmetic mean of $\hat{H}_0$ and $\hat{H}_1$, respectively. When $N\to\infty$,

$$\bar{\hat{H}}_0=E(\hat{H}_0),$$
$$\bar{\hat{H}}_1=E(\hat{H}_1),$$

and

$$\bar{\hat{D}}_1=\left(\frac{\overline{\hat{H}_0-\hat{H}_1}}{\hat{H}_0}\right)\approx\frac{\bar{\hat{H}}_0-\bar{\hat{H}}_1}{\bar{\hat{H}}_0}. \tag{94}$$

Then

$$\bar{\hat{D}}_1\approx\frac{E(\hat{H}_0)-E(\hat{H}_1)}{E(\hat{H}_0)}$$
$$=\frac{H_0-H_1+\frac{1}{N}(A_1-A_0)}{H_0-\frac{1}{N}A_0}\downarrow\frac{H_0-H_1}{H_0}=D_1. \tag{95}$$

That is, $\bar{\hat{D}}_1$ decreases monotonically to D_1 when $N\to\infty$. Equation (95) indicates that the bias of $\hat{D}_1$ is determined by N, H_0 and n_s. Then Equation (84) is proved. When $N\to\infty$,

$$\bar{\hat{D}}_1^{\mathrm{sh}}=\left(\frac{\overline{\hat{H}_0-\hat{H}_1^{\mathrm{sh}}}}{\hat{H}_0}\right)$$
$$\approx\frac{\bar{\hat{H}}_0-\bar{\hat{H}}_1^{\mathrm{sh}}}{\bar{\hat{H}}_0},$$

where $\bar{H}_1^{\mathrm{sh}}$ is the arithmetic mean of $\hat{H}_1^{\mathrm{sh}}$ when the shuffling is made finite times for sample sequence of size N, and $\bar{\hat{H}}_1^{\mathrm{sh}}$ is that of $\bar{H}_1^{\mathrm{sh}}$ calculated from sample sequences. When $N\to\infty$,

$$\bar{\hat{H}}_1^{\mathrm{sh}}=E(\bar{H}_1^{\mathrm{sh}})=E(\hat{H}_1^{\mathrm{sh}}).$$

The expected value of $\hat{H}_1^{\mathrm{sh}}$ is expressed by the following equation similar to Equation (92):

$$E(\hat{H}_1^{\mathrm{sh}})=H_1^{\mathrm{sh}}-\frac{1}{N}A_1-O\left(\frac{1}{N}\right).$$

From our definition of the shuffling,

$$H_1^{\mathrm{sh}}=H_0.$$

Then

$$\bar{\hat{D}}_1^{\mathrm{sh}}=\frac{H_0-\frac{1}{N}A_0-\left(H_0-\frac{1}{N}A_1\right)}{H_0-\frac{1}{N}A_0}\downarrow 0,$$

when $N\to\infty$. Accordingly Equation (85) is proved.

It is similarly proved that $\bar{D}_m\downarrow D_m$ and $\bar{\hat{D}}_m^{\mathrm{sh}}\downarrow D_{m-1}$ when $N\to\infty$.

Appendix 7

Proof of $|\hat{S}_{m+1}^{\mathrm{sh}}|=|\hat{S}_m|\left(1-\frac{\chi_m^2}{N}\right)$. When we substitute $y_1, y_2, \ldots$ and y_m for $\hat{\varrho}_1^{\mathrm{sh}}, \hat{\varrho}_2^{\mathrm{sh}}, \ldots$, and $\hat{\varrho}_m^{\mathrm{sh}}$, respectively, In Equation (46),

$$|\hat{S}_{m+1}^{\mathrm{sh}}|=\begin{vmatrix}1 & y_1 & \cdots & & y_{m-1} & y_m\\ y_1 & 1 & \varrho_1 & \cdots & \varrho_{m-2} & \varrho_{m-1}\\ \vdots & \varrho_1 & & & \vdots & \vdots\\ \vdots & \vdots & & & \vdots & \varrho_1\\ y_m & \varrho_{m-1} & \cdots & & \varrho_1 & 1\end{vmatrix}. \tag{96}$$

Here $\varrho_1, \varrho_2, ..., \varrho_{m-1}$ are known, when these values are calculated from the original sequence of sufficiently large sample size.

From the vector series given by Equation (23), x^{sh}_{t-m} and $(x_{t-m+1}, ..., x_t)$ are independent with each other. Then

$$E(y_i)=0, \tag{97}$$

$$E[(x^{sh}_{t-m}-\bar{x})^2]=\sigma^2, \tag{98}$$

and

$$\begin{aligned} E(y_iy_j)&=\frac{1}{(N-m)^2}\frac{1}{\sigma^4}\sum_{t=m+1}^{N}E[(x^{sh}_{t-m}-\bar{x})^2(x_{t-m+i}-\bar{x})(x_{t-m+j}-\bar{x})] \\ &=\frac{1}{(N-m)^2}\frac{1}{\sigma^2}\sum_{t=m+1}^{N}(x_{t-m+i}-\bar{x})(x_{t-m+j}-\bar{x}) \\ &=\frac{1}{N-m}\varrho_{|i-j|}\approx\frac{1}{N}\varrho_{|i-j|}, \end{aligned} \tag{99}$$

if N is large.

Let S'_{ij} be a cofactor of the element (i,j) in

$$|\hat{S}_m|=\begin{vmatrix} 1 & \varrho_1 & \cdots & \varrho_{m-1} \\ \varrho_1 & 1 & \cdots & \varrho_{m-2} \\ \vdots & \vdots & & \vdots \\ \varrho_{m-1} & \varrho_{m-2} & \cdots & 1 \end{vmatrix}. \tag{100}$$

Then

$$|\hat{S}^{sh}_{m+1}|=|\hat{S}_m|-\sum_{i,j=1}^{m}S'_{ij}y_iy_j. \tag{101}$$

On the other hand, from Equation (99) the variance-covariance matrix of $(y_1, y_2, ..., y_m)$ is as follows:

$$\left(\frac{1}{N}\varrho_{|i-j|}\right)=\frac{1}{N}(\hat{S}_m). \tag{102}$$

The inverse matrix of Equation (102) is

$$\left(\frac{1}{N}\varrho_{|i-j|}\right)^{-1}=N(\hat{S}_m)^{-1}=N\left(\frac{S'_{ij}}{|\hat{S}_m|}\right)=N(\hat{S}^{ij}_m), \tag{103}$$

where $\hat{S}^{ij}_m=\dfrac{S'_{ij}}{|\hat{S}_m|}$, (i,j) element of inverse matrix of $(\hat{S}_m)$.

When we substitute $|\hat{S}_m|\hat{S}^{ij}_m$ for S'_{ij} in Equation (101), we obtain the following equation:

$$|\hat{S}^{sh}_{m+1}|=|\hat{S}_m|\left(1-\frac{1}{N}\sum_{i,j=1}^{m}N\hat{S}^{ij}_m y_iy_j\right). \tag{104}$$

We consider the distribution of the quadratic form of matrix $(N\hat{S}^{ij}_m)$ in Equation (104):

$$\chi^2_m=\sum_{i,j=1}^{m}N\hat{S}^{ij}_m y_iy_j. \tag{105}$$

$(y_1, y_2, ..., y_m)$ is a vector random variable having m-variate normal distribution, and the mean and the variance-covariance matrix are given by Equations (97) and (102), respectively.

Then Equation (105) has the chi-square distribution with m degrees of freedom (Wilks, 1962):

$$|\hat{S}^{sh}_{m+1}|=|\hat{S}_m|\left(1-\frac{\chi^2_m}{N}\right). \tag{106}$$

Appendix 8

Proof of Independence of m from the Distribution of $\Delta\hat{\mathcal{Q}}^{sh}_m$. From Equations (43), (44), (104), and (105),

$$\begin{aligned} \Delta\hat{\mathcal{Q}}^{sh}_m&=\tfrac{1}{2}\{\log_2|\hat{S}^{sh}_m|-\log_2|\hat{S}^{sh}_{m+1}|\}-\tfrac{1}{2}\{\log_2|\hat{S}_{m-1}|-\log_2|\hat{S}_m|\} \\ &=\tfrac{1}{2}\left[\log_2\left(1-\frac{\chi^2_{m-1}}{N}\right)-\log_2\left(1-\frac{\chi^2_m}{N}\right)\right], \end{aligned} \tag{107}$$

where

$$\chi^2_m=\sum_{i,j=1}^{m}N\hat{S}^{ij}_m y_iy_j.$$

Since $E(\chi^2_m)=m$ and $\mathrm{var}(\chi^2_m)=2m$, when $N\gg m$,

$$\Delta\hat{\mathcal{Q}}^{sh}_m\approx\frac{\log_2 e}{2}\cdot W_m,$$

where

$$W_m=\sum_{i,j=1}^{m}\hat{S}^{ij}_m y_iy_j-\sum_{i,j=1}^{m-1}\hat{S}^{ij}_{m-1}y_iy_j. \tag{108}$$

Then moment generation function of W_m is as follows:

$$E\{e^{\Theta W_m}\}=\int_{-\infty}^{\infty}\cdots\int_{-\infty}^{\infty}e^{\Theta W_m}f(y_1, ..., y_m)dy_1...dy_m, \tag{109}$$

where

$$f(y_1, ..., y_m)=\frac{\sqrt{|N\hat{S}^{ij}_m|}}{\sqrt{(2\pi)^m}}\exp\left(-\tfrac{1}{2}\sum_{i,j=1}^{m}N\hat{S}^{ij}_m y_iy_j\right). \tag{110}$$

Then

$$\begin{aligned} E\{e^{\Theta W_m}\}=\frac{\sqrt{|N\hat{S}^{ij}_m|}}{\sqrt{(2\pi)^m}}\int_{-\infty}^{\infty}\cdots\int_{-\infty}^{\infty}\exp\Bigg\{&-\left(\frac{N}{2}-\Theta\right)\sum_{i,j=1}^{m}\hat{S}^{ij}_m y_iy_j \\ &-\Theta\sum_{i,j=1}^{m-1}\hat{S}^{ij}_{m-1}y_iy_j\Bigg\}dy_1...dy_m. \end{aligned}$$

Here

$$\begin{aligned} \sum_{i,j=1}^{m}\hat{S}^{ij}_m y_iy_j&=\hat{S}^{mm}_m\left(y_m+\sum_{i=1}^{m-1}\frac{\hat{S}^{mi}_m}{\hat{S}^{mm}_m}y_i\right)^2+\sum_{i,j=1}^{m-1}\left(\hat{S}^{ij}_m-\frac{\hat{S}^{mi}_m\hat{S}^{mj}_m}{\hat{S}^{mm}_m}\right)y_iy_j \\ &=\hat{S}^{mm}_m\left(y_m+\sum_{i=1}^{m-1}\frac{\hat{S}^{mi}_m}{\hat{S}^{mm}_m}y_i\right)^2+\sum_{i,j=1}^{m-1}\hat{S}^{ij}_{m-1}y_iy_j. \end{aligned} \tag{111}$$

The 2nd term of Equation (111) is derived as follows:
We put

$$B_{ij}=\hat{S}^{ij}_m-\frac{\hat{S}^{mi}_m\hat{S}^{mj}_m}{\hat{S}^{mm}_m}.$$

Then

$$\begin{aligned} B_{ij}&=\frac{1}{\hat{S}^{mm}_m}\begin{vmatrix}\hat{S}^{ij}_m & \hat{S}^{im}_m \\ \hat{S}^{mj}_m & \hat{S}^{mm}_m\end{vmatrix} \\ &=\frac{1}{\hat{S}^{mm}_m|\hat{S}_m|^2}\cdot T_{ij}, \end{aligned}$$

where

$$T_{ij}=\begin{vmatrix}\hat{S}'_{ij} & \hat{S}'_{im} \\ \hat{S}'_{mj} & \hat{S}'_{mm}\end{vmatrix}.$$

Here $\hat{S}'_{ij}$ means the cofactor of $\hat{S}_{ij}$ in the determinant $|\hat{S}_m|$. Then T_{ij} is the 2nd order minor of reciprocal determinant of $|\hat{S}_m|$. When $m\geqq 3$, according to Jacobi's theorem,

$$\begin{aligned} T_{ij}&=|\hat{S}_m|(-1)^{i+m+j+m}\hat{S}_m\binom{im}{jm} \\ &=|\hat{S}_m|(-1)^{i+j}\hat{S}_{m-1}\binom{i}{j} \\ &=|\hat{S}_m||\hat{S}_{m-1}|\hat{S}^{ij}_{m-1}, \end{aligned}$$

where $\hat{S}_m\binom{im}{jm}$ is the $(m-2)$th order minor of $|\hat{S}_m|$ in which the i-th and m-th rows of $|\hat{S}_m|$, and the j-th and m-th columns of $|\hat{S}_m|$ are removed; $\hat{S}_{m-1}\binom{i}{j}$ is the $(m-2)$th order minor of $|\hat{S}_{m-1}|$ in which the i-th row

and j-th column of $|\hat{S}_{m-1}|$ are removed; and $(-1)^{i+j}\hat{S}_{m-1}\begin{pmatrix} i \\ j \end{pmatrix}$ is the cofactor of (i,j) element in the determinant $|\hat{S}_{m-1}|$. Then

$B_{ij}=\hat{S}^{ij}_{m-1}$.

Accordingly

$$E\{e^{\Theta W_m}\}=\frac{\sqrt{|N\hat{S}^{ij}_m|}}{\sqrt{(2\pi)^m}}\int_{-\infty}^{\infty}\cdots\int_{-\infty}^{\infty}\exp\left(-\tfrac{1}{2}\sum_{i,j=1}^{m-1}N\hat{S}^{ij}_{m-1}y_iy_j\right)dy_1\ldots dy_{m-1}$$
$$\cdot\int_{-\infty}^{\infty}\exp\left\{-\frac{(N-2\Theta)\hat{S}^{mm}_m}{2}\left(y_m+\sum_{i=1}^{m-1}\frac{\hat{S}^{mi}_m}{\hat{S}^{mm}_m}y_i\right)^2\right\}dy_m$$
$$=\frac{\sqrt{|N\hat{S}^{ij}_m|}}{\sqrt{(2\pi)^m}}\frac{\sqrt{(2\pi)^{m-1}}}{\sqrt{|N\hat{S}^{ij}_{m-1}|}}\sqrt{\frac{2\pi}{(N-2\Theta)\hat{S}^{mm}_m}}.$$

where

$$|N\hat{S}^{ij}_m|=\frac{N^m}{|\hat{S}_m|}.$$

Then

$$E\{e^{\Theta W_m}\}=\left(1-\frac{2\Theta}{N}\right)^{-\frac{1}{2}}. \tag{112}$$

When $m=2$, Equation (112) is also derived directly from Equation (109). Then

$$E(W_m)=\frac{1}{N}\quad\text{and}\quad\operatorname{var}(W_m)=\frac{2}{N^2}. \tag{113}$$

Equation (113) indicates that the distribution of W_m has the same distribution of $\frac{1}{N}\chi^2_1$. That is, if we neglect the higher terms of $1/N$ in Equation (107), the distribution of $\Delta\hat{D}^{\mathrm{sh}}_m$ has the same distribution of of $\Delta\hat{D}^{\mathrm{sh}}_1$ for all m.

Acknowledgements. Much of this work was suggested by Professor Masami Ogawara of Tokyo Woman's Chistian University, to whom we owe thanks for his constant guidance and help in theoretical proof. We are also indebted to Associate Professor Tsuneo Yamamoto and Mr. Fujio Tange of Computer Center, University of Tokyo for the use of computer facilities.

This study was supported by a Grant-in-Aid for Scientific Research (Grant No. 189004; and Grant No. 110202, Specified Category, 1976) from the Ministry of Education, Science and Culture, Japan.

References

Cox, D. R., Lewis, P. A. W.: The statistical analysis of series of events. New York: Wiley 1966

Cramér, H.: Mathematical methods of statistics. Princeton, N. J.: Princeton Univ. Press 1963

Fano, R. M.: Transmission of information. A statistical theory of communications. Massachusetts: MIT Press 1961

Nakahama, H.: Relation of mean impulse frequency to statistical dependency between intervals in neuronal impulse sequences. J. Neurophysiol. **29**, 935—941 (1966)

Nakahama, H., Ishii, N., Yamamoto, M.: Markov process of maintained impulse activity in central single neurons. Kybernetik **11**, 61—72 (1972)

Nakahama, H., Ishii, N., Yamamoto, M., Fujii, H.: Statistical inference of Markov process of neuronal impulse sequences. Kybernetik **15**, 47—64 (1974)

Nakahama, H., Ishii, N., Yamamoto, M., Fujii, H., Obata, T.: Statistical dependency as a measure to evaluate Markov properties of stochastic point processes. Biol. Cybernetics **18**, 191—208 (1975a)

Nakahama, H., Ishii, N., Yamamoto, M., Saito, H.: Stochastic properties of spontaneous impulse activity in central single neurons. Tohoku J. exp. Med. **104**, 373—409 (1971)

Nakahama, H., Nishioka, S.: Statistical dependency between intervals in neuronal impulse sequences. J. theor. Biol. **12**, 140—146 (1966)

Nakahama, H., Nishioka, S., Otsuka, T., Aikawa, S.: Statistical dependency between interspike intervals of spontaneous activity in thalamic lemniscal neurons. J. Neurophysiol. **29**, 921—934 (1966)

Nakahama, H., Yamamoto, M., Ishii, N., Sato, T., Fujii, H., Obata, T.: Markov properties of spike trains recorded from central single neurons. In: Proceedings of the 8th International Biometric Conference, pp. 219—228. Corsten, L. C. A., Postelnicu, T. (Eds.) Bucuresti: Editura Academiei Republicii Socialiste România 1975b

Naylor, T. H., Balintfy, J. L., Burdick, D. S., Chu, K.: Computer simulation techniques. New York: Wiley 1967

Papoulis, A.: Probability, random variables, and stochastic processes. New York: McGraw-Hill 1965

Perkel, D. H., Gerstein, G. L., Moore, G. P.: Neuronal spike trains and stochastic point processes. 1. The single spike train. Biophys. J. **7**, 391—418 (1967)

Shannon, C., Weaver, W.: The mathematical theory of communication. Urbana: Univ. of Illinois Press 1949

Wilks, S. S.: Mathematical statistics. New York: Wiley 1962

Wold, H.: On stationary point processes and Markov chain. Skand. Aktuar. **31**, 229—240 (1948)

Yanaru, T., Nakahara, J.: Computer simulation of Markov processes of inter-point intervals and their statistical properties. Bull. Kyushu Inst. Tech. **29**, 125—132 (1974)

Received: September 27, 1976

Prof. Hiroshi Nakahama
Division of Neurophysiology
Institute of Brain Diseases
Tohoku University School of Medicine
5-13-1, Nagamachi, Sendai, Japan

Biol. Cybernetics 25, 227–240 (1977)

Biological Cybernetics

The Modelling of a Burst-Generating Neuron with a Field-Effect Transistor Analog

R. M. Gulrajani, F. A. Roberge, and P. A. Mathieu

Biomedical Engineering Group, Department of Physiology, Faculty of Medicine, University of Montreal, Montreal, Canada

Abstract. An electronic analog that models the burst generating neuron R_{15} of the *Aplysia* abdominal ganglion is described. The analog is based on the four branch Hodgkin-Huxley equivalent circuit for a patch of squid axon membrane, with a choice of parameter values appropriate to the *Aplysia* cell membrane. To realize the slow subthreshold oscillations seen in cell R_{15} upon exposure to the drug tetrodotoxin (TTX), it was necessary to include two additional conductance branches, g'_{Na} and g'_{K}, to the basic Hodgkin-Huxley circuit. Without these, the analog was capable of generating only action potentials and hence termed the "suprathreshold" analog. With all six branches operative, bursts very similar to those seen in R_{15} were realized, and subsequent inhibition of the Hodgkin-Huxley sodium conductance g_{Na} resulted in the desired subthreshold oscillations. The electronic circuitry and the performance of the "suprathreshold" and complete analog are described. An explanation is offered for the progressive widening of the action potentials within a burst seen in R_{15}. The analog also simulates the phenomenon of potassium ion accumulation outside the cell membrane during a burst, using a local feedback loop to reduce the potassium equilibrium potential in a manner roughly proportional to the logarithm of the time integral of the outward potassium current. Some consequences of this effect are also discussed.

Introduction

The central nervous system of invertebrates has long been used for the study of single neurons. One of the most common preparations is the abdominal ganglion of the marine mollusc *Aplysia californica*. A limited number of neurons in this ganglion have been identified by Frazier et al. (1967) according to their position, size and pigmentation (Fig. 1a). These identified cells have been classified into four groups according to their usual pattern of activity. Silent cells (e.g., cells R_2, L_1), which discharge action potentials only upon stimulation. "Beating" pacemaker cells (e.g., cells $R_3 - R_8$) which generate action potentials spontaneously at a more-or-less regular rate and with a firing frequency in the range $0.5 - 2$ per second. Irregular pacemaker cells (e.g., cells L_7, L_8) which are generally beating pacemaker neurons whose steady rhythm is modulated in an irregular fashion by synaptic inputs from other cells in the ganglion. And finally "bursting" cells (e.g., cells R_{15}, $L_2 - L_4$, L_6) which display a firing pattern characterized by clusters of spikes separated by periods of hyperpolarization (Fig. 1b).

These various forms of spontaneous activity make the abdominal ganglion of *Aplysia* ideal for the investigation of the mechanisms of "beating" and "bursting" activity. In particular the bursting cells R_{15}, $L_2 - L_4$, L_6 have been extensively studied. A typical experiment involves dissecting the abdominal ganglion from the animal, and pinning it on a resin layer, in a bath which is perfused with artificial seawater. The bursting cell is then penetrated with two *KC 1*-filled glass microelectrodes, one for recording the internal cell membrane potential, the other to permit the passage of intracellular current for stimulation purposes. The change in firing activity in response to changes in the perfusing solution can also be studied. One such experiment involved the substitution of artificial seawater with seawater containing the drug tetrodotoxin (TTX). This substance is known to block action potentials in biological cells, by inhibiting the early transient increase in the cell membrane sodium conductance that triggers an action potential (Moore and Narahashi, 1967). Moreover the drug seems to be highly selective in that it blocks just this one ionic channel, leaving the other ionic pathways relatively intact. When the bursting cell was exposed to TTX, as expected all action potential activity eventually disappeared (Strumwasser, 1968; Mathieu and Roberge, 1971). However the cell

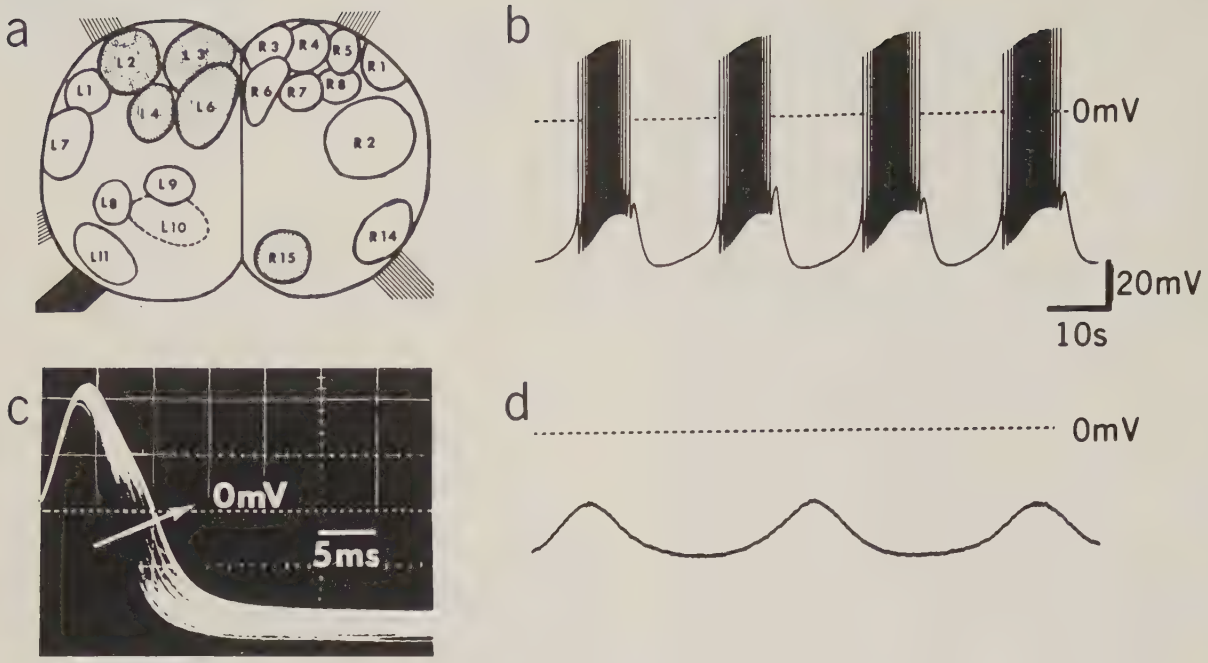

Fig. 1a—d. Some characteristics of the *Aplysia* bursting cell R_{15}. **a** Diagram showing the identified neurons on the dorsal side of the abdominal ganglion; bursting neurons are shown shaded. **b** Tracing of the bursting discharge of cell R_{15}. **c** Photograph of a typical burst discharge in R_{15} in which the action potentials have been superposed to show the progressive increase in action potential duration as the burst develops. **d** Slow wave oscillations unmasked by tetrodotoxin (TTX) in R_{15}

continued to exhibit its cycles of depolarization and hyperpolarization (Fig. 1d). Clearly these slow membrane potential oscillations are behind the cell's burst firing pattern in normal seawater.

Once the independent existence of these slow oscillations was demonstrated, the question naturally arose as to the ionic mechanisms responsible for their generation. Junge and Stephens (1973) demonstrated that an increase in membrane conductance, primarily to K^+ ions, is responsible for the hyperpolarizing phase of the slow wave. Using the voltage clamp technique, it was found that two slow current components are activated during the slow wave: an initial inward current due to Na^+ ions followed by a progressively increasing outward current due to K^+ ions (Gola, 1974; Carnevale, 1974; Smith et al., 1975). Thus it would appear that slow cyclic variations in two distinct membrane conductances are responsible for the slow oscillations. The depolarizing phase is due to an increase in a sodium conductance and is accompanied by an inward flow of Na^+ ions, the hyperpolarizing phase is due to a subsequent increase in a potassium conductance with an outward flow of K^+ ions. These slow conductance variations are of course in addition to the fast sodium and potassium conductance transients that are responsible for action potential generation.

Although the principal features of the bursting mechanism are known, viz., that bursting is due to an underlying slow oscillation which triggers action potentials during its depolarizing phase, and that this slow oscillation is itself due to cyclic variations in a sodium and a potassium conductance, several points remain to be elucidated. For instance, it has been observed that during a burst the frequency of firing first increases and then decreases (Fig. 1b). Is this effect consistent with the assumed bursting model of a slow oscillation triggering action potentials? And what, in turn, is the effect of the action potentials during a burst on the slow oscillations? What are the most likely explanations for the changes in waveform of successive action potentials within a burst (Fig. 1c)? Although final conclusive answers to these questions must await the results of more biological experiments, considerable additional insight into the burst mechanism can be gained by constructing an electronic analog of the bursting cell. Based on the information summarized above, the analog must consist of fast sodium and potassium channels to generate action potentials along with two additional, and much slower, conductance channels for generating the slow oscillations. If the assumptions underlying bursting are correct, the performance of this electronic analog should closely approximate the real bursting cell. In addition, "electronic" experiments involving changes in analog parameters can be easily performed to suggest both possible answers to the questions raised, as well as biological experiments to verify these possible answers. A similar approach, but employing digital simulation, has recently been described by Both et al. (1976).

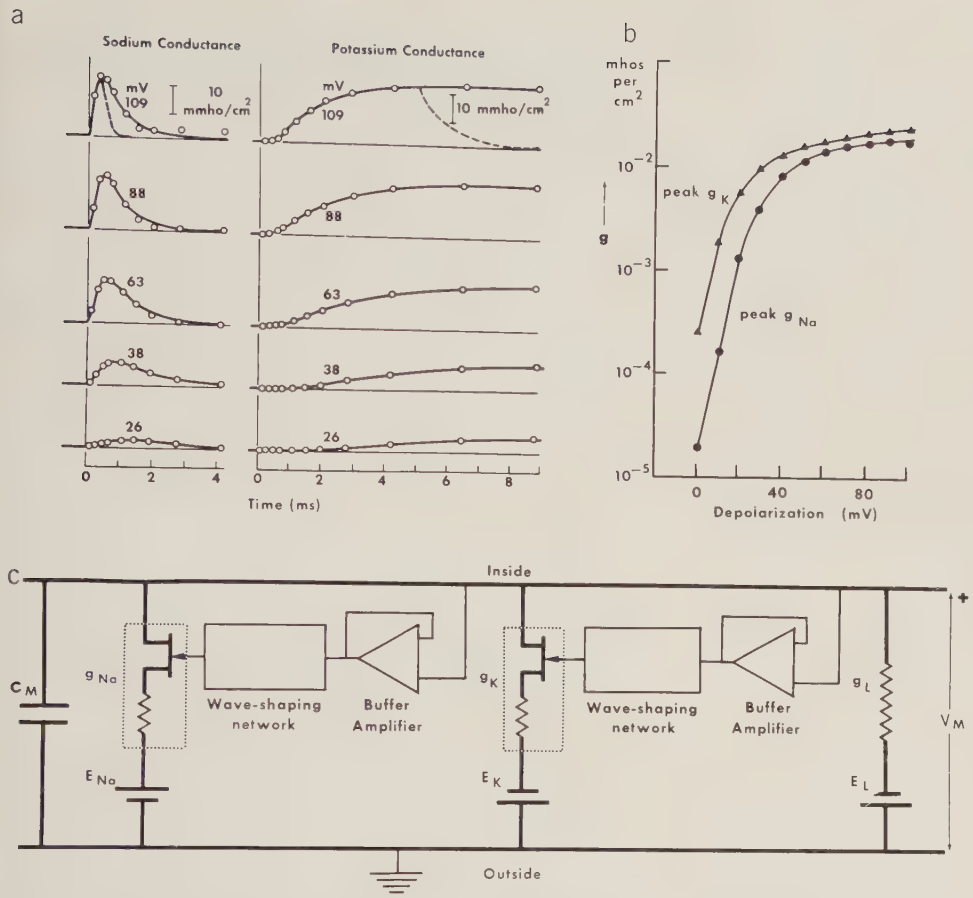

Fig. 2a—c. Conductance characteristics of the squid axon membrane and their simulation with field-effect transistors. **a** Sodium and potassium conductance transients for various clamp voltages. **b** Peak sodium and potassium conductance variation with depolarization (after Hodgkin and Huxley, 1952a, b, c). **c** Field-effect transistor analog of the squid axon membrane (after Gulrajani and Roberge, 1976)

Modelling Technique

The FET Analog for the Squid Axon Membrane

An electronic analog for a patch of squid axon membrane, employing field-effect transistors (FETs) to simulate the sodium and potassium ionic conductances has recently been described (Gulrajani and Roberge, 1976). A brief summary of the technique is given below as the analog constructed to model the *Aplysia* bursting cell also utilizes FETs to simulate the various ionic conductances.

The squid axon membrane has been characterized by a four-branch electrical equivalent circuit (Hodgkin and Huxley, 1952d). These four branches represent the membrane capacitance C_M, the conductance of the membrane to sodium ions (g_{Na}), the conductance to potassium ions (g_K) and a lumped membrane conductance to all other ions besides Na^+ and K^+ (g_L). The ionic conductances are each placed in series with an electromotive source whose magnitude equals the Nernst equilibrium potential for the respective ion species: E_{Na}, E_K, E_L. Using the voltage clamp technique, Hodgkin and Huxley (1952a, b, c) found that depolarization caused an "activation" or increase in both g_{Na} and g_K, with the g_{Na} increase being only temporary (Fig. 2a). The peak g_{Na} and g_K values reached varied with the amount of depolarization (Fig. 2b). The g_{Na} and g_K transients of Fig. 2a may be characterized by their "rise" times and "fall" times, the second being the time for the conductance to reach its resting value when the applied depolarization is removed (the dotted transient in Fig. 2a). In addition, the g_{Na} transient is characterized by an "inactivation" time constant which governs the decay of g_{Na} with maintained depolarization and a "recovery-from-inactivation" time constant that governs the rate of removal of the effects of this decay once the depolarization is removed. Also both the sodium and potassium rise times and the sodium inactivation time vary with the level of applied depolarization. The rapid initial depolarization that characterizes an action potential is due to a corresponding increase in g_{Na} (and a concomitant inward flux of Na^+ ions). This is followed by an increase in g_K (and an outward flux of K^+ ions)

that results in the repolarizing phase of the action potential.

The modelling of the squid axon membrane involved using a junction FET and resistor in series to simulate the variable sodium and potassium conductances (Fig. 2c). Since the drain-source conductance of a FET is controlled by the voltage applied to the gate terminal, the dependence of g_{Na} and g_K on membrane depolarization (Fig. 2b) was realized by feeding back the simulated membrane potential, V_M, to this terminal. An accurate match required a careful selection of FET, series resistor, feedback gain, as well as the size of the membrane patch to be simulated (Gulrajani and Roberge, 1976). The correct transients in g_{Na} and g_K were realized by interposing a waveshaping network in the feedback loop. Correct adjustment of this network was done empirically such that for a step change in V_M the waveform at the gate resulted in the desired conductance transients. The action potentials generated by the four-branch FET analog were found to be remarkably similar in form to those observed in the real squid axon membrane.

Development of the FET Analog for the Aplysia bursting cell

Clearly if it is desired to model the *Aplysia* bursting cell with a FET analog, the first step is to obtain the magnitudes of the membrane parameters for this preparation. This entails knowing the approximate values of each of the elements in the equivalent circuit, the variations in g_{Na} and g_K with depolarization, and the magnitudes of the rise times, fall times, inactivation and recovery-from-inactivation times of the conductance transients. Again some of these time parameters may vary with depolarization levels. Furthermore two additional branches, the slow sodium and slow potassium conductances, g'_{Na} and g'_K, have to be included to completely characterize the bursting cell. The selection of these parameters based on the available experimental data, and the development of the final electronic analog of the bursting cell are described below.

This development took place in two steps and will be described as such. Initially a classic four-branch Hodgkin-Huxley equivalent circuit was constructed, i.e., the conductance branches g'_{Na} and g'_K responsible for the slow subthreshold oscillations were omitted. We refer to this circuit as the "suprathreshold" analog and its description and performance are given together below. The suprathreshold analog may be considered to model either a silent or a beating pacemaker cell, as it can be transformed from one to the other. In the second phase the subthreshold conductance branches g'_{Na} and g'_K were added, to yield the complete FET analog of the bursting cell. The construction of these subthreshold branches and the performance of the complete analog are described next. A discussion of the results obtained concludes the paper.

The Suprathreshold Analog

Parameter Estimation

Kunze and Brown (1971) used liquid ion exchanger microelectrodes to measure the potassium and chloride activities in certain *Aplysia* cells, in order to obtain values of the equilibrium potentials E_K and E_{Cl}. Using their results as a guide and assuming that E_L may be set equal to E_{Cl}, we select $E_K = -75\,\text{mV}$ and $E_L = -55\,\text{mV}$. With the same technique, Russell and Brown (1972) estimated the sodium equilibrium potential E_{Na} as $76 \pm 5\,\text{mV}$. However voltage clamp studies on R_2 (Geduldig and Gruener, 1970) have indicated that the inward current reverses at a membrane potential of approximately $+55\,\text{mV}$ and that the contribution of calcium ions to this inward current is small. Thus it was deemed preferable to use $E_{Na} = +55\,\text{mV}$.

The specific membrane capacitance was chosen as $1\,\mu\text{F/cm}^2$. This figure corresponds to experimental measurements on the *Anisodoris nobilis G* cell, a somewhat similar type of invertebrate neuron (Gorman and Mirolli, 1972). It may be noted also that this value of membrane capacitance is being increasingly accepted as a standard for the biological membrane, both on the basis of actual measurements as well as the range of values to be expected from a consideration of the physical dimensions and chemical structure of biological membranes (Cole, 1968; Jack et al., 1975).

To estimate g_L we refer to observations made by Carpenter (1970) on the cell R_2. He estimated the total resistance of R_2 as about $10^6\,\Omega$. Next, considering R_2 to be a sphere of diameter $600\,\mu$ with membrane infoldings sufficient to increase the apparent surface area by a factor of 10, he calculated the surface area of the cell to be approximately $0.1\,\text{cm}^2$. This yields a value of $10^{-5}\,\text{mhos/cm}^2$ for the specific membrane conductance at rest, viz. $(g_L + g_{Na}\,\text{rest} + g_K\,\text{rest}) = 10^{-5}\,\text{mhos/cm}^2$. It is reasonable to assume that most of the membrane conductance in the resting state is due to g_L. Therefore we select $g_L = 9 \times 10^{-6}\,\text{mhos/cm}^2$ and $(g_{Na}\,\text{rest} + g_K\,\text{rest}) = 10^{-6}\,\text{mhos/cm}^2$.

The next step was to estimate the variation in peak g_{Na} and peak g_K with depolarization. These were calculated from published current-voltage curves (Geduldig and Gruener, 1970; Eaton, 1972). The peak g_{Na} and peak g_K curves are plotted in Figure 3. These curves must be considered to be very rough estimates, since to obtain them considerable extrapolation of clamp currents and guessing of cell size and surface in

the published experiments cited were necessary. They are scaled to represent the peak conductances of 5 mm^2 of *Aplysia* membrane, the size of the membrane patch simulated by the analog. For comparison purposes, superposed on the curves are the measured peak g_{Na} and peak g_K data points obtained via voltage clamp tests on the completed suprathreshold analog.

Initial estimates of the magnitude of the time constants governing the g_{Na} and g_K transients were also obtained using some of the results published by Geduldig and Gruener (1970) and Eaton (1972). Slight adjustments of these time parameters were eventually required to bring the action potential waveforms of the suprathreshold analog into good correspondence with those seen in *Aplysia* cells.

Potassium Accumulation and Potassium Inactivation

Eaton (1972) has convincingly demonstrated the phenomenon of potassium accumulation in cell R_{15}. He found that in this cell the outward potassium current (I_K) during voltage clamp, decayed to a steady state value appreciably less than the peak I_K reached. This drop in I_K can result from either an inactivation in g_K or a reduction in the magnitude of E_K. While Eaton could not rule out g_K inactivation entirely, he did show that a considerable reduction in the magnitude of E_K occurred with an ongoing I_K outflow. For example, with a maintained depolarization of +55 mV he obtained an E_K shift from −70 mV to −30 mV in approximately 2 seconds. Thus it would seem that the outward flowing potassium ions tend to accumulate in pockets just outside the cell membrane, thereby temporarily augmenting the extracellular potassium ion concentration, and consequently reducing E_K.

The progressive reduction in action potential undershoot during a burst (Fig. 1b) could very well be due to such an E_K shift with potassium current outflow. This effect was incorporated in the suprathreshold analog by means of a local feedback loop which approximately realizes the function $\Delta E_K \sim \ln\left|\int_0^t I_K dt\right|$. This equation assumes that the extracellular potassium concentration is proportional to the time integral of the outward potassium current.

It was also decided to include a small amount of g_K inactivation in the suprathreshold analog, partly because there is a possibility that the effect is present in *Aplysia* cells and partly to verify whether cumulative g_K inactivation could be held responsible for action potential widening during a burst (Fig. 1c). The amount of g_K inactivation, and the magnitudes of the time constants for g_K inactivation and recovery-from-inactivation, were left adjustable for lack of precise information.

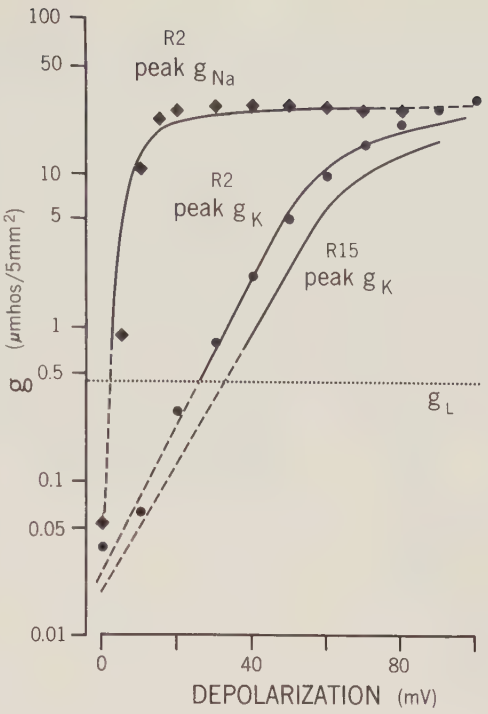

Fig. 3. Curves depicting peak sodium and potassium conductance values in cells R_2 and R_{15}. The dotted portions were obtained after extrapolation of the original voltage clamp results (Geduldig and Gruener, 1970; Eaton, 1972). Data points are results obtained with the suprathreshold analog

Simulation of Peak g_{Na} and Peak g_K Curves with FETs

The total conductance, g, of a FET in series with a resistor R (Fig. 4, inset) is given by $g = g_{DS}/(1 + Rg_{DS})$ where g_{DS} is the drain-source conductance of the FET. For a sufficiently large negative gate bias, one has $g_{DS} \ll (1/R)$ and hence $g \simeq g_{DS}$. As the gate bias is made less negative, ultimately $g_{DS} \gg (1/R)$ and consequently $g \lesssim (1/R)$. Thus the total conductance saturates at this value. This variation of g with gate bias V_G is illustrated in Figure 4.

Now if a characteristic such as that of peak g_K against depolarization (Fig. 3) has to be matched, in which the curve just begins to exhibit saturation, a careful selection of FET and series resistor has to be made. This is because the total conductance of the series arrangement remains equal to $g_{DS}/(1 + Rg_{DS})$ and cannot be approximated by the limiting value $(1/R)$. Accordingly, R must be selected to be appreciably less than $1/(g_K \text{ max})$. On the other hand if the peak g_{Na} against depolarization characteristic has to be realized, where an appreciable degree of saturation is exhibited, one can simply select $R = 1/(g_{Na} \text{ max})$ and make sure that the condition $g_{DS} \gg (1/R)$ is satisfied by driving the gate sufficiently towards zero for large depolarizations. This procedure has one drawback however, for while the simulated conductance saturates at the correct

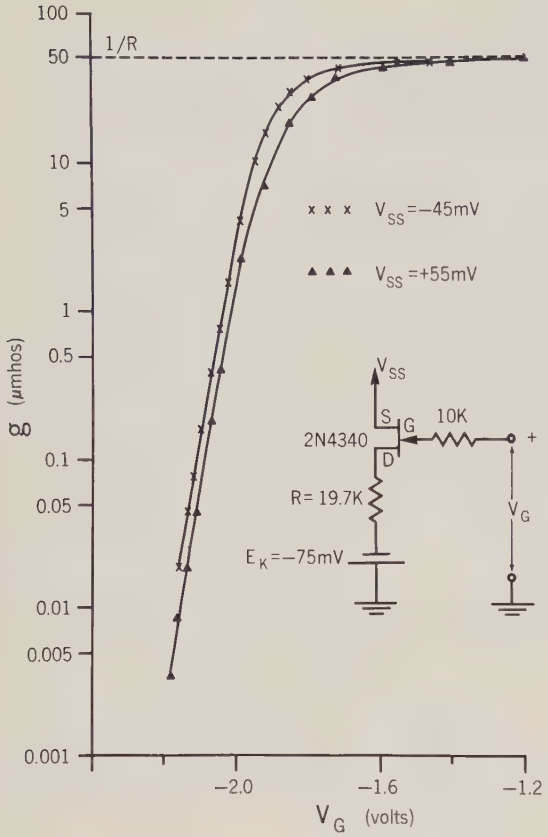

Fig. 4. Conductance variation with V_G of the FET-series resistor combination (inset) used to simulate g_K, for two different values of source potential V_{SS}

value with increasing depolarization, the input to the waveshaping network does not (Fig. 2c). Thus the transients in g_{Na} keep changing even though the peak g_{Na} value remains constant. It was therefore necessary in the case of g_{Na} simulation, as will be described in the next section, to include a limiter amplifier before the wave-shaping network that also saturated at the same level of depolarization as the peak sodium conductance.

Circuit Description

The complete schematic of the g_{Na} simulation network is shown in Figure 5. The limiter amplifier A_2 follows the initial buffer amplifier A_1. The potentiometer marked "Na gain" is adjusted so that A_2 limits at −10 V (approximately the breakdown voltage of the 1 N 758 A Zener diode D_1), for a depolarization of approximately 30 mV from rest. The gain of the final operational amplifier in the feedback loop (A_4) is fixed so that when A_2 limits, the condition $g_{DS} \gg (1/R)$ holds and consequently, the peak g_{Na} reached is approximately equal to $(1/R)$. To simulate TTX blockage of the sodium conductance the normally closed switch "g_{Na} block" is opened, thereby drastically reducing the gain of the operational amplifier A_4. The feedback capacitor across A_4 determines the sodium rise time. The charging rate of the 20 μF capacitor through the SV 100 A varistor and MPS 6522 transistor determines the inactivation time constant. This charging rate increases with increasing depolarization (as long as A_2 does not limit), thereby decreasing the inactivation time. The fall time, inactivation time and recovery-from-inactivation time of the sodium conductance may be varied by changing the appropriate potentiometer settings as marked in Figure 5. The resting value of g_{Na} is varied by adjusting the potentiometer "FET bias". A resting potential of −45 mV was selected as being most representative of *Aplysia* cells, and the resting values of g_{Na} and g_K are set to yield this resting potential for the analog.

Correct adjustment of the g_{Na} circuit is done by clamping the simulated *Aplysia* membrane to its assumed resting potential of −45 mV and subjecting it to depolarizing steps. The g_{Na} transients are visualized by monitoring the sodium current (as the voltage across the 31.9 K resistor), and the various time parameters may then be appropriately adjusted. Furthermore the peak values of g_{Na} should correspond with the desired values of Figure 3.

The schematic of the g_K circuit is shown in Figure 6. In this case A_2 is connected simply to provide additional gain and does not limit. The potassium rise and fall times are adjustable by changing the settings of the potentiometers so marked. Partial inactivation to a steady state value is provided by the elements between A_3 and A_4. There is no dependence of the inactivation rate on the level of depolarization. As before the potentiometer marked "FET bias" sets the resting value of g_K. Adjustment is done via voltage clamp tests with the switch "E_K shift" open (no E_K shift due to accumulation). The variation of g_K is observed at point I_K, after a hundred-fold amplification of the potassium current waveform. The potentiometers marked "gain", "rise time", and "steady state conductance" are adjusted simultaneously to realize both the correct peak g_K values (Fig. 3) as well as the appropriate g_K transients.

Closing the switch "E_K shift" will result in E_K shifts with the outward potassium current. Here A_9 integrates the potassium current; its output is then fed to the logarithmic amplifier A_{10}. The output of the latter has a non-adjustable slope of approximately 60 mV per decade change in input voltage, and is temperature dependent. However, the variations in slope are slight following an initial warmup period of a half hour, and as such they do not materially affect the results. The output of A_{10} is applied to the FET-series resistor combination via A_{11}. The quiescent value of E_K (−75 mV) is also set through A_{11}. An increase in I_K will

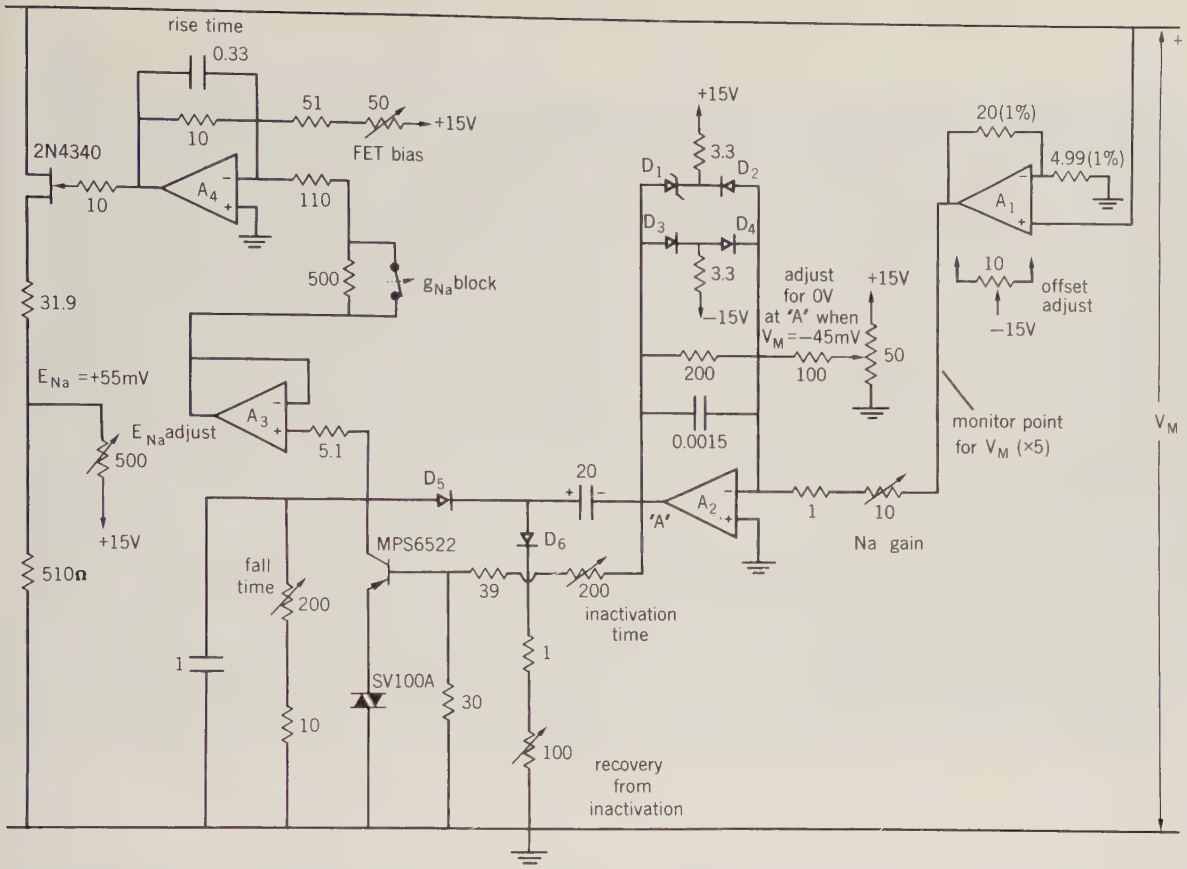

Fig. 5. Circuit diagram for the simulation of g_{Na} (suprathreshold analog). Amplifiers A_1 and A_3 are of type LH 0042 C, A_2 and A_4 of type 741 C. Diode D_1 is type 1 N 758 A, $D_2 - D_6$ are type 1 N 4454. The SV 100 A varistor is supplied by Victory Engineering Corporation, Springfield, New Jersey. Component values are in $k\Omega$ and μF unless otherwise indicated

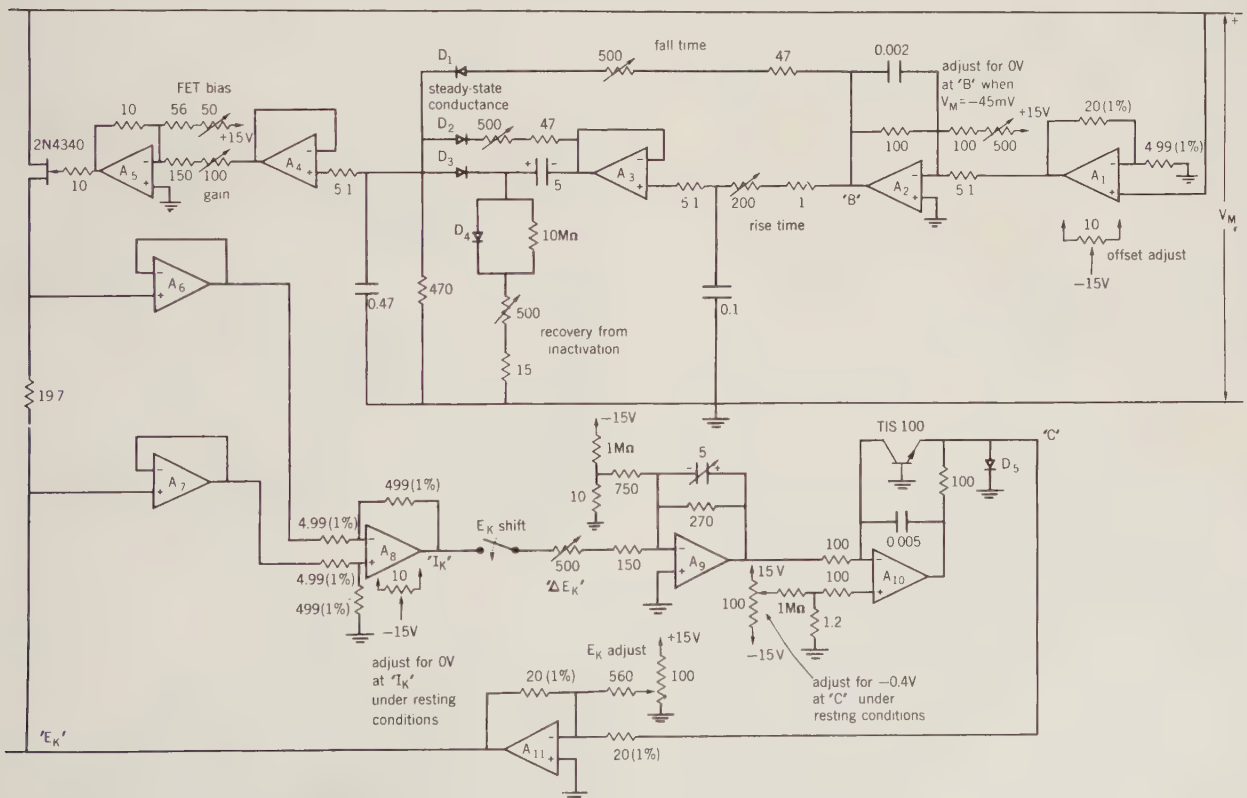

Fig. 6. Circuit diagram for the simulation of g_K (suprathreshold analog). Amplifiers A_2, A_3, A_5, A_8, A_9, and A_{11} are type 741 C. Amplifiers A_1, A_4, A_6, A_7, and A_{10} are type LH 0042 C. All diodes are type 1 N 4454. As before, component values are in kΩ and μF unless otherwise indicated

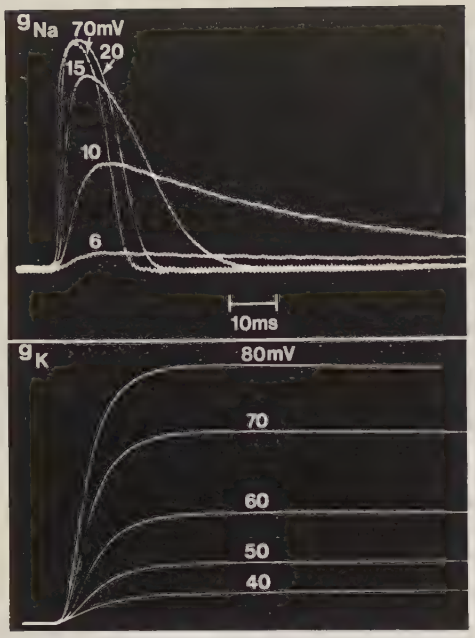

Fig. 7. Photographs of the suprathreshold g_{Na} and g_K transients for the depolarization steps indicated

change this quiescent value by an amount roughly proportional to the logarithm of the integral of I_K, as desired. The time constant of the E_K shift may be varied by changing the 5 μF integrating capacitor, and its magnitude by varying the potentiometer marked "ΔE_K". These parameters were usually set to obtain Eaton's (1972) observation of a 40 mV E_K shift in approximately 2 s, following a maintained depolarization of 55 mV.

Performance

The g_{Na} and g_K circuits (Figs. 5 and 6) in parallel with a capacitance C_M of 0.05 μF and a leakage branch comprising $g_L = 0.45$ μmhos and $E_L = -55$ mV constituted the suprathreshold analog. The resting sodium and potassium conductances were selected to be close to the extrapolated values of the conductance curves of Figure 3, and at the same time result in a resting potential of −45 mV for a silent analog. As mentioned earlier, the suprathreshold analog could be transformed into a beating pacemaker by appropriately adjusting certain circuit parameters. In the previous simulation study of the squid axon membrane (Gulrajani and Roberge, 1976), the condition for spontaneous pacemaker activity was that the potassium fall time had to exceed the sodium recovery-from-inactivation time. In this way, a recovering (decreasing) potassium conductance following an action potential would result in a slow depolarization, which would in turn trigger another action potential provided sodium recovery was

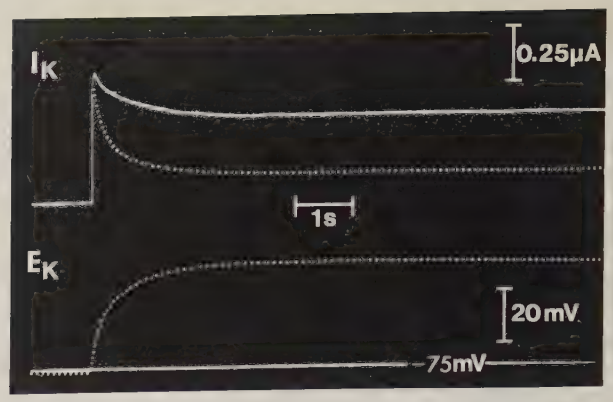

Fig. 8. Waveforms of the I_K and E_K transients with the E_K shift circuitry disabled (solid trace) and operative (dotted trace)

complete. With the present analog, the intrinsic mechanism responsible for spontaneous action potentials was again verified to be an interaction between sodium recovery-from-inactivation and potassium fall times; spontaneous activity was obtained by decreasing the former or increasing the latter. However, in this case, it was not possible to establish precisely the relative magnitudes of the two parameters at which pacemaker activity commenced. As before, factors such as a low resting g_{Na}, or too large a value for E_K, could inhibit spontaneous action potential generation, even with a favourable ratio between sodium recovery and potassium fall times.

The match with the desired peak g_{Na} and peak g_K curves has been described (Fig. 3). No significance should be attached to the fact that the data points for the analog follow the peak g_K curve for the silent cell R_2 rather than the bursting cell R_{15}, as once again it must be stressed that the derived g_{Na} and g_K curves are, at best, rough estimates of the conductance variations in *Aplysia*. The data points shown in Figure 3 were obtained by means of voltage clamp tests on the suprathreshold analog with the potassium accumulation circuit disabled. Photographs of the g_{Na} and g_K transients are shown in Figure 7. The decrease in the time constant of sodium inactivation, τ_h, with increasing membrane depolarization is evident upon examination of the g_{Na} transients of Figure 7. This decrease ceases when the value of peak g_{Na} saturates, i.e., for depolarizations greater than 30 mV from rest. No variation of potassium rise time with depolarization is present in the g_K curves.

The slow inactivation of g_K is not very evident at the fast sweep speed of Figure 7. The phenomenon is better visualized in Figure 8, taken at a much slower sweep speed, where the potassium clamp current I_K (as opposed to g_K) is depicted, both with the E_K shift circuitry working and disabled. In the latter condition the I_K and g_K transients are proportional to one

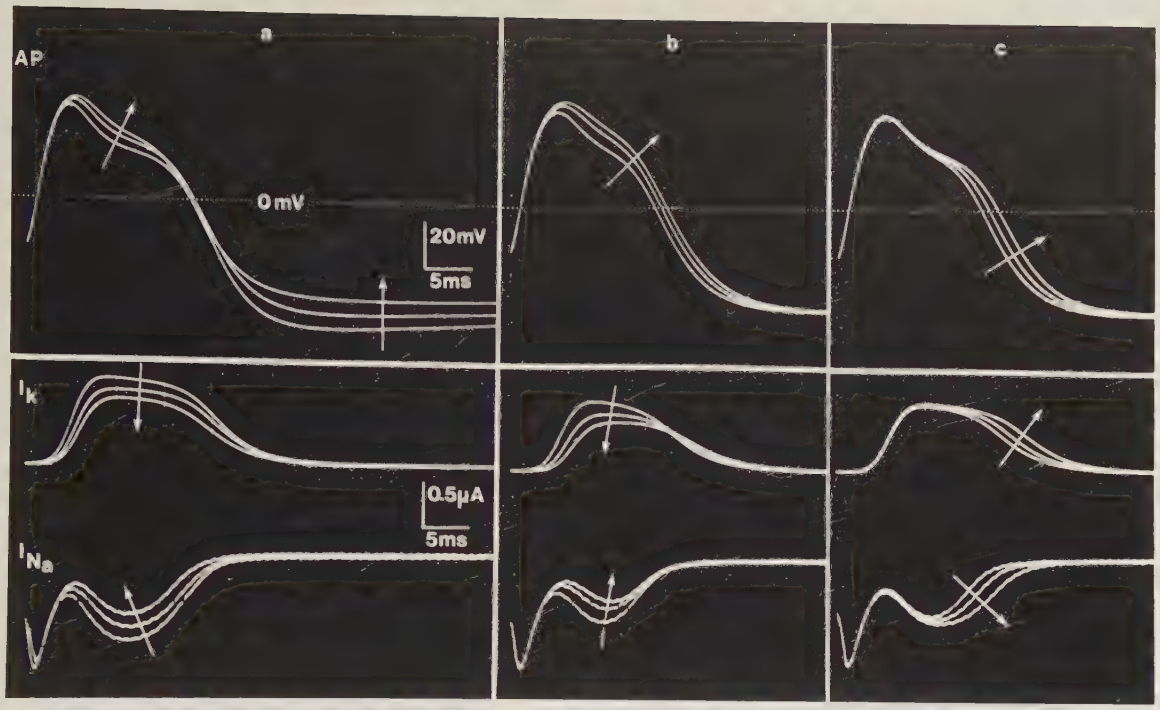

Fig. 9a—c. Variations in action potential waveform (AP), I_K and I_{Na} of the suprathreshold analog when **a** E_K is reduced **b** g_K is diminished and **c** τ_h is increased. In each case the arrows indicate the direction of change

another, and the I_K transient clearly demonstrates g_K inactivation to a steady state value ($g_K ss$). With the E_K shift circuitry active, the same depolarization of 55 mV is seen to reduce I_K appreciably due to an E_K shift of 38 mV. Now because of these ongoing E_K shifts, the I_K transient is no longer proportional to g_K. It was found that the additional I_K reduction in this case was greater than could be attributed to the diminution in E_K, i.e., a further reduction in $g_K ss$ was present. This meant a second order effect of a changing E_K value on the simulated potassium conductance, and was traced to the slight variation in FET conductance with changes in V_{SS}, in spite of V_G being held constant (Fig. 4). Another point is the shape of the E_K shift transient (Fig. 8) which is not sigmoidal as obtained experimentally in cell R_{15} by Eaton (1972). However Palti et al. (1974) have published theoretical curves of such E_K shift transients that do have the more exponential shape obtained via the suprathreshold analog. This is not surprising since they employed the same basic scheme used here, viz., $\Delta E_K \sim \ln\left|\int_0^t I_K dt\right|$, with the only modification being that the effect of K^+ ions being removed from the extracellular space by diffusion and electric forces was also taken into account. Thus it appears that the underlying assumptions behind this formula may have to be modified to obtain Eaton's *S*-shaped E_K shift curves.

Finally the effect of varying certain parameters on the action potential waveform was investigated (Fig. 9). Here the changes in the action potential waveform of a spontaneously active analog, in response to parameter changes, were photographed, along with the changes in I_K and I_{Na}. In (a) E_K is reduced, thus leading to a reduction in the action potential undershoot and a slight widening probably due to the reduced potassium current. In (b) the potassium recovery-from-inactivation time was progressively increased. As the frequency of action potential generation remained unchanged this resulted in a progressively diminished available potassium conductance. Again widening of the action potential is noted. Widening very similar to that observed during a burst in R_{15} (Fig. 1c) is seen to occur when the sodium inactivation time is increased (Fig. 9c). This will be discussed further at a later stage.

The Subthreshold Conductance Branches

Accurate estimates of the Hodgkin-Huxley parameters of the subthreshold conductance branches are hampered by the lack of precise quantitative voltage clamp data. Very little is known either about the absolute values of g'_{Na} and g'_K or their variation with depolarization. They are, however, one or two orders of magnitude smaller than the maximum values of the corresponding suprathreshold conductances. Gola (1974) states that in cell R_{15} neither g'_{Na} nor g'_K inactivate and gives approximate values for the time constants governing their kinetics. These are approximately 1 s

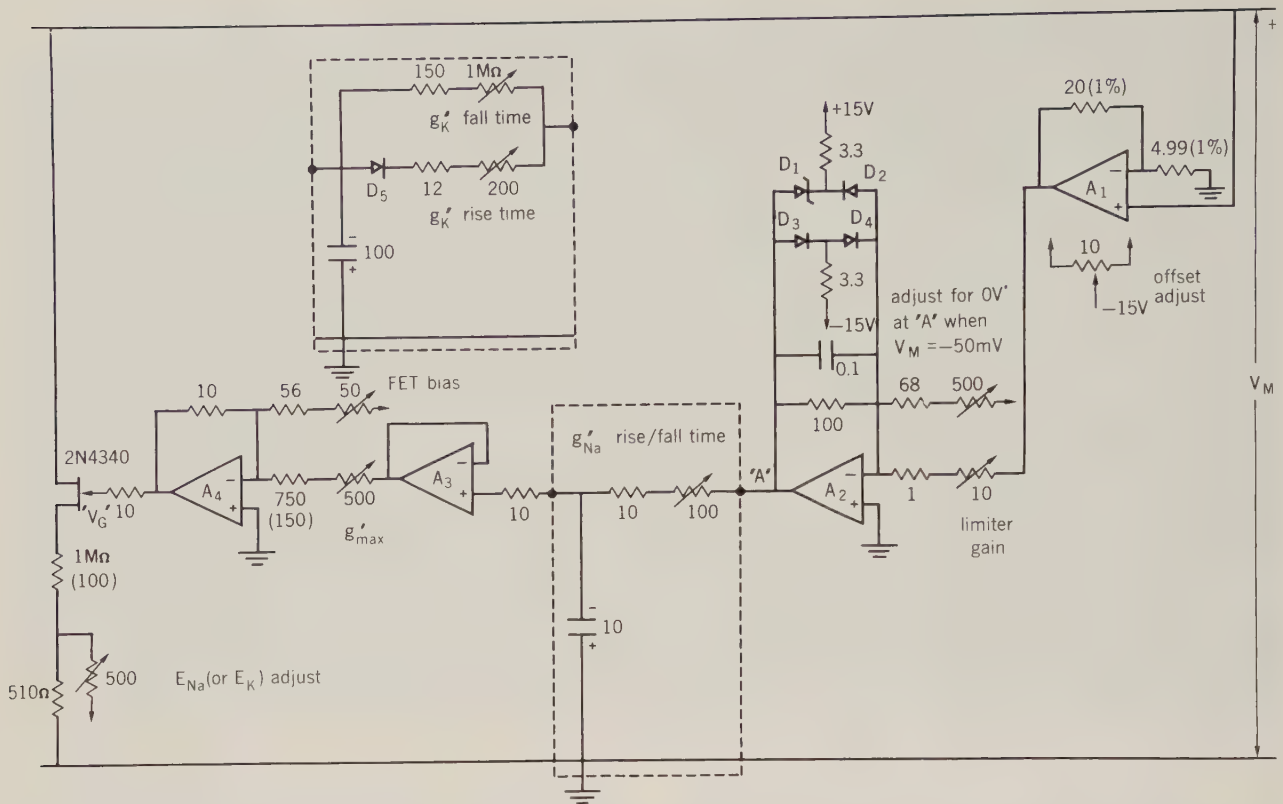

Fig. 10. Circuit diagram for the simulation of g'_{Na}. Amplifiers A_1 and A_3 are of type LH 0042 C, A_2 and A_4 of type 741 C. Diode D_1 is type 1 N 753 A, $D_2 - D_5$ type 1 N 4454. All component values are in kΩ and μF unless otherwise indicated. For g'_K simulation use circuit values in parentheses and the appropriate g'_K wave-shaping network (inset)

for the sodium rise and fall times, 3–4 s for the potassium rise time and 10–20 s for the potassium fall time.

The lack of detailed information prompted consideration of a design technique that would permit of easy adjustment of both the slopes of the g'_{Na} and g'_K characteristics, as well as their limiting values upon depolarization. Hitherto the resistor in series with the FET was always selected to yield a predetermined limiting value of conductance. In this case it was chosen so as to result in a limiting value for the conductance much larger than anticipated. Conductance curves similar to those of Figure 4 were plotted. For g'_{Na} the curve saturated at 1 μmho ($R = 1\,M\Omega$), for g'_K at 10 μmho ($R = 100\,K\Omega$). Next the output of the amplifier A_2, placed before the wave-shaping network (Fig. 10), is set to limit (at the breakdown voltage of the Zener diode) for sufficiently large membrane depolarizations. The membrane depolarization at which its output limits is controlled by the potentiometer marked "limiter gain". Thus the voltage applied to the FET gate (V_G) also limits, its limiting value being controlled mainly by the potentiometer marked "g' max". This limiting value of V_G sets the limiting values of g'_{Na} and g'_K, as the gate is never driven sufficiently towards zero so as to reach the saturation limits set by the series resistors. Generally the limiting values of g'_{Na} and g'_K were in the range 0.1 − 0.4 μmhos and 1 − 6 μmhos respectively and thus at least an order of magnitude less than the maximum values attained by the corresponding suprathreshold branches (Fig. 3). The "resting conductances" of g'_{Na} and g'_K, if such a term can be used for a continuously oscillating membrane, are set by clamping the analog to − 50 mV and adjusting the potentiometer marked "FET bias". They were usually set in the range 0.01 − 0.1 μmhos for both g'_{Na} and g'_K. While the initial slope of the g'_{Na} and g'_K against depolarization curves varies with the settings of both "limiter gain" and "g' max" potentiometers, the value of membrane depolarization at which the curves saturate depends only on the former. Adjustments of these potentiometers were made empirically so as to result in bursts that resembled those seen in *Aplysia*. In general, oscillatory activity could be suppressed by increasing the slope of the g'_K characteristic or decreasing that of the g'_{Na} characteristic. The g'_{Na} rise and fall times are varied together by the potentiometer so marked. Although controlled by the same RC circuit the fall time is always less than the rise time owing to the non-linear FET-series resistor characteristic (Fig. 4). In the g'_K wave-shaping network however (Fig. 10 inset), independent control of rise and fall times is possible.

Performance of the Complete Analog

The technique of generating bursts basically involved starting with a *beating* suprathreshold analog and adjusting the added subthreshold branches till the slow oscillations generated by the latter interacted with the spikes generated by the former to result in bursts resembling those seen in *Aplysia* cells. Under these conditions it was verified that the various subthreshold time constants and conductance values were within the ranges mentioned in the previous paragraph. The resultant bursts may be seen in Figure 11a. The frequency modulation of action potentials within a burst, as well as the variation in their undershoots, are similar to those seen in *Aplysia*. However the progressive evolution of the action potential waveform during a burst (Fig. 12) differed from that seen in the living preparation. The major difference was that the "bump" on the downward slope had a tendency to smoothen out as the simulated burst progressed, whereas it becomes more pronounced in the real bursting cell (Fig. 1c). This smoothening was due to a progressive decrease in the time for sodium inactivation caused by an increasing level of inactivation on account of the depolarizing effect of the slow oscillations. While this effect may well be present in *Aplysia* cells, it is obviously overshadowed by an increase in the sodium inactivation time due to an increase in τ_h. This parameter has been singled out because appreciable g_K inactivation, leading to a diminished and delayed potassium current I_K, while widening the action potential (Fig. 9b), does not accentuate the bump. It needs an accelerated I_K or a prolongation of I_{Na} to do this and the former would result in reduced magnitude as well as narrower action potentials. Thus the conclusion seems to be a prolongation of I_{Na} due to a progressive increase in the inactivation time constant. One hypothesis for the biological mechanism of this proposed increase is given in the discussion.

By opening the switch "g_{Na} block" (Fig. 5), TTX block of the transient increase in g_{Na} can be simulated. When this is done the underlying slow oscillations are exposed (Fig. 11b). The increase of impedance leading up to the more rapid depolarizing phase of these oscillations is demonstrated by injecting constant-current pulses into the simulated *Aplysia* membrane and noting the transients in membrane potential. A similar impedance increase was noted during the slow depolarizing phase of the oscillations uncovered in the TTX-treated cell (Mathieu, 1972). It was also observed in real *Aplysia* cells that the amplitude and period of these subthreshold oscillations increased with hyperpolarizing current injection, and decreased with depolarizing current (Mathieu and Roberge, 1971). However, in our case it was not possible to vary the simulated membrane potential appreciably in this way, without either silencing the analog in the former case or generating anomalous waveforms in the latter. This could be rectified somewhat by readjusting the subthreshold branches for larger amplitude slow oscillations, but the inevitable result was abnormal bursts when g_{Na} activation was reintroduced. Thus a degree of mismatch between supra and subthreshold channels is present in the analog.

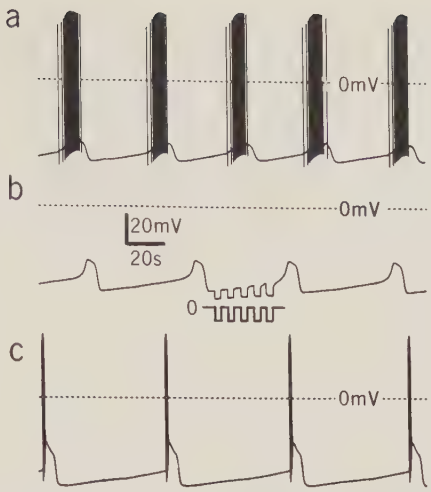

Fig. 11a—c. **a** Bursts generated by the complete analog. **b** The underlying slow oscillations, uncovered by blocking the increase in g_{Na} on opening switch "g_{Na} block" (Fig. 5). Test pulses show the relative increase in resistance during a cycle. **c** "Abnormal" bursts generated due to shifts in the potassium equilibrium potential of the g'_K branch (see text). Calibration marks apply for all traces

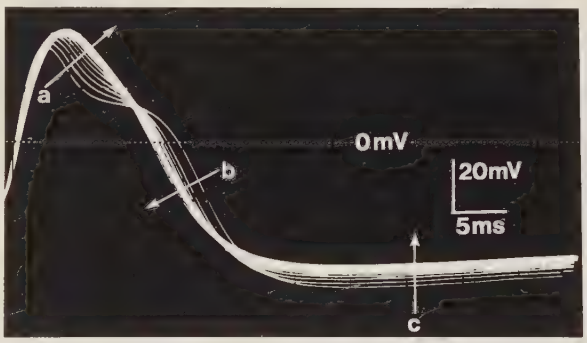

Fig. 12. Changes in action potential waveform during a burst generated by the analog. Arrows indicate changes from the start of the burst. The changes indicated by **a** are due to E_K shifts and residual g_K inactivation, by **b** due to a decrease in the time for sodium inactivation and by **c** solely due to E_K shifts

Figure 13a, b respectively show the sodium and potassium currents flowing in the subthreshold branches alone, upon application of depolarizing steps of 15 mV and 20 mV from a holding potential of −50 mV. Note the different time and amplitude scales for parts (a) and (b). The sodium current actually decreases between 15 mV and 20 mV owing to g'_{Na} having already reached its limiting value.

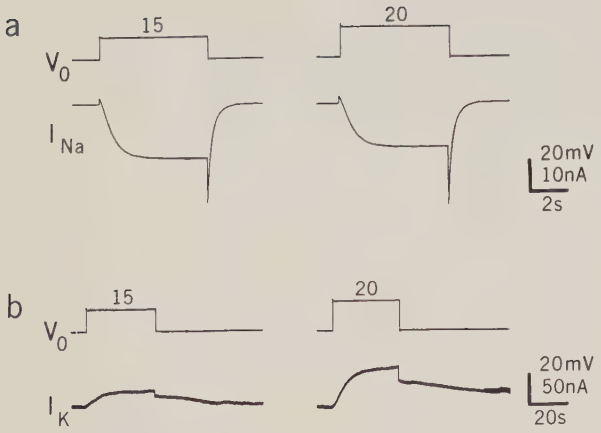

Fig. 13a and b. **a** Sodium and **b** potassium currents flowing in the subthreshold branches alone, upon application of depolarizing steps of 15 mV and 20 mV from a holding potential V_0 of −50 mV. Note different calibration marks for **a** and **b**

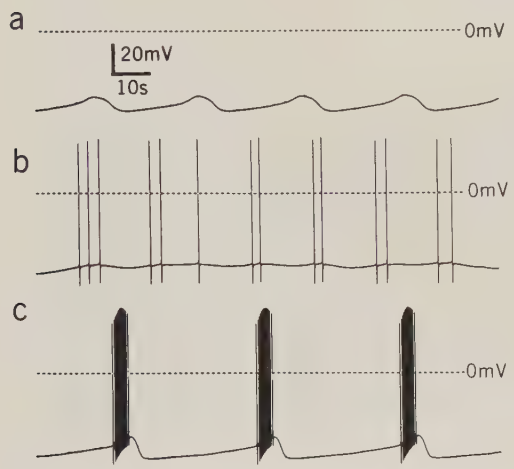

Fig. 14a—c. A fixed value of $E_K = -75$ mV for the g'_K branch yields **a** small amplitude slow oscillations and consequently **b** sparse bursts. When the potassium equilibrium potential of the g'_K circuit is replaced by the varying E_K of the g_K branch, the bursts shown in **c** are obtained (see text). Calibration marks are valid for all traces

It was also found that to get "rich" bursts (six or more action potentials per burst) it was necessary to start with a beating suprathreshold analog—i.e., with an appropriate relationship between sodium recovery and potassium fall times. As long as this condition was satisfied reasonable-sized bursts could be generated, even if initial spiking of the suprathreshold analog was inhibited by a low resting sodium conductance. On the other hand, starting with an intrinsically silent suprathreshold analog resulted in rather sparse bursts. These observations must be interpreted rather cautiously, as it could simply be another manifestation of the mismatch between supra and subthreshold channels mentioned above.

One final experiment must be mentioned. This consisted of replacing the normally constant potassium equilibrium potential of the g'_K branch with the varying E_K of the g_K branch, i.e., subjecting the subthreshold oscillations to the effect of potassium accumulation and concomitant E_K shifts that result from action potential activity. The effect was dramatic. The regular bursts of Figure 11a became immediately abnormal (Fig. 11c) due to a greatly accentuated underlying oscillation, the latter an obvious result of a diminishing E_K during the depolarizing phase. On the other hand, with a constant E_K of −75 mV for the g'_K branch, circuit parameters may be reset so as to obtain subthreshold oscillations of small amplitude (Fig. 14a) and consequently sparse bursts (Fig. 14b); in this case, replacing the constant g'_K branch potassium equilibrium potential by the varying E_K of the g_K branch can actually result in more normal bursts (Fig. 14c). Thus potassium accumulation per se, while not actually responsible for bursting activity, can under certain conditions effectively enhance it and promote its appearance. This observation is further strengthened by the hitherto "coincidental" fact that accumulation effects are noted in the bursting cell R_{15} but not in the silent cell R_2 (Alving, 1969; Eaton, 1972).

Discussion

The analog successfully demonstrates that bursts similar to those seen in *Aplysia* cells can be realized by means of a slow membrane potential oscillation triggering action potentials during its depolarizing phase. The frequency variation within a burst is a natural consequence of the mechanism of burst generation and follows the depolarizing and hyperpolarizing phases of the slow oscillation. The variation in action potential undershoots can be explained by potassium accumulation outside the cell membrane and consequent E_K shifts. Thus far the analog corroborates previously known, or suspected, characteristics of *Aplysia* bursting cells.

However on the basis of the observed performance of the analog, some new hypotheses may be put forward. First it is likely that the bursting cell is an intrinsic pacemaker, i.e., without the underlying slow oscillations, the cell would exhibit beating activity, at least within some range of membrane potential. Second, potassium accumulation outside the cell membrane, because of the accompanying E_K shifts, can enhance bursting activity. In this regard mention must be made of experimental evidence that an increase in K^+ concentration in the extracellular spaces of the cat's brain can precipitate seizures in already existing epileptogenic foci (Glaser, 1972). As is well known these epileptic seizures are often associated with bursting neuronal discharges. Finally, the widening of the action potentials during a burst is not so much due to a

cumulative inactivation of g_K as to a progressive increase in the sodium inactivation time constant, τ_h.

One way this increase in inactivation time may occur invokes the observation that calcium ions enter the cell R_{15} during an action potential (Stinnakre and Tauc, 1973). Furthermore during a burst as each successive spike widens, so does the amount of calcium ions entering per spike. The increased entry of calcium ions is a consequence of the widening rather than the other way around. If it were not so, in high external Ca^{++} solutions, one would expect a larger calcium ion influx and greater widening. In fact the reverse is seen in *Helix pomatia* (Meves, 1968), in single nodes of Ranvier (Ulbricht, 1964) and in *Aplysia* (unpublished observations by us), the action potentials becoming larger and narrower in high external Ca^{++} solutions and smaller and wider in low Ca^{++} ones. Progressive widening during a burst in Aplysia could therefore be due to a lowered local external Ca^{++} concentration as a result of the entry of calcium ions during a spike. Exactly how lowered external Ca^{++} widens an action potential is a matter of speculation. Meves (1968) explains the reduction of the overshoot and the drop in the maximum rate of rise of the action potential on the basis of theoretical permeability equations, assuming that a finite calcium permeability contributes to the action potential. We would like to suppose that, in addition, low external Ca^{++} also increases the sodium time constants, particularly the inactivation time constant τ_h. There is some evidence in single nodes of Ranvier, that the rate of recovery from inactivation at least, is slowed in low external Ca^{++} solutions (Ulbricht, 1964). This might well reflect an increase in τ_h also.

We have downplayed the cumulative inactivation of g_K as the cause of action potential widening during a burst, in favour of a projected increase in the inactivation time constant τ_h, primarily because in the model, the former did not lead to an accentuation of the bump on the downward phase. Additional supporting evidence is provided by Adelman et al. (1965) who measured an increase in τ_h associated with long duration action potentials obtained from squid axon internally perfused with low K^+ ion-containing solution. Our hypothesis, to some extent, contradicts experiments done in various preparations of the effect of the tetraethylammonium ion (TEA) on the action potential waveform. TEA selectively reduces the increase in g_K upon depolarization without affecting the increase in g_{Na}, and results in large-plateau action potentials of the cardiac type (Armstrong and Binstock, 1965), i.e., it can be said to accentuate the bump. However it does not seem to alter either the sodium or the potassium kinetics (Hille, 1967). Thus the widening under TEA does seem to argue in favour of a progressively reduced g_K as the mechanism behind action potential widening during a burst and our hypothesis of an increased τ_h should only be considered as an alternative till more concrete evidence is obtained.

It may be appropriate here to outline another hypothesis for action potential widening based on the assumption that the action potential recorded from the soma contains a contribution due to the axon spike. Evidence favouring this assumption comes from Alving's (1968) experiments on *Aplysia* pacemaker neurons where the soma spike amplitude diminished when it was isolated from the axon by ligation. Furthermore she mentions that the soma action potential shows "delayed repolarization in the falling phase", i.e., widening, when followed by the axon spike, which is the case for *Aplysia* pacemaker cells where the spike trigger zone is located in the soma. Thus progressive action potential widening during a burst may be a result of an increasing latency between soma and axon action potentials, instead of a change in soma membrane properties. This hypothesis could be tested in cell R_{15} either by recording simultaneously from the soma and axon, or by noting the change in soma action potential widening following ligation of the axon.

Finally a word is in order about the mismatch between supra and subthreshold branches that has been mentioned. This has been termed mismatch because if the subthreshold branches were adjusted for large amplitude slow oscillations, the bursts generated did not resemble those seen in R_{15}. However many varied types of bursting activity are present in biological cells (Watanabe et al., 1967; Matsumoto et al., 1969) and the bursts generated by the analog under the pronounced slow oscillation conditions did resemble some of these. Accordingly the mismatch between supra and subthreshold channels, often leading to "abnormal" or non-R_{15} like bursts, may simply reflect an improper choice of one or two analog parameters rather than a serious conceptual error in the simulation technique. If so, an analog of this type could prove of considerable value in studying bursting activity in other biological preparations besides *Aplysia*.

Acknowledgements. We thank Mrs. Del Fabbro for her help with the illustrations. This work was supported by the Medical Research Council of Canada.

References

Adelman, W.J., Dyro, F.M., Senft, J.: Long duration responses obtained from internally perfused axons. J. Gen. Physiol. **48**, 1—9 (1965)

Alving, B.O.: Spontaneous activity in isolated somata of *Aplysia* pacemaker neurons. J. Gen. Physiol. **51**, 29—45 (1968)

Alving, B.O.: Differences between pacemaker and nonpacemaker neurons of *Aplysia* on voltage clamping. J. Gen. Physiol. **54**, 512—531 (1969)

Armstrong, C.M., Binstock, L.: Anomalous rectification in the squid giant axon injected with tetraethylammonium chloride. J. Gen. Physiol. **48**, 859—872 (1965)

Both, R., Finger, W., Chaplain, R.A.: Model predictions of the ionic mechanisms underlying the beating and bursting pacemaker characteristics of molluscan neurons. Biol. Cybernetics **23**, 1—11 (1976)

Carnevale, N.T.: Voltage clamp analysis of the slow oscillations in bursting neurons reveals two underlying current components. Ph.D. Thesis, Department of Physiology, Duke University, 1974

Carpenter, D.O.: Membrane potential produced directly by the Na^+ pump in *Aplysia* neurons. Comp. Biochem. Physiol. **35**, 371—385 (1970)

Cole, K.S.: Membranes, ions and impulses. Berkeley: University of California Press 1968

Eaton, D.C.: Potassium ion accumulation near a pacemaking cell of *Aplysia*. J. Physiol. **224**, 421—440 (1972)

Frazier, W.T., Kandel, E.R., Kupfermann, I., Waziri, R., Coggeshall, R.E.: Morphological and functional properties of identified neurons in the abdominal ganglion of *Aplysia californica*. J. Neurophysiol. **30**, 1288–1351 (1967)

Geduldig, D., Gruener, R.: Voltage clamp of the *Aplysia* giant neurone: early sodium and calcium currents. J. Physiol. **211**, 217—244 (1970)

Glaser, G.H.: Experimental derangements of extracellular ionic environment. In: Experimental models of epilepsy. Purpura, D.O., et al. (Eds.) pp. 317—345. New York: Raven Press 1972

Gola, M.: Neurones à ondes-salves des mollusques: variations cycliques lentes des conductances ioniques. Pflügers Arch. ges. Physiol. **352**, 17—36 (1964)

Gorman, A.L.F., Mirolli, M.: The passive electrical properties of the membrane of a molluscan neurone. J. Physiol. **227**, 35—49 (1972)

Gulrajani, R.M., Roberge, F.A.: The modelling of the Hodgkin-Huxley membrane with field-effect transistors. Med. Biol. Eng. **14**, 31—41 (1976)

Hille, B.: The selective inhibition of delayed potassium currents in nerve by tetraethylammonium ion. J. Gen. Physiol. **50**, 1287—1302 (1967)

Hodgkin, A.L., Huxley, A.F.: Currents carried by sodium and potassium ions through the membrane of the giant axon of *Loligo*. J. Physiol. **116**, 449—472 (1952a)

Hodgkin, A.L., Huxley, A.F.: The components of membrane conductance in the giant axon of *Loligo*. J. Physiol. **116**, 473—496 (1952b)

Hodgkin, A.L., Huxley, A.F.: The dual effect of membrane potential on sodium conductance in the giant axon of *Loligo*. J. Physiol. **116**, 497—506 (1952c)

Hodgkin, A.L., Huxley, A.F.: A quantitative description of membrane current and its application to conduction and excitation in nerve. J. Physiol. **117**, 500—544 (1952d)

Jack, J.J.B., Noble, D., Tsien, R.W.: Electric current flow in excitable cells. Oxford: Clarendon Press 1975

Junge, D., Stephens, C.L.: Cyclic variation of potassium conductance in a burst-generating neurone in *Aplysia*. J. Physiol. **235**, 155—181 (1973)

Kunze, D.L., Brown, H.M.: Internal potassium and chloride activities and the effects of ACh on identifiable *Aplysia* neurones. Nature New Biol. **229**, 229—231 (1971)

Mathieu, P.A.: Etude d'un rythme neuronal chez l'Aplysie et analogies avec les oscillateurs non-linéaires. Ph.D. Thesis, Universite de Montreal, 1972

Mathieu, P.A., Roberge, F.A.: Characteristics of pacemaker oscillations in *Aplysia* neurons. Canad. J. Physiol. Pharmacol. **49**, 787—795 (1971)

Matsumoto, H., Ayala, G.F., Gumnit, R.J.: Neuronal behavior and triggering mechanism in cortical epileptic focus. J. Neurophysiol. **32**, 688—703 (1969)

Meves, M.: The ionic requirements for the production of action potentials in *Helix pomatia* neurones. Pflügers Arch. ges. Physiol. **304**, 215—241 (1968)

Moore, J.W., Narahashi, T.: Tetrodotoxin's highly selective blockage of an ionic channel. Fed. Proc. **26**, 1655—1663 (1967)

Palti, Y., Adelman, W.J., Jr., Senft, J.P.: Modification of membrane currents and potentials by dynamic alterations of ionic concentration in periaxonal space. In: Actualités neurophysiologiques, 10^{e} série, pp. 210—235. Paris: Masson 1974

Russell, J.M., Brown, A.M.: Sodium and potassium activities inside an identifiable molluscan neuron. Fed. Proc. **31**, 298 (1972)

Smith, T.G., Barker, J.L., Gainer, H.: Requirements for bursting pacemaker potential activity in molluscan neurones. Nature **253**, 450—453 (1975)

Stinnakre, J., Tauc, L.: Calcium influx in active *Aplysia* neurones detected by injected aequorin. Nature New Biol. **242**, 113—115 (1973)

Strumwasser, F.: Membrane and intracellular mechanism governing endogenous activity in neurons. In: Physiological and biochemical aspects of nervous integration. pp. 329—341. Carlson, F.D. (Ed.). New Jersey: Prentice-Hall 1968

Ulbricht, W.: Some effects of calcium ions on the action potential of single nodes of Ranvier. J. Gen. Physiol. **48**, 113—127 (1964)

Watanabe, A., Obara, S., Akiyama, T.: Pacemaker potentials for the periodic burst discharge in the heart ganglion of a stomatopod, *Squilla oratoria*. J. Gen. Physiol. **50**, 839—862 (1967)

Received: October 4, 1976

Prof. F. A. Roberge
Biomed. Eng. Program
Dept. de physiologie/Fac. de Méd.
Case Postale 6208, Succursale A
Montreal, Que. H3C 3T8, Canada

Verantwortlich für den Textteil: Prof. Dr. W. Reichardt, Max-Planck-Institut für biologische Kybernetik, Spemannstr. 38, D-7400 Tübingen. Verantwortlich für den Anzeigenteil: L. Siegel, G. Sternberg, Springer-Verlag, Kurfürstendamm 237, D-1000 Berlin 15, Fernsprecher: (030)8821031, Telex: 01-85411. Springer-Verlag, Berlin · Heidelberg · New York
Druck der Brühlschen Universitätsdruckerei, Gießen. Printed in Germany

Bio-mathematics

Managing Editors: K. Krickeberg, S. Levin

The analytical treatment of biological problems is an area of growing complexity and interest. The series Biomathematics provides a meeting ground for mathematics, biology, and medicine in which crossfertilization of ideas and methodologies may be enhanced. The series includes conventional mathematics and statistics, but places special importance upon innovative mathematical approaches and profound involvement with biological questions.

Volume 1:

Mathematical Topics in Population Genetics

Edited by K. Kojima
55 figures. IX, 400 pages. 1970
Cloth DM 78,—; US $34.40
ISBN 3-540-05054-X

This book is unique in bringing together in one volume many, if not most, of the mathematical theories of population genetics presented in the past which are still valid. The book is written from the geneticist's rather than the mathematician's point of view; and each chapter deals in depht with a single subject, thus introducing all the controversial themes of present-day research. The material is presented and discussed in a way which assumes a certain degree of familiarity with the problems involved.

Volume 2: E. BATSCHELET

Introduction to Mathematics for Life Scientists

2nd edition
227 figures. XV, 643 pages. 1975
Cloth DM 64,—; US $28.20
ISBN 3-540-07293-4

This second edition includes more problems and solutions as well as worked examples. It has been amended throughout along the lines of suggestions from leading biomathematicians. In particular, Chapter 9, "Differential and Integral Calculus" and Chapter 14 "Matrices and Vectors", have been considerably expanded.

Volume 3*/Volume 4*:
M. IOSIFESCU, P. TĂUTU

Stochastic Processes and Applictions in Biology and Medicine

This two-volume treatise is intended as an introduction for mathematicians and biologists with a mathematical background to the study of stochastic processes and their applications in medicine and biology. It is both a textbook and a survey of the most recent developments in this field.
*Distribution rights for the Socialist Countries: Centrala Cartii, Bucharest

Part 1: **Theory**
331 pages. 1973
Cloth DM 58,—; US $25.60
ISBN 3-540-06270-X

Part 2: **Models**
337 pages. 1973
Cloth DM 58,—; US $25.60
ISBN 3-540-06271-8

Volume 5: A. JACQUARD

The Genetic Structure of Populations

Translated by D. Charlesworth, B. Charlesworth
92 figures. XVIII, 569 pages. 1974
Cloth DM 96,—; US $42.30
ISBN 3-540-06329-3

Populations genetics involves the application of genetic information to the problems of evolution. Since genetics models based on probability theory are not too remote from reality, the results of such modeling are relatively reliable and can make important contributions to research. This textbook was first published in French; the English edition has been revised with respect to its scientific content and instructional method.

Volume 6:

Mathematical Demography

Selected Papers
Editors: D. P. Smith, N. Keyfitz
Approx. 350 pages. 1976
In preparation
ISBN 3-540-07899-1

Prices are subject to change without notice

Springer-Verlag
Berlin
Heidelberg
New York

5009/4/1

The Study of Time II

Proceedings of the Second Conference of the International Society for the Study of Time, Lake Yamanaka, Japan

Edited by J. T. Fraser,
International Society for the Study of Time, Westport, Connecticut
and N. Lawrence, Williams College, Massachusetts

80 figures. 4 tables. VII, 486 pages
1975. Cloth DM 57,—; US $25.10
ISBN 3-540-07321-3

Springer-Verlag
Berlin
Heidelberg
New York

This volume contains the proceedings of the Second World Conference on the Study of Time, which took place in the summer of 1973. The range of the topics covered is very wide, extending from biological and physical questions, to philosophical topics, political philosophy and sociological questions. Contributions of a special session, Timekeepers and Time, conclude the volume; the articles in this section are devoted to historical topics, and include many attractive illustrations of old or unusual clocks.

CONTENTS

Previously published

The Study of Time

Proceedings of the First Conference of the International Society for the Study of Time, Oberwolfach (Black Forest), West Germany

Edited by J. T. Fraser, F. C. Haber, and G. H. Müller

65 figures. VIII, 550 pages. 1972
Cloth DM 77,—; US $31.60
ISBN 3-540-05824-9

5045/4/1